THE CHARACTERISATION OF IN(GA)AS QUANTUM DOT LASERS

Ian C Sandall, MPhys (Cardiff)

2006

A thesis submitted to Cardiff University in fulfilment of the requirements of the PhD degree.

ProQuest LLC
789 East Eisenhower Parkway
P.O. Box 1346
Ann Arbor, MI 48106-1346

Abstract

Self-assembled InAs quantum dot lasers have been characterised by measuring the modal absorption and gain along with radiative and non-radiative current densities as well as determining threshold current densities as a function of length. The number of dot layers stacked and the GaAs spacer layers used are both shown to influence the dot density and distribution. The peak ground state gain is found to saturate at around a third of the available absorption in intrinsic quantum dot samples (reaching a value of 1.2±0.2 cm^{-1} per layer). The average spontaneous lifetime of a single dot is determined from measurements of the optical cross section (yielding a value of 2.0±0.5 ns).

From the lifetime measurements, the number of dots occupied at a given injection has been determined; this has shown that gain saturation in quantum dot lasers is due to the incomplete filling of states. The occupancy is shown to increase with the inclusion of p-type modulation doping (from 31% for an intrinsic structure to 43 % and 51 % for doping levels of 15 and 50-p dopants per dot respectively), hence increasing the available ground state gain to 2.2 cm^{-1} per layer for 50 dopants per dot. In some of the samples studied the use of modulation doping has been shown to lead to an increase in the non-radiative current density. The temperature dependence of the threshold current density in InAs quantum dot lasers is also investigated. It is found that in the p-doped structures the threshold current shows an initial decrease in the threshold current, before increasing at higher temperatures (for example a decrease of 100Acm^{-2} occurs between 180 and 290 K for a 2 mm long cavity with 15-p dopants per dot), this is shown to originate from the temperature dependence of the modal gain in these structures.

Acknowledgements

I would firstly like to thank my supervisors Doctor Peter Smowton and Professor Peter Blood for their guidance and support throughout this work. I would also like to thank everyone in the Optoelectronics group that helped contribute to such a good working environment. Thanks also to all the technical staff for the support and advice which I have received along the way.

I would also like to thank all my family and friends for their support and their belief in me. I would especially like to thank Beth for giving me the motivation and belief in myself to complete this work.

1. Thesis Rationale and Background

1.1 Introduction

The work presented in this thesis has been conducted with the intention of characterising and optimising the performance of InAs quantum dot structures for use in semiconductor laser diodes. In particular the modal absorption, gain and un amplified spontaneous emission are studied using the segmented contact technique [1].

The idea of using quantum dots as the active gain medium in semiconductor lasers was first proposed in 1982 by Arakawa [2]. Quantum dot systems have since attracted a great deal of interest due to the promise of low threshold currents, good temperature stability and broad gain spectra [3,4]. An additional interest for InAs quantum dot lasers is the prospect of achieving lasing on GaAs substrates over the technologically important wavelength range 1.3 – 1.6 μm. This is an important wavelength range as at 1.3 and 1.55 μm there are minima in the loss and dispersion in optical fibres and hence are the optimum wavelengths to operate laser diodes for optical communications. Current laser diodes operating at these wavelengths are based on InP quantum well lasers. The relatively shallow potential wells in these materials lead to poor temperature sensitivity, while the Bragg mirror stacks, required for VCSEL operation are difficult and expensive to engineer. The ability to grow semiconductor lasers in GaAs substrates would remove these problems as deeper potentials are formed in InAs quantum dots and Bragg reflectors are common and inexpensive on GaAs.

To allow these structures to be fully optimised the modal gain and recombination paths have to be analysed. Knowledge of the modal gain spectra allows for accurate design of VCSEL cavities for surface emission, while knowledge of the

radiative and non-radiative currents allows the efficiency of the structures to be determined and optimised.

1.1.2 Thesis Structure:

The remainder of this chapter describes some basic semiconductor physics and laser concepts that will be required to understand the work and the results in the following chapters. The chapter will conclude with a summary of the development of InAs quantum dot lasers up to the beginning of this work.

Chapter two outlines the experimental techniques used in this work; this includes a description of the theoretical ideas around the experiment as well as details of how the work was carried out.

Chapter three looks at how the growth conditions of GaAs spacer layers can greatly enhance the performance of multilayer quantum dot structures. The chapter will go on to show that even in low threshold devices a large fraction of this current is still due to on-radiative contributions. The origin of this non-radiative current will also be investigated.

Chapter four shows the effects of increasing the number of quantum dot layers in the samples. The data from this will be used to further investigate possible sources of non-radiative recombination in InAs quantum dot samples.

Chapter five analyses the use of modulation doping to increase the modal gain and hence decrease the threshold current in quantum dot lasers. This work is carried out by analysing how both the modal gain and the recombination currents are modified in doped structures.

Chapter six investigates further the effects of p-type modulation doping by investigating the temperature performance of the threshold current in doped structures.

This is done by investigating how the temperature performance of both the modal gain and the non-radiative currents are influenced by doping.

Chapter seven uses absorption measurements to determine the average radiative lifetime of a single quantum dot. The lifetime is calculated for each of the structures investigated in the previous chapters to see how it is influenced by the various factors studied. The lifetime is used to calculate the number of carriers in each dot at a given injection level and is used to try and further understand the non-radiative processes in InAs quantum dot samples.

Finally chapter eight gives a summary of the main points encountered from this work and suggest some possible future investigations originating from this study.

1.2 Semiconductor Physics

1.2.1 Bandstructure

The electrical properties of semiconductors are described in detail in many textbooks on solid state physics [5,6]; here a brief account of the main points is given. Semiconductor crystals are formed via covalent bonds between atoms which result in the formation of a lattice structure. The periodicity of this lattice affects the electrical and optical properties of the semiconductor. The interaction of consecutive atoms causes a splitting of the energy levels due to a difference in symmetric and anti-symmetric bonding. This behaviour occurs over the complete lattice, resulting in the formation of bands of closely spaced energy levels. The two most important bands when considering a semiconductor laser are the adjacent conduction and valence bands. At absolute zero all the valence band states are occupied with electrons, while all the conduction band states are empty. As the temperature is then increased electrons can be

thermally excited from valence band to the conduction band. Unoccupied states in the valence band can be described as being occupied by 'holes' which behave as positively charged electrons.

The conduction and valence bands are described by the E-k relationships. In a simplified picture these can be approximated by parabolas,

$$E(k) = \frac{\hbar^2 k^2}{2m^*} \qquad \textbf{Equation 1.1}$$

where m^* is the effective mass of the electrons (or holes) in the conduction (or valence) band and k is the wavevector which is related to the electron momentum by,

$$p = \hbar k \qquad \textbf{Equation 1.2}$$

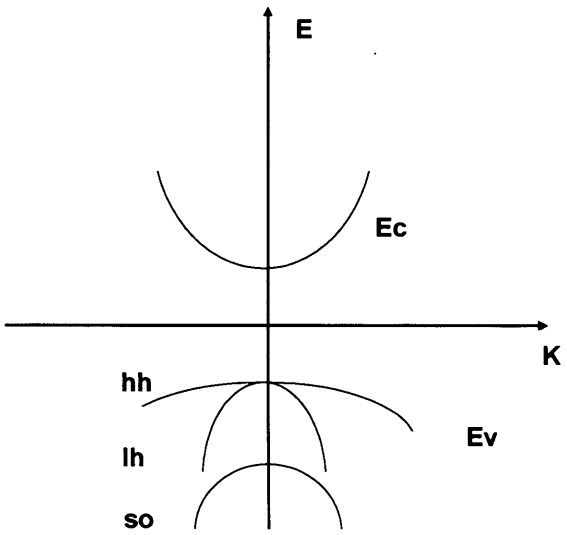

Figure 1.1: - E-k Band Diagram

Under the influence of strain in the material the valence band splits into the heavy-hole (hh), light-hole (lh) and split off (so) bands due to spin-orbit coupling as shown. The minimum energy difference between the two bands (occurring at k = 0 in the diagram) gives the band gap of the material. When the minima occur at the same k-

value it is known as a direct band gap material, while if the minima occur at different k-values it is known as indirect bandgap. Any transition between the conduction and valence bands must conserve both energy and momentum so the emitted photon energy must be equal to the difference in the electron and hole energies.

$$h\nu = E_g + \frac{\hbar^2 k^2}{2m_c^*} + \frac{\hbar^2 k^2}{2m_v^*} \qquad \textbf{Equation 1.3}$$

Given that photons have a negligible momentum, the electrons and holes must also have the same k-value.

1.2.2 Fermi-Functions:

The probability of an energy state being occupied by an electron is described by the Fermi-Dirac distribution, giving occupation probabilities for the conduction and valence band as,

$$f_c = \frac{1}{e^{(E-E_{Fc})/kT} + 1} \qquad \textbf{Equation 1.4}$$

and

$$f_v = \frac{1}{e^{-(E-E_{Fv})/kT} + 1} \qquad \textbf{Equation 1.5}$$

where k is the Boltzmann constant, T is the temperature and E_{Fc} and E_{Fv} are the quasi-Fermi levels for electrons in the conduction and valence band respectively.

1.2.3 Quantum Confinement:

If one or more dimensions of a semiconductor are reduced quantum confinement effects can alter the electronic states within the semiconductor. To investigate the behaviour of electrons and holes in quantum confined structures the time independent Schrödinger equation has to be solved,

$$\frac{\partial^2\varphi(r)}{\partial r^2}+\frac{2m^*}{\hbar^2}(E-U(r))\varphi(r)=0 \qquad \textbf{Equation 1.6}$$

where U(r) is the background potential to the crystal lattice. The wavefunctions for the electrons (and holes) can be described using Bloch's theorem. This states that the wavefunction can be written as two parts, an envelope function and a periodic function. So for the electrons the wavefunction is given by,

$$\varphi_c(r)=F(r)u_c(r) \qquad \textbf{Equation 1.7}$$

where F(r) is the normalised envelope function and $u_c(r)$ is the Bloch function for the conduction band which has the periodicity of the lattice. A similar expression can be obtained for the hole wavefunction. Applying this to a three dimensionally confined system (a quantum dot), with infinite barriers, the following energy levels are obtained,

$$E_{nx,ny,nz}=\frac{\hbar^2\pi^2}{2m^*}\left(\frac{n_x^2}{L_x^2}+\frac{n_y^2}{L_y^2}+\frac{n_z^2}{L_z^2}\right) \qquad \textbf{Equation 1.8}$$

where L_x, L_y and L_z give the dimensions of the dot in the x, y and z directions.

1.3 Laser Diodes

A laser produces coherent light by allowing stimulated emission to dominate over absorption and spontaneous emission (these processes will be discussed in more detail in section 1.4). A laser diode is formed by placing an 'active region' in a resonant cavity, with partially reflecting mirrors. Electrons in the active layer can be excited

(either electrically or optically) into non-equilibrium higher energy states. The electrons can then relax back into an equilibrium state releasing a photon in the process (known as spontaneous emission). This creates a photon density which can be amplified by the non-equilibrium electron distribution through the process of stimulated emission leading to laser action.

1.3.1 Threshold Gain:

In a semiconductor laser diode a non-equilibrium electron distribution is achieved via electrical pumping by injecting the carriers through a p-n junction. The growth of the photon density due to stimulated emission can be characterised by the modal gain of the cavity.

As the photon density travels along the cavity it grows in intensity due to stimulated emission events. The ends of the cavity consist of partially reflecting mirrors (typically formed by the air / semiconductor interface of the diode) as such some of the light is transmitted from the device and some is reflected back across the cavity (providing optical feedback). For sustained lasing to occur the growth of the photon density (the gain) must be equal to the losses in the cavity, as such it can be shown that the threshold condition for the modal gain is,

$$G = \frac{1}{L_C} \ln\left(\frac{1}{R}\right) + \alpha_i \qquad \textbf{Equation 1.9}$$

where L_c is the length of the cavity, R is the reflectivity of the mirrors (typically ~ 0.3 for an air / semiconductor interface and α_i is the intrinsic scattering loss caused by the scattering of photons within the cavity. Therefore coherent light is produced and hence lasing is achieved through the oscillation of stimulated emission in the cavity.

1.3.2 History of the diode laser:

The first semiconductor laser diodes were developed in 1962 and based on GaAs homojunctions, where the mirrors were formed by polishing of the crystal in the plane perpendicular to the junction [7-10]. Schematic diagrams are shown in Figure 1.2 for a homojunction under (a) equilibrium conditions and (b) when a forward bias is applied.

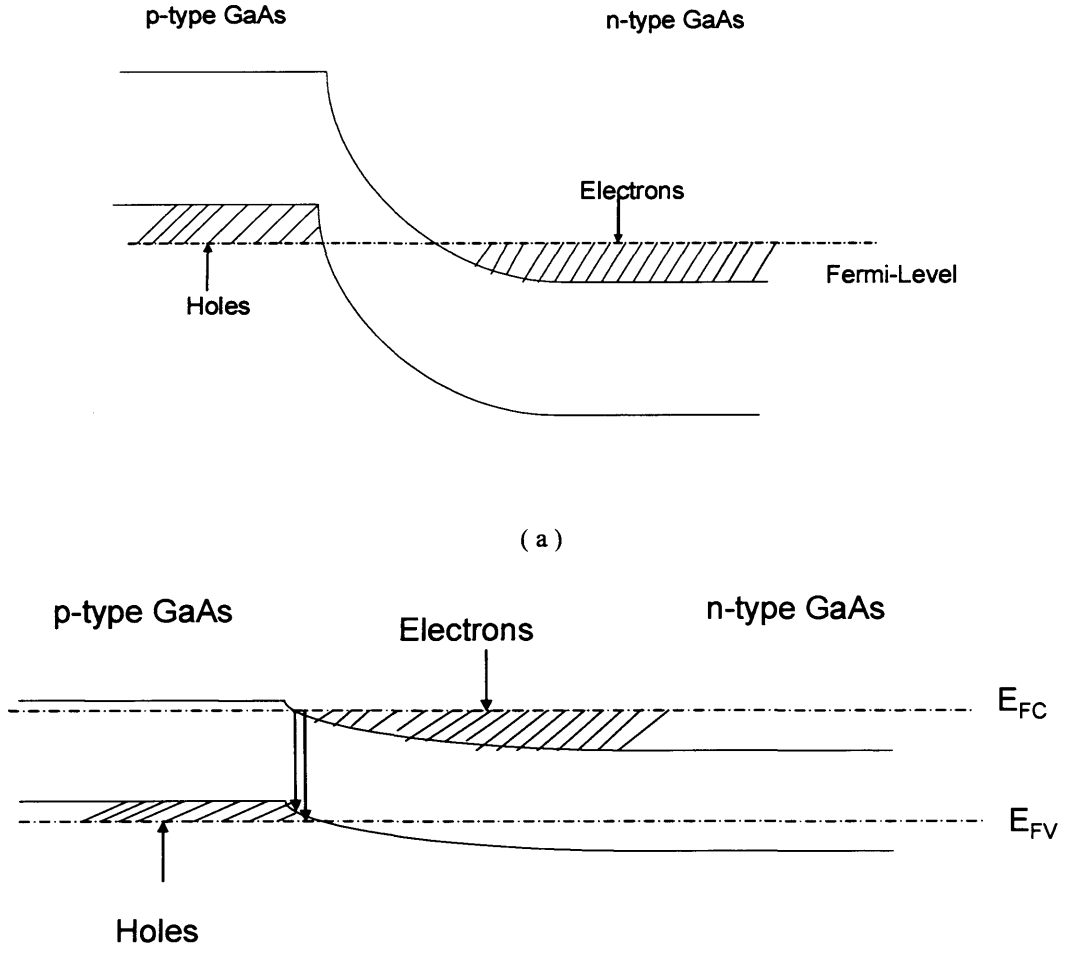

Figure 1.2: - Schematic diagram of a homojunction in equilibrium (a) and under a forward bias (b).

In equilibrium the Fermi level lies within conduction band for the n-type GaAs and within the valence band for the p-type material. When a forward bias is applied the

bands begin to bend and the Fermi level splits into two quasi-Fermi levels for the conduction and valence band. The situation shown in figure 1.2b is for when the applied voltage is approximately the same as the bandgap of the junction. An active region is formed in the junction where the electrons and holes overlap leading to radiative recombination and the ability for stimulated emission to take place.

These early laser diodes had high threshold current densities (~10 $kAcm^{-2}$) with lasing only possible at liquid nitrogen temperatures [7-10]. These high operating currents were partially due to poor carrier confinement and overlap (as shown in figure 2b) and also due to a poor optical confinement of the produced light. The light is poorly confined in such structures due to very little variation in the refractive index across the junction and the poor confinement reduces the probability of stimulated emission.

Reduced threshold currents and room temperature lasing were achieved through, the development of the double heterostructure [11-13]. In such a structure the active region is sandwiched between n- and p-type doped layers that have larger band gaps (forming a p-i-n junction). As well as increasing the carrier confinement by reducing diffusion away from the junction, the change in bandgap also creates a step in the refractive index profile, leading to optical confinement. Such a structure lead to the first report of continuous operation at room temperature[14].

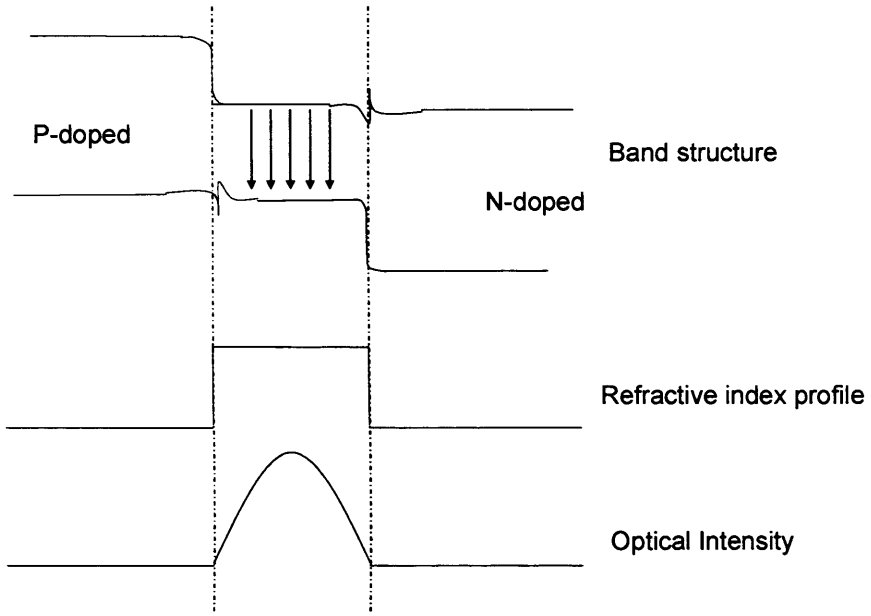

Figure 1.3: - Band diagram, refractive index profile and the optical intensity in a double heterostructure.

Further improvements in threshold current and device performance were obtained by the development of the separate confinement heterostructure [15-17]. This involved the placing of a lower bandgap material at the centre of the structure (for example GaAs in AlGaAs).

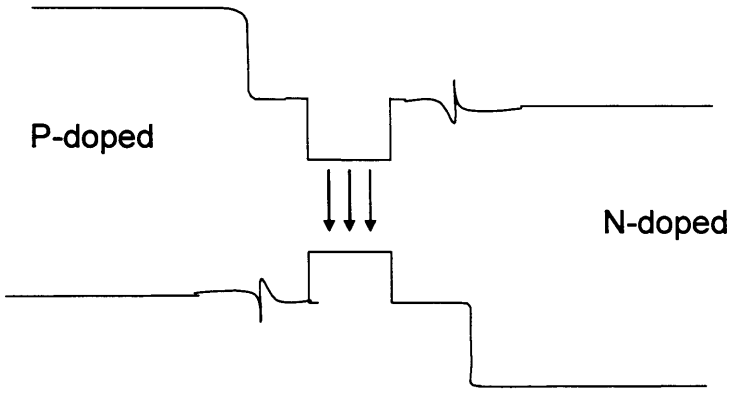

Figure 1.4: - Band diagram for a separate confinement heterostructure.

If the thickness of the separate confinement layer becomes sufficiently thin (approximately of the order of the de Broglie wavelength, <10nm) the carriers become

localised in this region and a quantum well system is formed [18,19], where the depth of the well is determined by the offset of the conduction and valence bands. More recently quantum dot separate confinement heterostructures have been developed as the active region in laser diodes [20-22].

1.4 Optical transitions:

There are three possible optical transitions that can occur between two energy levels (i.e. in a semiconductor). These are absorption, spontaneous emission and stimulated emission.

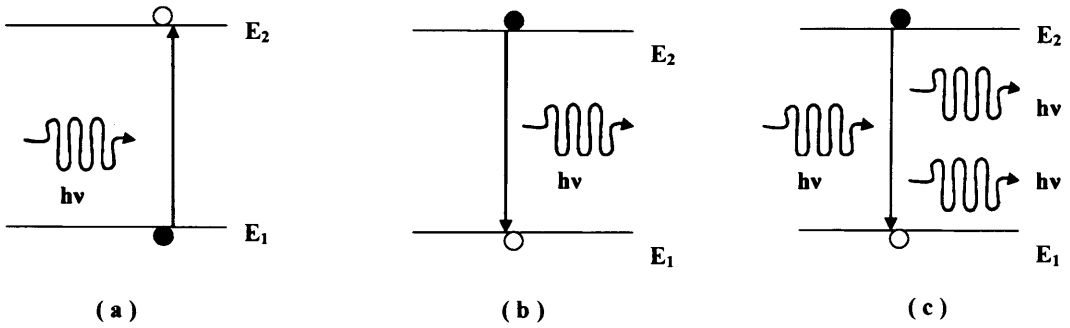

Figure 1.5: - Diagrams illustrating (a) absorption, (b) spontaneous emission and (c) stimulated emission.

1.4.1 Absorption:

In an absorption event an electron is initially in the lower energy level (the valence band) and an incoming photon with an energy equal to the band gap is 'absorbed' by the electron, causing the electron to travel to an empty state in the higher energy level (the conduction band). The absorption rate is therefore controlled by the number of photons with the appropriate energy, the number of electrons in the valence

band and the number of empty states in the conduction band. The total rate is therefore given by

$$r_{abs} = B_{1,2}(1-f_2)f_1\rho(h\nu) \qquad \textbf{Equation 1.10}$$

where f_1 and f_2 are the occupation probabilities for electrons in the lower and upper states respectively, ρ is the photon density and $B_{1,2}$ is a probability coefficient.

1.4.2 Spontaneous Emission:

A spontaneous emission event occurs when an electron spontaneously "falls" from the higher to the lower energy level releasing a photon in the process. The energy of this photon is again equal to energy difference between the two states. This process is governed by so called 'virtual' photons generated by zero-point fluctuations in the electromagnetic field. As such this process is independent of any photon density and is controlled only by the relative occupation of the two states,

$$r_{Spon} = A_{2,1}f_2(1-f_1) \qquad \textbf{Equation 1.11}$$

where $A_{2,1}$ is again a probability coefficient. The direction and phase of the electrons that are emitted due to this process are random.

1.4.3 Stimulated Emission:

A stimulated emission event occurs when an incoming photon (with an energy equal to the difference between the two states) perturbs an electron in the upper state (conduction band). This results in the electron falling down to the lower state (valence

band) releasing another photon in the process. As well as having the same energy as the first photon the second photon is coherent with the first (has the same phase and direction). This rate is therefore controlled by the photon density and the relative occupation probabilities,

$$r_{stim} = B_{2,1}(1-f_1)f_2\rho(h\nu) \qquad \textbf{Equation 1.12}$$

where $B_{2,1}$ is another probability coefficient.

Under equilibrium conditions the upward and downwards transition rates must balance so,

$$r_{abs} = r_{spon} + r_{stim} \qquad \textbf{Equation 1.13}$$

This expression was first solved by Einstein in 1917 [23,24] where under the conditions,

$$B_{1,2} = B_{2,1} \qquad \textbf{Equation 1.14}$$

and

$$A_{2,1} = \frac{8\pi n^3}{h^3 c^3}(h\nu)^2 B_{2,1} \qquad \textbf{Equation 1.15}$$

he derived Planck's law of blackbody radiation. As such the probability coefficients $A_{2,1}$, $B_{2,1}$ and $B_{1,2}$ are known as the Einstein coefficients. This relates the coefficients for spontaneous and stimulated emission. The units of $A_{2,1}$ are inverse time and as such it is related to the spontaneous lifetime of the transition by,

$$A_{2,1} = \frac{1}{\tau_s} \qquad \textbf{Equation 1.16}$$

1.5 Population Inversion

As was shown in the previous section in thermal equilibrium the rate of downward transitions is equal to the rate of upward transitions. For lasing action to

occur, stimulated emission must dominate in the cavity, and hence there must be more carriers in the upper state than the lower. However this cannot be achieved under thermal equilibrium in a two level system. Therefore to obtain population inversion and hence allow stimulated emission to become the dominant process, a non-equilibrium state of the system has to be achieved.

1.5.1 Three Level Systems:

A schematic overview of a three level system is shown in Figure 1.6. In such a system electrons are initially pumped (either electrically or optically) from the ground state, E_0 to a higher energy state (labelled E_2). The electrons can then relax to the intermediate energy level, E_1. Provided the relaxation time between E_2 and E_1 is quicker than the recombination time between E_1 and the ground state then the electron population can build up in the higher state and lasing can occur between E_1 and the ground state.

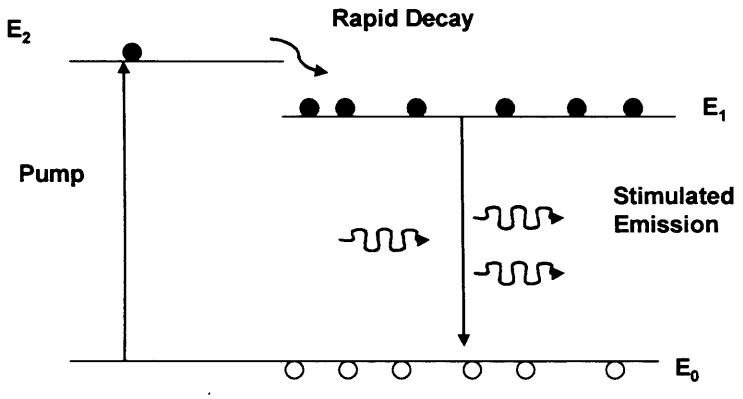

Figure 1.6: - Schematic diagram of a three level laser system

Although lasing can occur in three level systems, the process is very inefficient, as to achieve population inversion over half the electrons need to be excited out of the

ground state, as such large pump powers are required. Population inversion can be achieved more easily by using a four level system.

1.5.2 Four Level Systems:

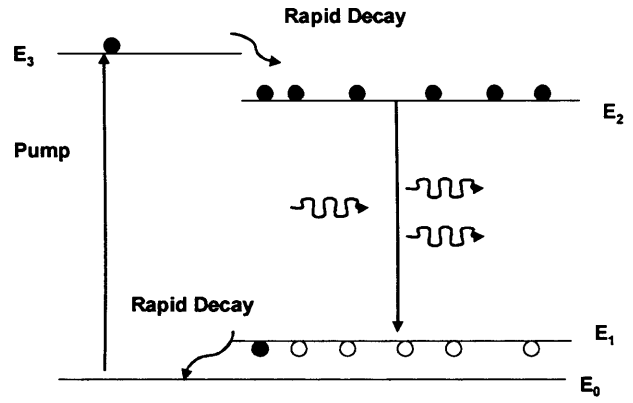

Figure 1.7: - Schematic diagram of a four level laser system.

In a four level system, electrons are pumped out of the ground state to a higher energy state (E_3), where they rapidly decay to the state E_2. Lasing then occurs between the levels E_2 and E_1. The electrons then decay back to the ground state. As the lasing transition in this system does not involve the ground state, population inversion can be achieved with much lower pump powers. Semiconductor lasers form a four level system where a continuum of states forms the lowest and uppermost energy levels and lasing occurs between two discrete levels.

1.6 Non-Radiative Recombination Processes

It is possible for electrons in the conduction band and holes in the valence band to recombine non-radiatively (i.e. recombination without the emission of a photon). Such events raise the current required to achieve threshold in a laser and ideally need to be identified and minimised. Due to the absence of light in these processes, they can only be detected indirectly and (as such) determining the non-radiative process is

difficult. To identify the process the temperature dependence of various quantities (i.e. threshold current, radiative current, efficiency) need to be measured. There are two main sources of non-radiative recombination in semiconductor lasers that will now be discussed.

1.6.1 Recombination via Defects:

In an ideal semiconductor there are no defects or impurities in the crystal lattice. However in a real semiconductor structure impurities or defects can form (i.e. due to a vacant lattice site), and such defects result in a localised state in the crystal. If a defect state forms on or in the conduction or valence band, the effects are negligible. However as the defect is localised spatially it is able to form in the 'forbidden' energy gap, where it can have a significant impact on the recombination in the structure. This type of recombination was first described in 1952 by Hall [25] and in a separate publication by Shockley and Read [26] and (as such) is commonly known as Shockley-Read-Hall recombination. A recombination event is shown schematically in Figure 1.8.

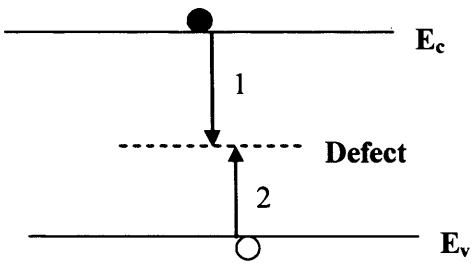

Figure 1.8: - Schematic diagram of recombination via a defect state.

In such a recombination event a carrier is captured by the defect (in the example shown an electron is captured). This then charges the defect state and results in the capture and subsequent recombination (resulting in the emission of a phonon) of a

carrier of opposite charge (a hole in the example). The recombination rate of this type of process is determined by the carrier with the slowest capture rate.

1.6.2 Auger Recombination:

Auger recombination occurs due to a hole and electron recombining indirectly. Momentum and energy are conserved in this process by the emission of a second electron (or hole) high into the conduction (or valence band), where it then relaxes via multi phonon emission. Due to energy and momentum having to be conserved Auger recombination is generally negligible in wide band gap materials, but becomes increasingly important as the band gap is narrowed. Auger recombination has been predicted to contribute a high proportion of the current in InAs quantum dot lasers [27]. There are several different Auger process that can occur [24]. For simplicity one such process is illustrated in Figure 9.

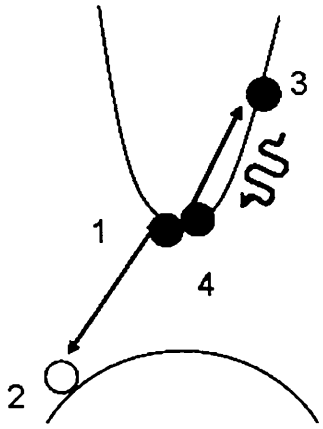

Figure 1.9: - Schematic diagram of an Auger recombination process

In the process illustrated an electron (1) recombines with a hole (2), and this causes a second electron to travel high into the conduction band (3) where it then relaxes back to its initial position via multiple phonon emission (4).

1.7 Quantum Dot Systems

As previously mentioned the development of quantum well lasers has led to low threshold devices. However these remain sensitive to temperature. The natural progression from such a two dimensional system is to a one dimensional quantum wire (where the carriers are confined in two dimensions) and further on to a zero dimensional quantum dot (where the carriers are confined in all three directions). The work in this thesis is concerned with characterising quantum dot systems; therefore this following section will describe some of the key factors affecting quantum dot performance.

Many of the predicted improvements in performance in quantum dot systems originate from the three dimensional confinement of carriers. To confine the carriers the dimensions of the dot have to be of the order of the de Broglie wavelength (~10nm). When Schrödinger's equation is solved for such a system a series of widely spaced discrete energy levels is obtained (equation 1.8). These discrete energy levels are similar to the energy levels within an atom and as such an ensemble of quantum dots behaves in a similar to a solid state laser.

N.B: Although a quantum dot has a similar energy structure as an atom, a single dot can comprise more than ten thousand atoms.

Quantum dot systems were predicted to have several key advantages over quantum well lasers. These were: a reduced threshold current, a narrow spectral line and reduced temperature sensitivity. The reduced threshold comes from having many dots at the same energy resulting in fewer carriers being required to achieve population inversion. A narrow spectral emission line was predicted due to the dots having the same energy states. A reduced temperature sensitivity, was predicted due to the expected delta like density of states.

1.7.1 Quantum Dot Growth:

The most common way of growing quantum dot systems is through the self-assembly Stranski-Krastanow growth mode. The self-organised mechanism exploits the high lattice mismatch which can occur between semiconductor materials (for example there is a mismatch of approximately 7% between InAs and GaAs). Material of one type is deposited on top of a substrate. Each of these materials has a different surface energy and as increasing layers of material are deposited the strain energy increases, due to the lattice mismatch. The material initially forms a few monolayer thick film, known as the wetting layer. After the strain energy becomes too great to allow the continual stacking of material, then material nucleation begins which leads on to small three-dimensional island formation. The exact nature of the islands formed: size, shape, density, uniformity are all very sensitive to the growth conditions and can lead to difficulty in trying to obtain reproducible structures.

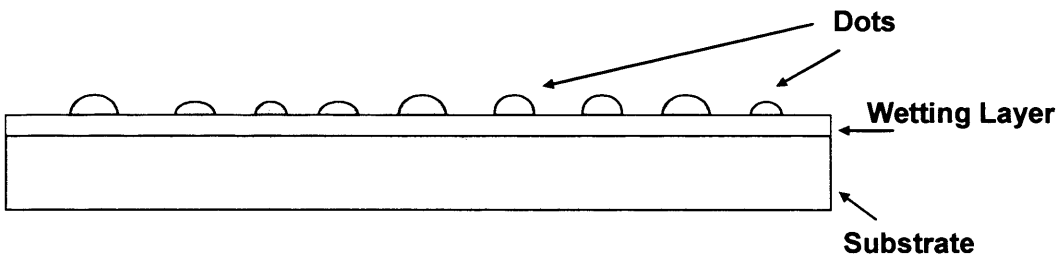

Figure 1.10: S-K growth mode

This method has been used successfully to grow quantum dot structures on many material systems including InAs [21,22], InP [28,29] and GaN [30,31].

Dots grown in this self-formation technique are accompanied by the wetting layer, as described above. This results in a coupled wetting layer quantum dot system, where the wetting layer provides a reservoir of carriers, allowing electrons and holes to

be transported between the dots. This allows quantum dot systems to be highly efficient as it allows electrons and holes to move across the ensemble and recombine. However due to the large number of carriers present in the wetting layer which leads to the incomplete occupation of the quantum dot states, the system is not completely inverted [32]. As such the modal gain achieved is less than that from a fully inverted system.

Practical quantum dot systems are also affected by the presence of excited states. In an ideal dot the energy levels would be widely spaced in energy, limiting any thermal activation of carriers into excited state(s). However in real quantum dot systems the size of the dots leads to the presence of excited state(s) which are comparably spaced with the thermal energy of the carriers. Therefore the effect of these state(s) cannot be ignored when considering real quantum dot systems.

1.7.3 Broadening

The transition from an ideal quantum dot should be a sharp delta function; however the transition is broadened by several factors. There are essentially two types of broadening that the dot will experience. The first of these broadens the transition from a single dot, while the second arises due differences between the dots in an ensemble.

Homogenous Broadening:

Homogenous broadening arises from the uncertainty principle. The energy of an electron (or hole) will only be well defined after a long period of time and therefore there is a probability that the electron energy is not exactly equal to the energy of the state. This can also be described in a wave picture by dephasing events due to collisions. This broadening is normally expressed in terms of a normalised Lorentzian function. In

quantum dot systems the value of the homogeneous broadening is typically in the order of meV [33,34].

Inhomogeneous Broadening:

This form of broadening arises in quantum dot ensembles and is due to differences between the individual dots. Each dot has an energy transition described by a Lorentzian distribution centred at the transition energy, however the dots can have different transition energies due to fluctuations in the size, shape and composition in each dot. These fluctuations are a result of the self-formation process used. The inhomogeneous broadening can be described by a Gaussian function over the ensemble. The inhomogeneous broadening is the dominant broadening mechanism in quantum dot ensembles [33,35].

1.8 Modal Gain

The starting point for the calculation of optical gain in bulk, quantum well and quantum wire systems is Fermi's Golden Rule [24]. This is concerned with transitions from a discrete energy state to a continuum of energy states with an appropriately defined density of states function, which includes k-selection. However such an approach cannot be used for a quantum dot system as the dot contains a series of discrete energy levels and as such does not have a continuum of energy states. Expressions for the modal gain of a quantum dot system have been derived using a modified "density of states" [36-39], which describe many properties of a quantum dot system.

These methods use a joint density of states based on the distribution of the energy levels (arising from the inhomogenously broadened ensemble). This assumes the electrons and holes are free to move around this energy distribution and in essence

allow any electron to recombine with any hole. However the energy states are not extended over the whole ensemble and as such cannot be combined to form a joint density of states. The localisation of carriers in the dots means that an electron can only recombine with a hole if it is in the same dot, leading to an additional spatial selection rule in quantum dot systems.

The approach taken here to determine the modal gain of an ensemble of quantum dots considers optical transitions in a two level system [40]. To begin with a single dot is analysed in the presence of an energy flux, S given by,

$$S = \frac{1}{2} cn\varepsilon_0 \omega^2 A_0^2 \qquad \textbf{Equation 1.17}$$

where A_0 is the vector potential and ω is the frequency of the electromagnetic field. The rate of absorption between the two energy levels in the dot is given by,

$$U = (\hbar\omega)\frac{\pi e^2}{m_0^2 \hbar} A_0{}^2 \gamma M^2 \left\{ \int_{dot} F_2(r)^* F_1(r) d^3 r \right\}^2 L(\hbar\omega) \qquad \textbf{Equation 1.18}$$

where M is the momentum matrix element for the dot, $F_2(r)$ and $F_1(r)$ are envelope functions describing the localisation of the electrons and holes within the dot. The factor γ allows for the relative orientation of the polarisation of the electromagnetic field and the dot. $L(\hbar\omega)$ is the Lorentzian function describing the homogenous broadening of the transition. A factor of 2 has also been included to take account of spin degeneracy.

The optical cross section of a single dot is given by the amount of energy absorbed from the incident flux,

$$\sigma(\hbar\omega, E_i) = \frac{2\pi\hbar}{cn\varepsilon_0(\hbar\omega)} \left(\frac{e}{m_0} \right)^2 \gamma M^2 \left\{ \int_{dot} F_2(r)^* F_1(r) d^3 r \right\}^2 L(\hbar\omega) \qquad \textbf{Equation 1.19}$$

This can be re-written as,

$$\sigma(\hbar\omega, E_i) = \sigma_0(E_i) L(\hbar\omega) \qquad \textbf{Equation 1.20}$$

giving the absorption strength for the transition in terms of a cross sectional area (σ_0) multiplied by an energy. As described in [35] the optical cross section can be determined by integrating the measured modal absorption spectrum, A(hv):

$$\sigma_0 = \frac{w_{\text{mod}}}{N_{Dots}} \int A(hv) d(hv) \qquad \textbf{Equation 1.21}$$

where N_{Dots} is the number of dots per unit area and ω_{mod} is an effective mode width which describes the coupling between the mode and the dot [36],

$$\frac{1}{w_{\text{mod}}} = \frac{A_{dot}^2}{\int A^2(z) dz} \qquad \textbf{Equation 1.22}$$

The optical gain of a cavity is defined as the fractional increase of the total energy in a guided mode per unit distance travelled. The total energy flux in the mode is determined from equation 1.16 as,

$$W_{Tot} = \left\{ \frac{1}{2} cn\varepsilon_0 \omega^2 \int_{dot} A^2(z) dz \right\} w \qquad \textbf{Equation 1.23}$$

where w gives the width of the mode. The increase in the energy in the mode due to a single dot is the same as the rate of absorption (equation 17),

$$U = (\hbar\omega) \frac{\pi e^2}{m_0^2 \hbar} A_{dot}{}^2 \gamma M^2 \left\{ \int_{dot} F_2(r)^* F_1(r) d^3 r \right\}^2 L(\hbar\omega)[f_1 - f_2] \qquad \textbf{Equation 1.24}$$

where A_{dot} is the vector potential of the electromagnetic field at the location of the dot and f_1 and f_2 are probability factors describing the occupation of the upper and lower states.

The modal gain is therefore given by,

$$G = \frac{U}{W_{Tot}.L}$$ **Equation 1.25**

where L is the distance travelled along the cavity therefore,

$$G(\hbar\omega) = \frac{2\pi\hbar}{cn\varepsilon_o(\hbar\omega)}\left(\frac{e}{m_0}\right)^2 \frac{A_{dot}^2}{\int_{dot} A^2(z)dz}\frac{1}{w.L}\gamma M^2\left\{\int_{dot} F_2(r)^* F_1(r)d^3r\right\}^2 L(\hbar\omega)[f_1 - f_2]$$

Equation 1.27

This can be rewritten using equations 1.20 and 1.22 as

$$G(\hbar\omega) = \frac{\sigma_0(E_i)L(E_i,\hbar\omega)}{\omega_{\text{mod}}.w.L}[f_1 - f_2]$$ **Equation 1.28**

This expression therefore gives the modal gain due to a single dot with the electrons localised due to normalised envelope functions. In an ensemble of dots with a density of N_{dots} dots per unit area, the modal gain of the system can be determined by summing the gain contributions from each dot over the length and width of the guide,

$$G_{Total}(\hbar\omega) = N_{dots}wL\sum_i G_i(\hbar\omega)P(E_i)$$ **Equation 1.29**

where $P(E_i)$ is a Gaussian function describing the inhomogeneous broadening of the dots. Therefore the total gain is given by,

$$G(\hbar\omega) = \frac{N}{\omega_{\text{mod}}}\sum_i \sigma_0(E_i)L(E_i,\hbar\omega)P(E_i)[f_1 - f_2]$$ **Equation 1.30**

the probability occupation factors are defined globally for the whole system (so any two dots with the same energy separation will have the same probability of occupation). The approach taken here takes account of the spatial localisation of the carriers, as such the gain scales with the number of dots.

The optical gain of a cavity is defined as the fractional increase in the photon density per unit length as the light propagates along the cavity. For a transition between

a single pair of states (for example a single quantum dot) the number of photons generated at a given photon energy (hv) is given by the difference between the net upward and downward rates (the difference between absorption and emission as given in section 1.4) multiplied by the Lorentzian broadening:

$$r_{net}(hv) = B(E_i)(f_2 - f_1)\rho(hv)L(E_i) \qquad \textbf{Equation 1.31}$$

If the cavity volume is defined as V_{cav} then the ratio of the gain to the total photon density within the cavity will give another expression for the modal gain,

$$G(hv) = \left(\frac{n}{c}\right)\frac{2B(E_i)(f_2 - f_1)\rho(hv)L(E_i)}{\rho(hv)V_{Cav}} \qquad \textbf{Equation 1.32}$$

where the factor of 2 has been included to take account of spin degeneracy. This can be equated with equation 1.26, which gives the gain for a single quantum dot,

$$B = \frac{1}{2}\left(\frac{c}{n}\right)\frac{V}{w_{\mathrm{mod}}wL}\sigma_0 \qquad \textbf{Equation 1.33}$$

and given that the cavity volume is defined such that,

$$V_{Cav} = w_{\mathrm{mod}}wL \qquad \textbf{Equation 1.34}$$

then,

$$B = \frac{1}{2}\left(\frac{c}{n}\right)\sigma_0 \qquad \textbf{Equation 1.35}$$

And by substituting this expression into equation 1.15 the spontaneous emission rate can be related to the optical cross section:

$$A_{2,1} = \frac{1}{2}\frac{8\pi n^2(hv)^2}{h^3c^2}\sigma_0 \qquad \textbf{Equation 1.36}$$

Therefore by determining the optical cross section of a single dot it is possible to calculate the spontaneous lifetime of that dot.

1.9 Spontaneous Emission Rate

Spontaneous emission is the excitation of a carrier from an occupied state to a lower energy unoccupied state via the emission of a single photon into an optical mode [24,36]. The probability of such a transition occurring in a simple two level system (i.e. a single quantum dot is given by),

$$W_{1\to 2}(\hbar\omega) = \frac{4\pi}{\hbar}\left|H'_{1,2}\right|^2 L(E_i,\hbar\omega)[f_1(1-f_2)] \qquad \textbf{Equation 1.37}$$

where f_1 and f_2 give the probability of occupation for the two states, and spin degeneracy has been accounted for, while $H'_{1,2}$ is related to the momentum matrix element by,

$$\left|H'_{1,2}\right|^2 = \left(\frac{e}{2m_0}\right)^2 \gamma A_0^2 M^2 \left\{\int F_1(r)^* F_2(r) d^3r\right\}^2 \qquad \textbf{Equation 1.38}$$

So,

$$W_{1\to 2}(\hbar\omega) = \frac{4\pi}{\hbar}\left(\frac{e}{2m_0}\right)^2 A_0^2 \gamma M^2 \left\{\int F_1(r)^* F_2(r) d^3r\right\}^2 [f_1(1-f_2)]L(E_i,\hbar\omega) \qquad \textbf{Equation 1.39}$$

The spontaneous emission rate is therefore given by the probability of the transition occurring multiplied by the number of optical modes available. The density of optical modes per unit volume in one polarisation is given by,

$$P_{Opt}(\hbar\omega) = \frac{1}{3\pi^2}\frac{n_g n^2}{(\hbar c)^3}(\hbar\omega)^2 \qquad \textbf{Equation 1.40}$$

while the vector potential associated with a single photon of frequency, ω in a unit volume is given by,

$$A_0 = \sqrt{\frac{2\hbar}{nn_g\varepsilon_0\omega}} \qquad \textbf{Equation 1.41}$$

This therefore gives the spontaneous emission from a single two level system (a single dot) into one polarisation as,

$$R^e_{spon}(\hbar\omega) = \frac{8n\omega}{3\pi\hbar c^3\varepsilon_0}\left(\frac{e}{2m_0}\right)^2 \gamma M^2 \left\{\int F_1(r)^* F_2(r) d^3r\right\}^2 [f_1(1-f_2)] L(E_i,\hbar\omega) \qquad \textbf{Equation 1.42}$$

To determine the total spontaneous emission from an ensemble of dots the above expression is summed over all dots.

$$R^e_{spon}(\hbar\omega) = \frac{8n\omega}{3\pi\hbar c^3\varepsilon_0}\left(\frac{e}{2m_0}\right)^2 N\sum_i \gamma M^2 \left\{\int F_1(r)^* F_2(r) d^3r\right\}^2 [f_1(1-f_2)] P(E_i) L(E_i,\hbar\omega)$$

Equation 1.43

where the N gives the number of dots and $P(E_i)$ is a Gaussian distribution describing the inhomogeneous broadening of the dots.

1.10 The Inversion Factor

The probability of occupation for the upper and lower states is used in the expressions for the modal gain and the spontaneous emission. The ratio of these two quantities gives an indication as to the degree of inversion in the system. By dividing the total modal gain in the system by the spontaneous emission the following expression is obtained,

$$P_f = \frac{G(\hbar\omega)}{R^e_{Spon}(\hbar\omega)} = \frac{3\pi^2\hbar c^2}{n^2\omega^2}\frac{1}{\omega_{\text{mod}}}\frac{f_1(\hbar\omega)-f_2(\hbar\omega)}{f_1(\hbar\omega)(1-f_2(\hbar\omega))} \qquad \textbf{Equation 1.44}$$

Apart from the occupation probabilities all the quantities on the right hand side of equation 1.43 are known values (are constants or can be calculated). As such if the modal and spontaneous emission can be measured, their ratio will give an indication as to the degree of inversion across the system. The final term containing the occupation probabilities can range from a value of 0 to 1. A value of unity can be achieved if f_1 is equal to one (this will occur if the probability of occupation of an electron in the upper state is one, so all the higher states are full) or if f_2 is equal to zero (the probability of an electron in the lower state is zero, so all the states are empty). Although the system will not be fully inverted until both these conditions are met (when the gain and spontaneous emission will both saturate), a value of unity will cause the ratio of the gain to spontaneous emission to saturate.

If the system can be described by global occupation probabilities which are in quasi-thermal equilibrium, then equation 1.44 can be described by Fermi-dirac statistics of the form,

$$P_f \propto \left(1 - e^{\left(\frac{E-\Delta E_F}{kT}\right)}\right) \qquad \textbf{Equation 1.45}$$

where E is the photon energy and ΔE_f is the quasi-Fermi level separation. Therefore by studying the ratio of the modal gain to the spontaneous emission the form of the carrier distribution can be identified.

1.11 Momentum Matrix Element

The momentum matrix element $|M|^2$ gives the probability of a transition occurring between the conduction band Bloch function and the basis Bloch function. The valence band Bloch functions can be written as the sum of the basis Bloch functions (x, y and z directions).

1.12 Development of InAs Quantum Dot Lasers

Room temperature, ground state lasing from InGaAs quantum dot heterostructures under electrical injection was first demonstrated in 1994 [20]. Low threshold currents (~100 Acm^{-2}) were observed at low temperatures (<150 K) indicating that the dot size distribution is small enough to achieve lasing. However the threshold current showed a dramatic increase as the temperature was increased, reaching values of around 1 $kAcm^{-2}$ at room temperature. The increase in threshold current was due to the thermal escape of carriers to excited states and the wetting layer, reducing the occupancy of the dots and hence the modal gain available. This leads to devices having to be long ~ 4 mm, making them impractical for many applications. Even given this limitation, substantial progress has been made in optimising the performance of quantum dot lasers [41-43] with the lowest reported room temperature threshold current of an InGaAs device of 16 Acm^{-2} [44] being a factor of three lower than InGaAs quantum well devices [45, 46].

Several approaches have been investigated to increase the modal gain in quantum dot systems; these include using wider bandgap materials for the barrier regions to decrease the leakage of carriers to these layers and using tunnelling injection structures [47], which use quantum mechanical tunnelling to inject carriers from a

quantum well directly into the dots. This enables specific dots to be selected due to the tunnelling process, hence reducing the effective inhomogeneous broadening of the ensemble. The total number of dots and hence the number of states available can also be increased by stacking multiple quantum dot layers on top of each other [48]. The performance can also be improved by growing the dots in a quantum well [49,50] (forming a DWELL structure) to increase the barriers around the dots, improve the growth surface and the uniformity. This is achieved by growing a thin layer of material (with a different lattice constant) before the dots and then capping the dots with the same material, hence enclosing them inside a quantum well.

A problem that can follow on from stacking DWELL layers is defect formation resulting from large amounts of strain in the system. The In content in both the dots and the well structures can be close to the critical thickness for defect formation; as the number of layers is increased this amount of strain can further increase resulting in defect and dislocation formation.

One possible way of relieving this problem would be to use wide spacer layers between the DWELLs, allowing the built up strain to relax, by removing the lattice mismatch, before the next DWELL is grown. However, this often proves incompatible when trying to optimise the system for use in laser structures as it leads to wide active regions.

Several groups have recently developed so called annealing techniques to improve multi layer growth in quantum dot devices. The first of these was developed by Ledenstov et al. [51]; in their technique they place a very thin cap of material on top of the dots (typically only 2 to 4 nm). This is then followed by a high temperature evaporation (in excess of 600°C); this evaporation step removes any excess dot material above this cap. Any voids which are created in the cap are subsequently filled by the next growth

step, resulting in a much smoother and more uniform surface on which the dots can grow.

Another technique has been developed by Liu et al. [52], [53] in Sheffield. In their technique each DWELL is separated by a 50 nm GaAs barrier, the first 15 nm of this layer is grown at the standard temperature of 510°C; the temperature is then increased to 580°C for the remainder of the layer, before being reset for the next DWELL. This technique is known as the inclusion of High Growth Temperature Spacer Layers, (HGTSLs). It is these samples that are studied in some detail in chapter three to try and understand the origins of the improvements from modifying the growth of the spacer layers.

2. Experimental Procedures

2.1 Introduction

This chapter will outline the experimental procedures and techniques which were used to obtain the results described in the following chapters.

2.2 IVLT Measurements

The current (I), voltage across (V), and light output (L) from a laser diode were recorded as a function of temperature (T), to allow the threshold current of a laser diode to be determined. These measurements were performed on existing experimental apparatus used existing computer software. The diodes were positioned within a vacuum chamber, which had a neutral density filter acting as a 'window'. An InGaAs photodiode was placed on top of the 'window' to collect the emitted light. Due to cost limitations the photodiode was a small area detector and was therefore aligned for a maximum signal at room temperature before each measurement run. The temperature was changed using a heater, which was computer controlled and a cold finger, which could be lowered into liquid nitrogen; this allowed the temperature to be altered over the range 140 K – 400 K. A complete experiment set-up is shown schematically in Figure 2.1.

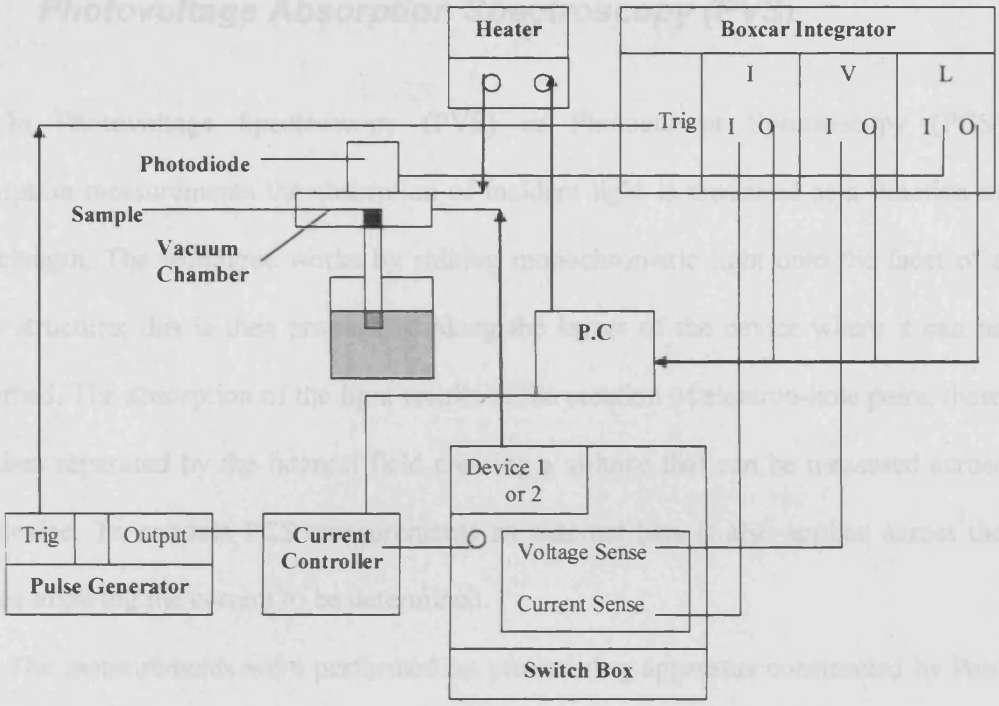

Figure 2.1: - Schematic diagram of experimental set-up for IVLT measurements

The pulse generator produces voltage pulses with a length of 400 ns at a frequency of 1 kHz. These were passed into a current controller, which is a computer controlled potentiometer allowing the amplitude of the current pulse to be varied. The voltage, current and light signals were read into the PC by the boxcar integrator. The boxcar works by a 'sample and hold' technique, where the incoming pulse is measured over a set gate length; the signal is then averaged over many gate lengths before being sent as a D.C. signal to the PC

To perform a temperature run the device was cooled to the lowest temperature required, and measurements were then taken at periodic steps as the device heats up.

2.3 Photovoltage Absorption Spectroscopy (PVS)

In Photovoltage Spectroscopy (PVS) or Photocurrent Spectroscopy (PCS) absorption measurements the absorption of incident light is measured as a function of wavelength. The technique works by shining monochromatic light onto the facet of a laser structure; this is then propagated along the layers of the device where it can be absorbed. The absorption of the light results in the creation of electron-hole pairs; these are then separated by the internal field creating a voltage that can be measured across the device. To conduct PCS measurements an external bias is also applied across the device allowing the current to be determined.

The measurements were performed on pre-existing apparatus constructed by Paul Mogensen. The experimental set-up is outlined in schematic form in Figure 2.2. A white light source is provided from a halogen lamp operating at a voltage of 24 V. The light is chopped and passed into a monochromator, the resolution of which is controlled by the widths of the entrance and exit slits, which were typically set to 100 μm (and given that the grating contains 600 l/mm) giving a resolution of 0.64 nm. The monochromator was connected to the PC, via a stepping motor to allow for wavelength selection. The light was then colliminated and passed through a polarizer; this allows the selection of either Transverse Electric (TE), light polarised perpendicular to the growth plane or Transverse Magnetic TM light, light polarised parallel to the growth plane, which is then focused on to the sample. The signal generated in the device is measured on a lock-in-amplifier, using the reference signal from the optical chopper.

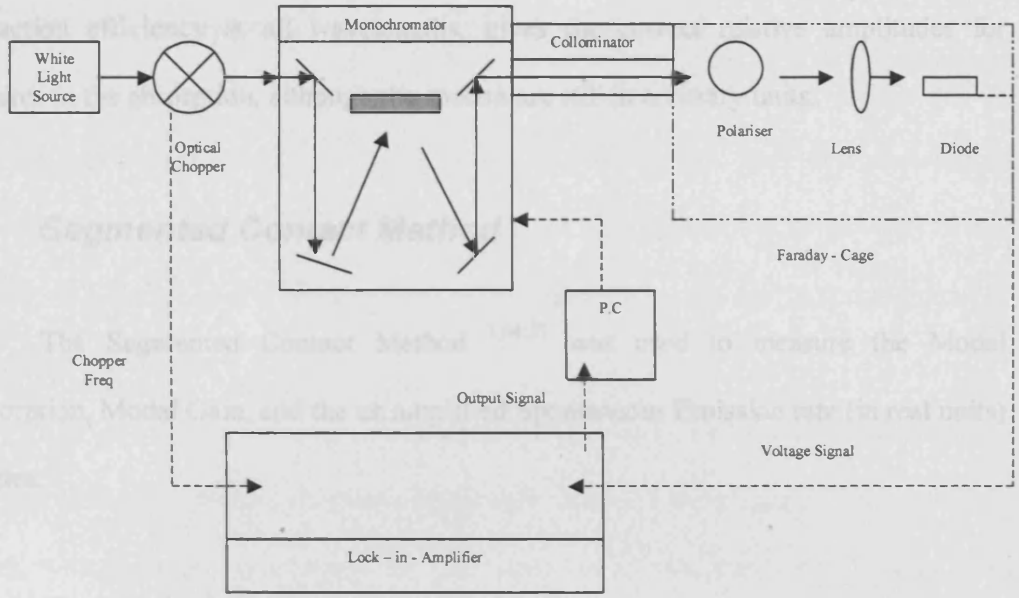

Figure 2.2: - Experimental set - up for Photovoltage experiments

The polariser, lens and device, were all placed inside a metal box acting as a Faraday cage, to provide a shield against both electrical and light interference signals. The sample could be moved in all three translational directions as well as three rotational degrees of freedom to allow alignment for maximum signal.

The signal measured by this system is not the true absorption spectrum due to several factors; firstly the system recorded spectra in arbitrary units, so the magnitude varied with alignment. Also some of the photo-generated carriers will recombine in the device before they are extracted and measured; hence the full absorption may not be measured. Finally the signal will also be affected by the various optical components (the mirrors, grating, collimator, polariser and lens), absorbing / transmitting different wavelengths of light with different efficiencies. To correct for this the spectra were calibrated to correct for this effect. This was achieved by replacing a sample with a photo detector with a known response. The recorded response could then be compared to that expected to obtain a relevant correction factor. The recorded spectra can then be multiplied by this factor to acquire a corrected response, which assuming an equal

extraction efficiency at all wavelengths, gives the correct relative amplitudes for features in the absorption, although the spectra are still in arbitrary units.

2.4 Segmented Contact Method

The Segmented Contact Method [1,54,55] was used to measure the Modal Absorption, Modal Gain, and the un amplified Spontaneous Emission rate (in real units) spectra.

2.4.1 The Technique

The Amplified Spontaneous Emission (ASE) that results from a single pass of light along a length, L of material is given by $I_{ASE}(L)$, which have units of photons per second per unit stripe width per unit energy interval.

$$I_{ASE}(L) = \frac{I_{Sp}(e^{(G-\alpha_i)L} - 1)}{(G-\alpha_i)} \qquad \textbf{Equation 2.1}$$

If different lengths of material are pumped, under the same collection geometry, a set of simultaneous equations can be formed. By algebraic manipulation of these it is possible to derive expressions for the absorption, gain and the spontaneous emission.

In this work I have used devices in which the top electrical contact is divided in to separate electrical injection regions (this will be described in more detail in section 2.6.2), allowing different lengths of material to be pumped. Pumping just the front contact, leads to current injection over a length L and gives a light signal $I_{ASE}(1)$, while pumping the front two sections together (with the same overall current density), results

in an injection over a length 2L and the light spectrum $I_{ASE}(1,2)$. It is also possible to pump the second section by itself and record the resultant spectra, $I_{ASE}(2)$. To ensure that the light measured was genuinely from a single pass (i.e. there is no round trip amplification of the light) there are at least three passive sections at the rear of the device. In addition to this the rear facet was damaged when the device was mounted to suppress any reflections.

The determination of the modal loss, gain, un-amplified spontaneous emission and the calibration factor, all graphs shown are from a 5 layer quantum dot structure which will form the benchmark for the structures in the following chapters. The structure is shown schematically in Figure 2.3 and consists of 5 DWELL layers, where each DWELL is formed by depositing 3.0 ML of InAs, which forms the wetting layer and the dots into an $In_{0.15}Ga_{0.85}As$ quantum well. The DWELLs are then separated by 50 nm GaAs spacer layers and the active region is incorporated into an $Al_{0.4}Ga_{0.6}As$ waveguide.

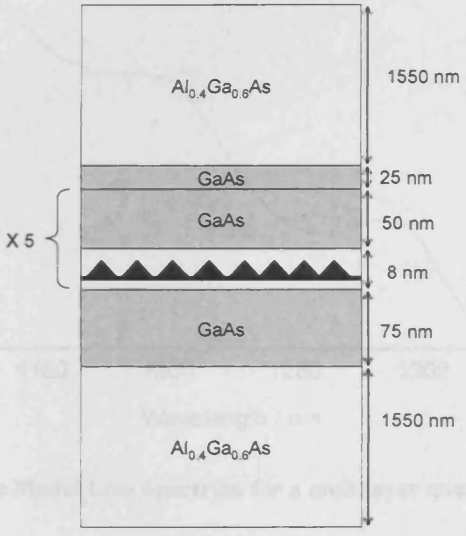

Figure 2.3: - Schematic diagram of quantum dot structure used illustrate measurement techniques.

2.4.2 Modal Loss

The modal loss was measured by comparing the ASE when just the front section is pumped to the spectra obtained when just the second section is pumped (i.e. giving the absorption due to the front section). By looking at the ASE from these two sections the following expression can be obtained for the absorption,

$$(\alpha + \alpha_i) = \frac{1}{L} \ln\left(\frac{I_{ASE}(2)}{I_{ASE}(1)}\right) \qquad \textbf{Equation 2.2}$$

where α is the modal absorption, α_i is the internal waveguide loss and L is the length of the section. As this is a passive measurement of the modal absorption in the un pumped section the spectrum obtained is independent of the current used to generate the light.

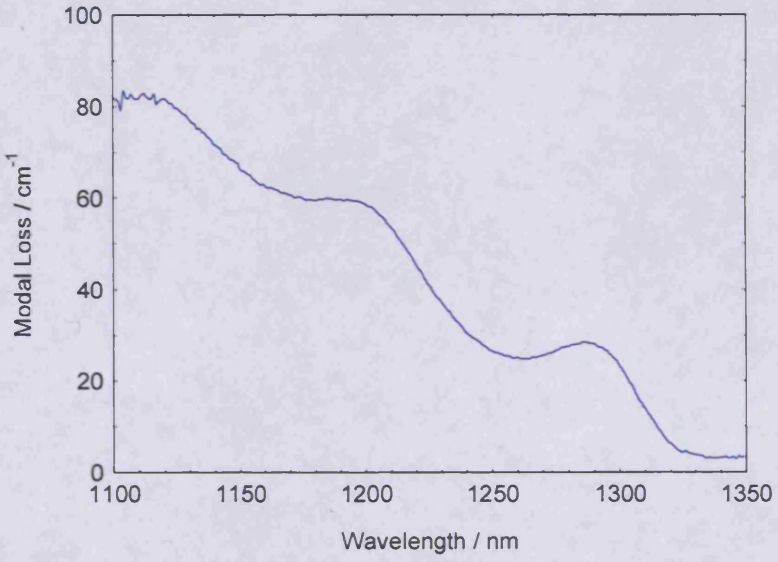

Figure 2.4: - Example of a Modal Loss Spectrum for a multilayer quantum dot sample.

Two peaks can be observed centred at 1290 and 1200nm, these can be attributed to ground and excited state quantum dot transitions. The region where the curve goes flat at long wavelength gives the value of the internal waveguide loss α_i. This is

assumed to be independent of wavelength; therefore the same loss is experienced over the whole spectrum; however it can only be measured at long wavelengths due to the absence of other loss processes at these energies.

Measurements of the modal absorption can be obscured by internal fields across the devices or due to impurities incorporated to the active region during growth. The effect of an internal field across the structure will alter the overlap of the electron and hole wavefunctions, decreasing the absorption. While the presence of impurities can result in the occupation of states without electrical or optical pumping and as such reduce the measured absorption due to state blocking.

To study these effects absorption measurements can be performed with a static D.C. bias applied across the section under test.

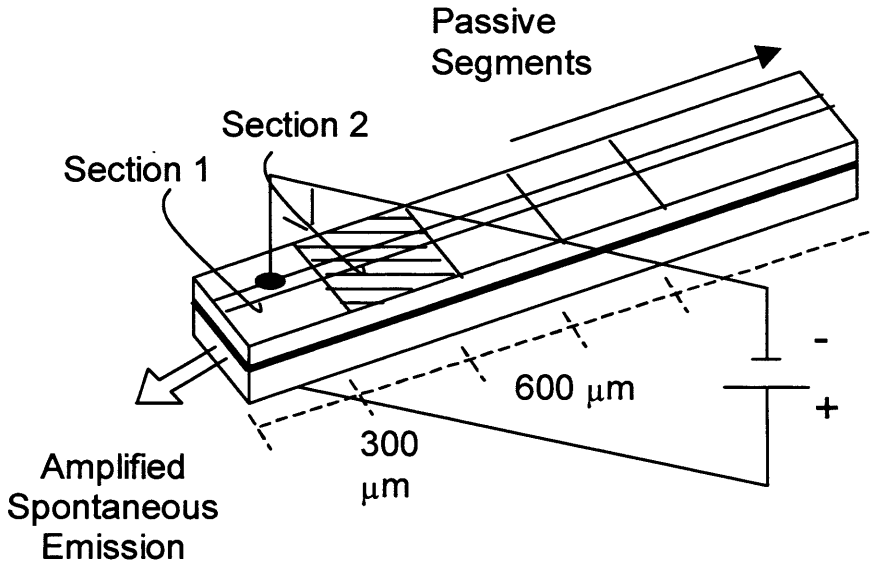

Figure 2.5: - Schematic diagram of a multisection device with a D.C. bias applied.

While the second section is being pumped the front section experiences a D.C. voltage to remove any excess carriers (introduced through impurities) and / or to counter any internal field, allowing the true absorption to be measured. For parity while

the front section is being electrically pumped the second section is also placed under a D.C. voltage.

2.4.3 Modal Gain

The modal gain can be obtained by comparing ASE from different pumped lengths, this can be achieved here by looking at $I_{ASE}(1)$ with $I_{ASE}(1,2)$, i.e. the light from lengths L and 2L, this gives the following expression,

$$(G-\alpha_i)=\frac{1}{L}\ln\left(\frac{I_{ASE}(1,2)}{I_{ASE}(1)}-1\right) \qquad \textbf{Equation 2.3}$$

where G is the modal gain and the other symbols have their usual meaning. We can therefore record gain spectra as a function of drive current.

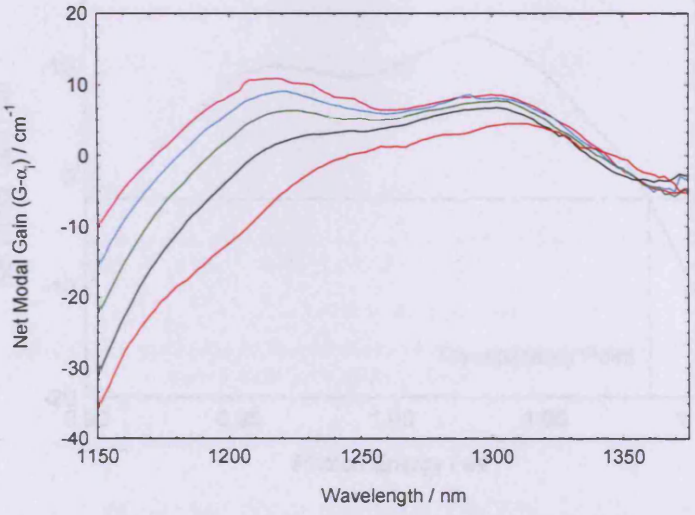

Figure 2.6: - Example Net Modal Gain Spectra for the same multi layered quantum dot sample as shown in figure 3.

Gain peaks can be observed from both the ground and excited state transitions, with the overall peak initially on the ground state and then switching to the excited state

as the current density is increased. The region at long wavelength where the curves come together and go flat again gives the waveguide loss and should be the same as that measured in the absorption measurement for the same device. The peak gain values can be plotted as a function of current density; these can then be compared to laser points to confirm the accuracy of the measurement. The laser points are given by the threshold current density and the threshold loss (as given in chapter 2).

As well as allowing us to determine the gain as a function of the current we can also determine the quasi-Fermi level separation from these spectra. The transparency point is defined as the point where the material goes from being an absorbing to a gain medium (i.e. $G = 0$ or $G - \alpha_i = -\alpha_i$). This can be determined from where the gain curves cross the value of α_i at short wavelength (high energy). If the device is in thermal equilibrium then the transparency point is the quasi-Fermi level separation.

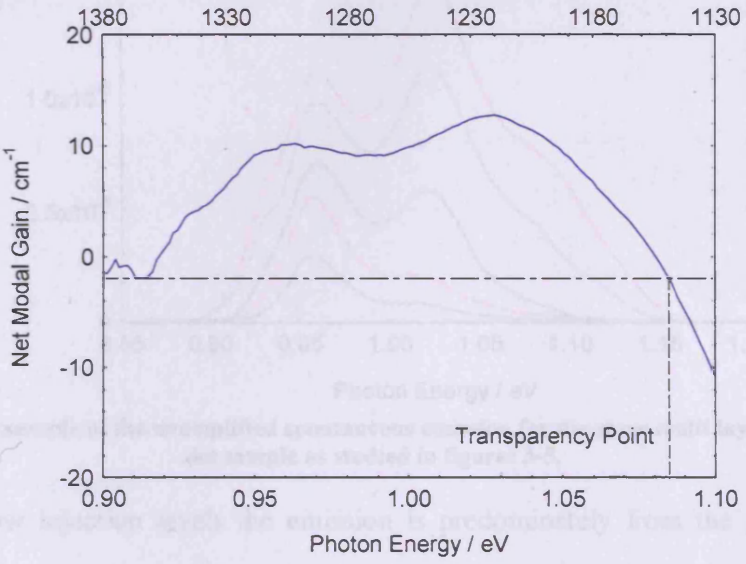

Figure 2.7: - An Example gain spectrum showing the determination of the transparency point for a multi layered quantum dot sample.

2.4.4 Spontaneous Emission

Apart from the net modal gain, equation 2.1 contains another unknown, the unamplified spontaneous emission from the device. By again looking at the ASE from different lengths of pumped material it is possible to determine an expression for the spontaneous emission.

$$I_{Spon}^{Meas} = \frac{1}{L}\ln\left(\frac{I_{ASE}(1,2)}{I_{ASE}(1)} - 1\right)\left(\frac{I_{ASE}(1)^2}{I_{ASE}(1,2) - 2I_{ASE}(1)}\right) \qquad \textbf{Equation 2.4}$$

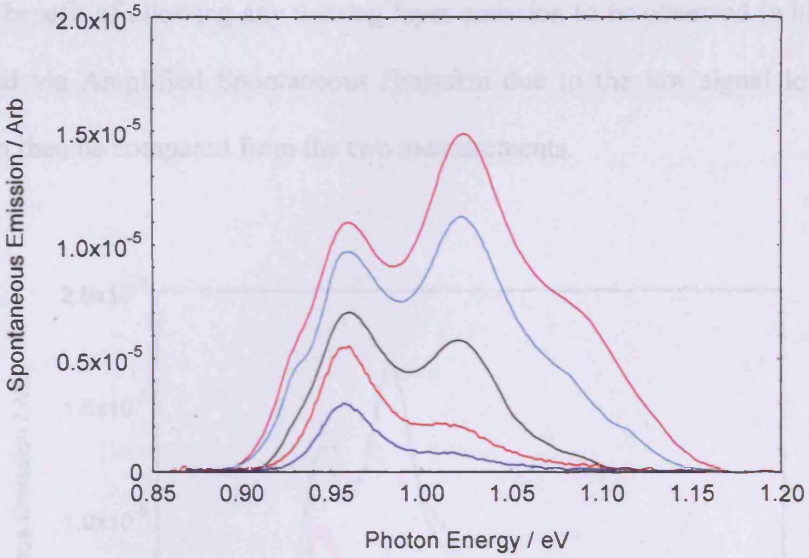

Figure 2.8: - Example of the unamplified spontaneous emission for the same multi layered quantum dot sample as studied in figures 3-5.

At low injection levels the emission is predominately from the ground state centred at 0.957 eV. As the current is increased emission is also observed from the excited states at energies of 1.023 and 1.079 eV. Whereas the modal absorption and gain obtained in equations 2.2 and 2.3 only involved a ratio of the ASEs; allowing the units to cancel and both quantities to be determined in units of reciprocal length. The

expression for the unamplified spontaneous emission is more complicated and has to be expressed in units of the ASE.

The shape of the unamplified spontaneous emission, can be checked by looking at the form of the emission from the top of the device [55]. This can be done by mounting a device, top side up; the light is then collected from the trench between the first two sections. This is akin to collecting the light from a 4 μm wide window in the oxide stripe. In this measurement it is important that the carrier density is distributed evenly between the sections to give homogenous and correct spectra. To ensure this occurs the near field from the 'window' is checked using an infrared camera. As well as validating the measurements from the end of the device, spontaneous emission from the top has the added benefit of allowing any wetting layer emission to be observed (which cannot be resolved via Amplified Spontaneous Emission due to the low signal levels). The spectra can then be compared from the two measurements.

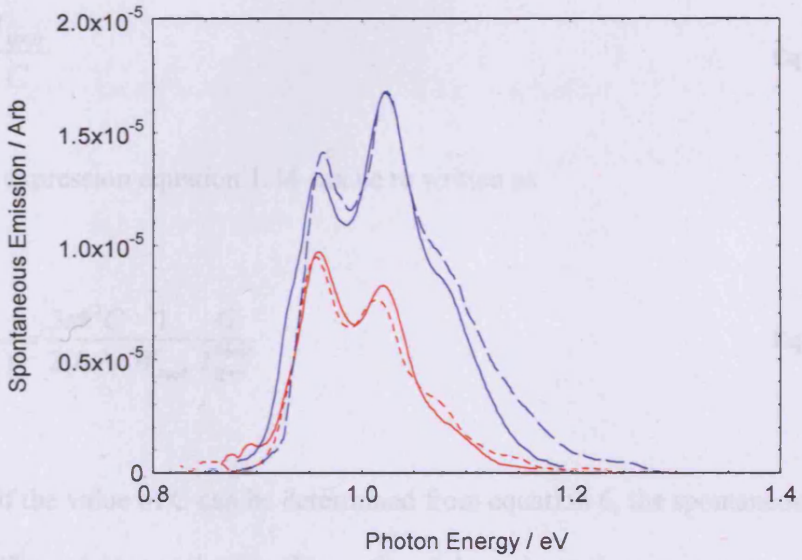

Figure 2.9: -Comparison of the spontaneous emission from the edge (solid lines) and from the top (dotted lines) for the same multi layered quantum dot sample as studied in figure 6.

The spectra from the top and the edge are reasonably similar; there is more emission at higher energies in the emission from the top (especially at higher driver currents). This difference is most likely caused by the low signal levels in the ASE at these energies, resulting in a reduced accuracy at these points. A bump can also be seen in the emission from the top centred at 1.262 eV (corresponding to a wavelength of 983 nm). This transition can be attributed to the emission from the wetting layer, and the integrated area under this region, accounts for approximately 1 % of the total area.

2.4.5 The Calibration Factor

As shown in equation 1.44, the ratio of the gain to the spontaneous emission gives an expression for the ratio of the occupation probabilities. This relation can be used to calibrate the spontaneous emission into real units. The real spontaneous emission is related to the measured quantity by a calibration factor, C, given by.

$$I_{Spon}^{Meas} = \frac{I_{spon}}{C} \qquad \textbf{Equation 2.5}$$

using this expression equation 1.44 can be re written as

$$\frac{f_1 - f_2}{f_1(f_2 - f_1)} = \frac{3\pi\hbar^3 C}{2(h\nu)n} \frac{1}{W_{\mathrm{mod}}} \frac{G}{I_{Spon}^{Meas}} \qquad \textbf{Equation 2.6}$$

therefore if the value of C can be determined from equation 6, the spontaneous emission can be calibrated into real units. The ratio of the gain to the spontaneous emission is plotted in Figure 2.9

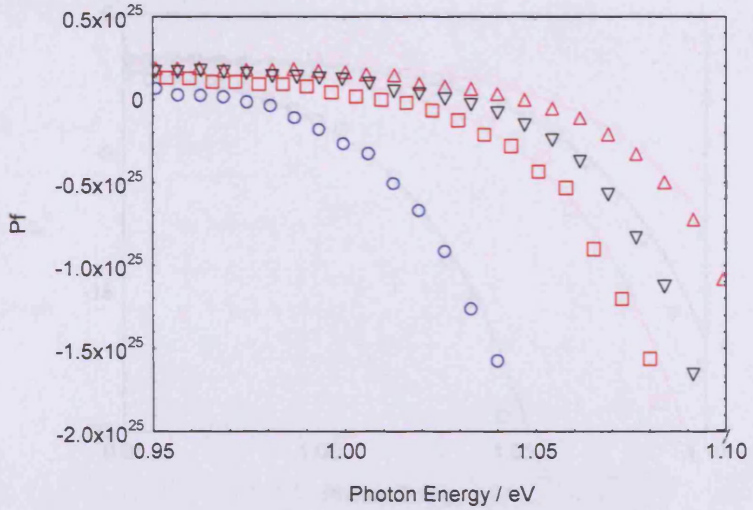

Figure 2.10: - Example of the Pf factor

As was also stated in chapter 1, if f_1 is equal to one, or f_2 is equal to zero then the ratio of the occupation probabilities tends to unity and saturates. At low photon energies the ratio of the gain and spontaneous emission clearly saturates, (as such) the ratio of the occupation probabilities in equation 2.6 can be set to unity and the value of C can be determined.

To help determine the value of the RHS of Equation 2.5 when the P_f saturates we can exploit the fact that if the sample is in quasi-thermal equilibrium then the data can be fitted by Fermi Dirac statistics as was explained in chapter 1.

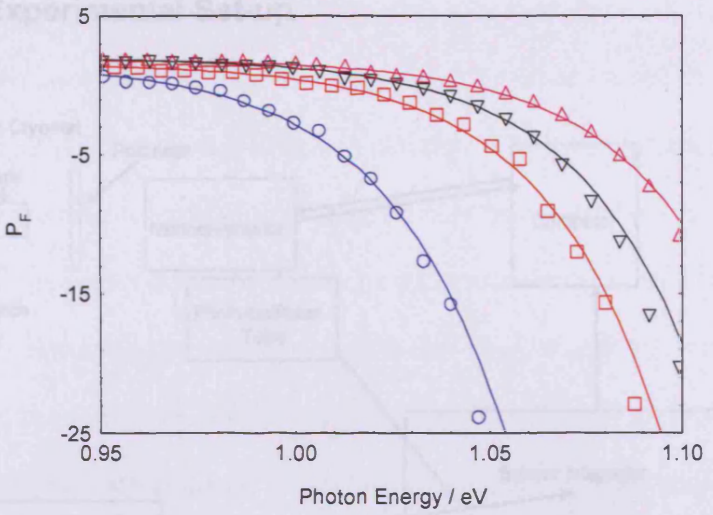

Figure 2.11: - Example of P_f functions with thermal fits

The open symbols give the experimental points, while the solid lines give the fits from Fermi-Dirac statistics. From the fits an accurate value for the calibration constant can be determined.

Once the spontaneous emission is in real units it is possible to determine the radiative current density, J_{Rad},

$$J_{Rad} = e\int I_{Spon} dh\nu \qquad \textbf{Equation 2.7}$$

where I_{Spon} is in units of $cm^{-2}eV^{-1}sec^{-1}$. From this it is possible to determine the internal radiative efficiency, which is defined as the ratio of the total radiative current to the total drive current.

$$\eta = \frac{J_{Rad}}{J_{Drive}} \qquad \textbf{Equation 2.8}$$

Likewise we can determine the total non-radiative current density, which is just the difference between the total current density supplied and the radiative current density (this is the case as stimulated emission is negligible in this experiment[1]).

$$J_{Non-Rad} = J_{Drive} - J_{Rad} \qquad \textbf{Equation 2.9}$$

2.4.6 The Experimental Set-up

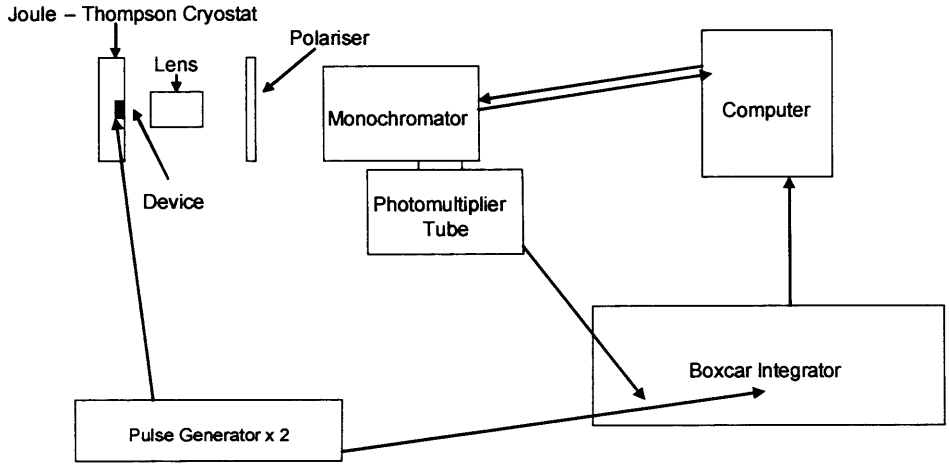

Figure 2.12: - Schematic of experimental set up for measurements using the Segmented Contact Technique

The experimental apparatus used for these measurements were constructed by Dr Craig Walker and me. The computer software to control the apparatus and measure the light signals was adapted by myself from existing code. The device is placed in Joule – Thompson cryostat, which is connected to a vacuum system comprising both a rotary and a diffusion pump, allowing pressures of around 10^{-5} torr to be achieved. The cryostat was also attached to a temperature sensor and controller which, along with compressed nitrogen and a heater, allows temperatures over the range ~ 100 – 400 K to be obtained.

Two pulse generators were used to enable the segments to be pumped individually. The value of the currents was monitored by a boxcar to allow the computer to accurately determine and set the currents in each section. The light is focused through a lens and then passed through a polariser to allow the selection of either TE or TM polarisation before being passed through a monochromator (with a grating containing 600 l/mm), which was computer-controlled to allow the selection of the

desired wavelength. Again the entrance and exit slits were typically set to 100 μm resulting in a resolution of 0.64 nm. The light signal was then passed from to a Photo-multiplier tube (PMT), where the light was detected. The signal is then passed to the boxcar so that it can be sampled and averaged before being sent back to the computer. The current pulses were overlapped in time, so that measurements could be made on the light signals from section one and section two (for loss) or sections one and two (for gain) at almost identical times. To allow these measurements to be made the light signal from the PMT is sent independently to three different sampling gates on the boxcar.

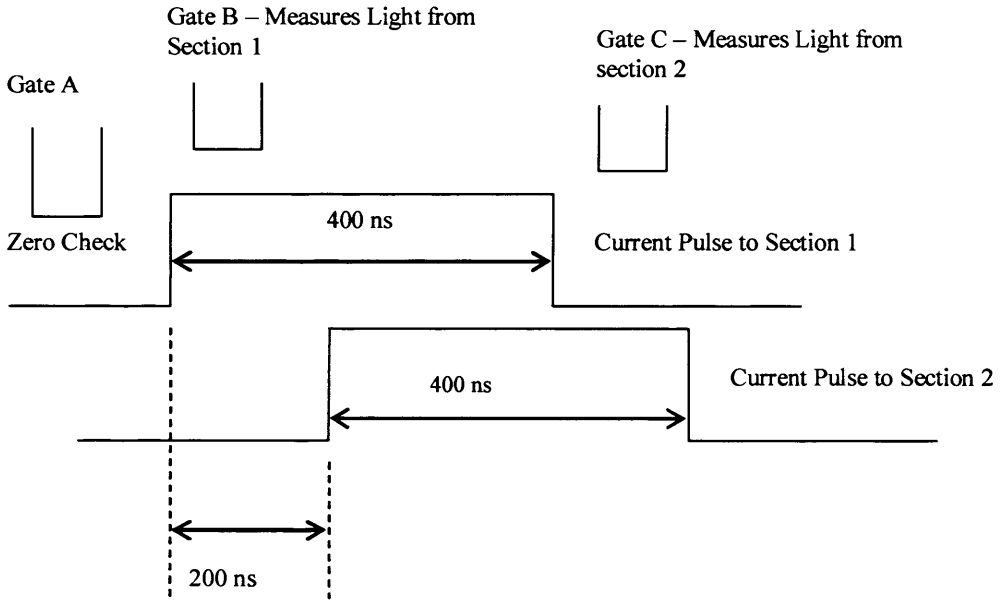

Figure 2.13: - Overview of the current pulses and boxcar gates for Absorption measurements

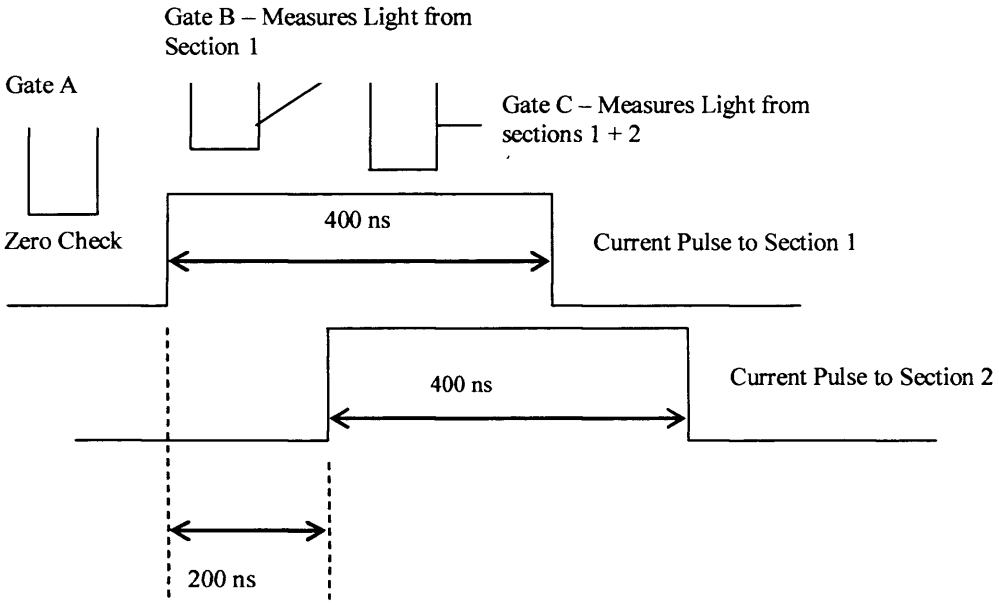

Figure 2.14: Overview of the current pulses and boxcar gates for Gain and Spontaneous Emission measurements

In both configurations Gate A is used to measure the 'zero' level of the light before the incident pulses. This reading is then subtracted from gates B and C in both cases to obtain the true light signal. Gate B is positioned over section one in both instances. This means that this gate measures the light due to the current pulse in the front section. The third gate is positioned over the light signal from section two alone in Figure 2.12, allowing a measurement of the absorption to be made. In Figure 2.13 it is positioned to measure the light due to both sections being pumped at the same time, hence allowing measurement of the gain and spontaneous emission.

By measuring at two gates nearly simultaneously the time required to obtain a measurement of the absorption or gain is halved compared to recording the ASE independently. The accuracy of the system is therefore increased as any slight variations in alignment, temperature, etc. will be present in both ASE readings at the same places and as the gain and absorption expressions involve a ratio of the ASE these inconsistencies will cancel out. If the signals were recorded separately these

inconsistencies would arise at different points in each spectrum causing inaccurate absorption or gain data to be obtained.

As in section 2.3 the ASE measured is in unknown units due to the different amounts of transmission and absorption from the various optical components. However for gain and absorption measurements this is not an issue as the expressions for both just involve a straightforward ratio of ASEs, allowing the quantities to be given in absolute units. However the expression for the spontaneous emission is more complex and is given in the units of the ASE. Therefore a spectral calibration needed to be performed before measurements of the spontaneous emission could be made. This was done by passing a light from a source (a halogen bulb) with a known spectral response through the system and measuring the output and then comparing to the expected values. For safe operation of the PMT system the average output current must remain below 1 μA. The halogen lamp used for the spectral calibration outputs 45 W and as such is likely to exceed this limit. Therefore the best approach to overcome this is to 'chop' the light so that it generates an A.C signal. This was done using a chopper wheel and lock in amplifier to record the system response.

2.4.7 Device Checks

It is important in this measurement to ensure that the device being measured is operating correctly and therefore going to give true results. Initially several visible checks can be made with the use of an optical microscope. It is important to ensure that the front facet consists of a 'smooth' (mirror like) cleave, as otherwise light may be refracted and reflected away from the detector. The front two sections also need to be measured to ensure they really are the same length. Next the device needs to be tested electrically; this is done by measuring the I-V characteristic (as described in section 2.2)

of each section. The two traces should be identical, and if they are not it implies that the resistance in the two sections (and/or of the bonded wires) is not the same. This could therefore result in the sections not being pumped equally. The inter-contact resistance between the two electrically injected regions also needs to be measured. This needs to be as high as possible to limit any current leakage between the sections which would potentially unbalance the currents. However as the inter-contact region is formed by etching through the top cap a resistance greater than 1 kΩ typically signifies that the etch has gone too deep and has disturbed the waveguide cladding. Therefore devices were typically selected with inter contact resistances of 200 – 600 Ω. A final check that can be performed involves using a free space camera to look at the near field from the device. The camera used consisted of an electrically cooled 2 dimensional InGaAs photodiode array. The near field should be homogenous to show that the current is being pumped uniformly across the stripe. The camera can also be used to measure the FWHM of the near field, giving an idea as to the amount of current spreading (this can then be used later to convert currents into current densities). The degree of current spreading should also be the same in both sections. If this is not the case it would imply that the sections were not being equally pumped at a fixed current.

2.5 Three Section Vs. Two Section Technique

It has recently been reported that the standard multisection technique described above can be inaccurate when applied to measurements on quantum dot structures under certain collection geometries[56,57]. The reason for this claim is due to 'un-pumped' light which is collected by the measurement system. The 'un pumped' light is caused by light beams that do not travel the full length of the stripe down a section and therefore are light rays that diverge at large angles. The collection of these rays results in the gain

being under calculated in the analysis. This is more problematic in quantum dot structures due to the low values of modal gain achieved. So any miscalculation will be a large fraction of the overall gain. To compensate for this a modified version of the segmented contact method has been developed, where the ASE is collected from the front 3 sections [56]. All the light from the front section (including the 'un pumped' light) can then be corrected for resulting in the true values of the gain and absorption being obtained.

It has previously been shown [58] that the problem of collecting 'un pumped' light can be removed by restricting the collection angle of the light. It was shown that if the light is collected from an angle of 8.4 ° or less from the centre of the facet then all the light rays collected have travelled the full length of the stripe. For this reason the lens used in the experimental set – up had was positioned 50 mm from the device and had a width of 12 mm, this then limited the collection angle from the edge of the device to 6.9^0.

To ensure that this collection problem had been fully corrected for with this collection geometry measurements were made on the same device using both the standard (as described in section 2.4) and the modified technique so that the absorption and gain spectra could be compared. As the apparatus is designed and set–up to operate using the standard two section technique, several modifications had to be made. These involved introducing a switch box from one of the pulse generators to enable two sections to be pumped from the one source. The code was also altered so that the pulse generator supplying the switch box gave twice as much current as the single source. Also due to there only being three boxcar channels to read the light signals the measurements had to performed in two runs with the gates positioned in different places. As this increased the time required to perform the measurement, at least one of

the gates was kept in the same position for the two runs to ensure the alignment had not altered.

Example absorption and gain spectra are shown comparing the two techniques.

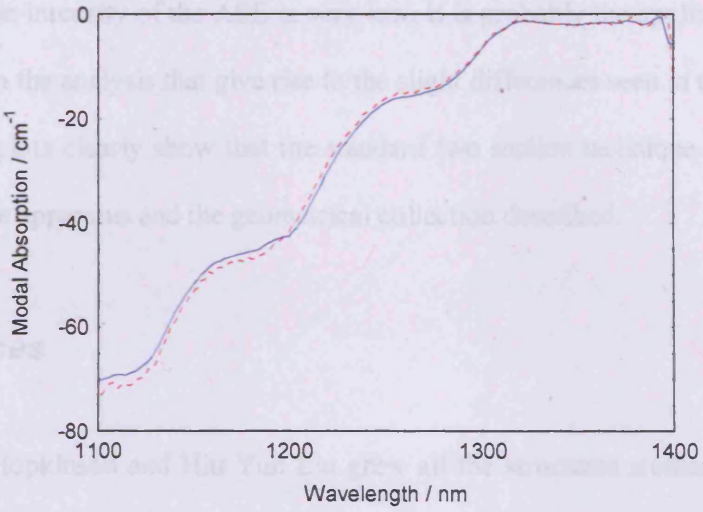

Figure 2.15: - Modal absorption spectra at 300 K under a drive current density of 444 Acm-2 using the standard technique (solid line) and the three section technique (dashed lines).

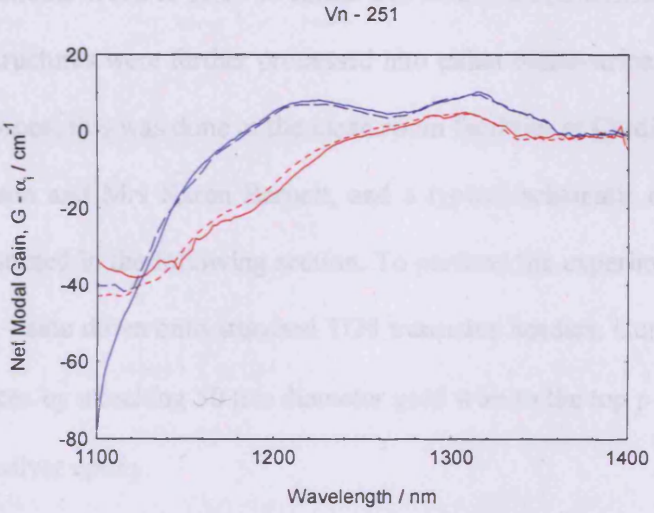

Figure 2.16: - Modal Gain spectra at 300 K for drive current densities of 222 and 444 Acm^{-2} using the standard technique (solid lines) and the three section technique (dashed lines).

Both plots clearly show that there is no obvious difference between the techniques, as expected from restricting the collection of the light. The absorption spectra in Figure 2.14, show excellent agreement over the whole wavelength range

(with a variation of < 2 cm^{-1} at any point); they also give identical values for α_i of 2cm^{-1}. The modal gain spectra in Figure 2.15, also give an excellent agreement. Here the curves only differ significantly at the lowest wavelengths (< 1150 nm); at these wavelengths the intensity of the ASE is very low. It is probably the application of these small signals in the analysis that give rise to the slight differences seen in the spectra.

These plots clearly show that the standard two section technique is appropriate for use with the apparatus and the geometrical collection described.

2.6 Devices

Mark Hopkinson and Hiu Yun Liu grew all the structures studied in this work via Solid Source Molecular Beam Epitaxy at the EPSRC III-V Facility at the University of Sheffield. All the structures had Quantum Dots as an active region, which were grown inside Quantum Wells to form so called Dot-In-a-Well (DWELL) structures (see chapter 2).The structures were further processed into either oxide-stripe laser devices or multi-section devices; this was done at the clean room facilities at Cardiff University by Dr John Thompson and Mrs Karen Barnett, and a typical schematic diagram of each device will be outlined in the following section. To perform the experiments the devices were mounted n – side down onto standard TO5 transistor headers. Current was passed through the devices by attaching 50 μm diameter gold wire to the top p metallization of the devices with silver epoxy.

2.6.1 Oxide Stripe Lasers

A schematic diagram of a typical oxide stripe laser is shown in Figure 2.16. To form the top contact an oxide layer is deposited during fabrication on the top of the

device, with a 50 μm stripe where the oxide is removed running through the middle of this to allow spatially confined current injection. A gold contact layer is then deposited on the top of the device to allow current to be injected. The devices were used as cleaved (i.e. with no additional reflection coatings on the facets); light is then emitted from both ends of the structure.

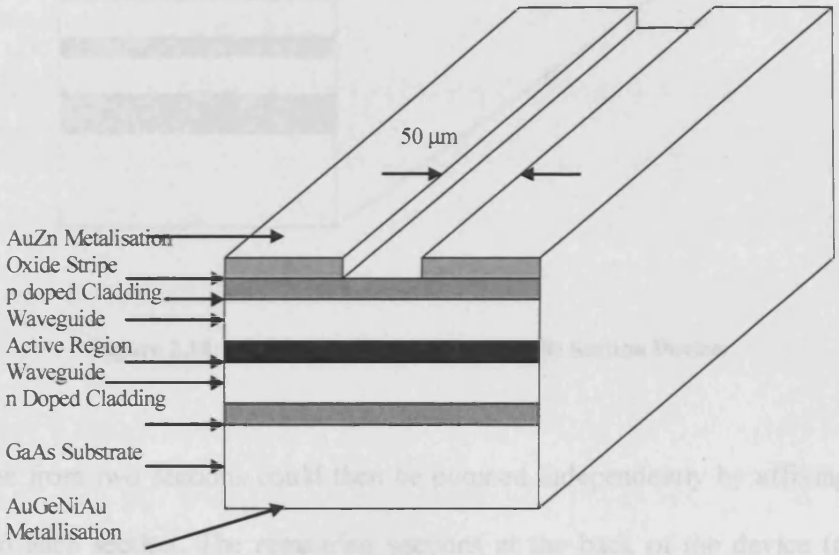

Figure 2.17: - Schematic Diagram of a typical Oxide Stripe Laser Device

2.6.2 Multi Section Devices

A schematic diagram of a multi section device is shown in Figure 2.17. These devices were used to obtain the modal absorption and gain data presented in this work as well as the spontaneous emission data. The structure for the multi section devices is the same as for the oxide stripe laser case discussed above, however the top contact is separated into electrically isolated contacts (to allow each section to be pumped separately) by etching periodic 4 μm gaps every 300 μm along the length of the device in the metallisation and in the top contact GaAs.

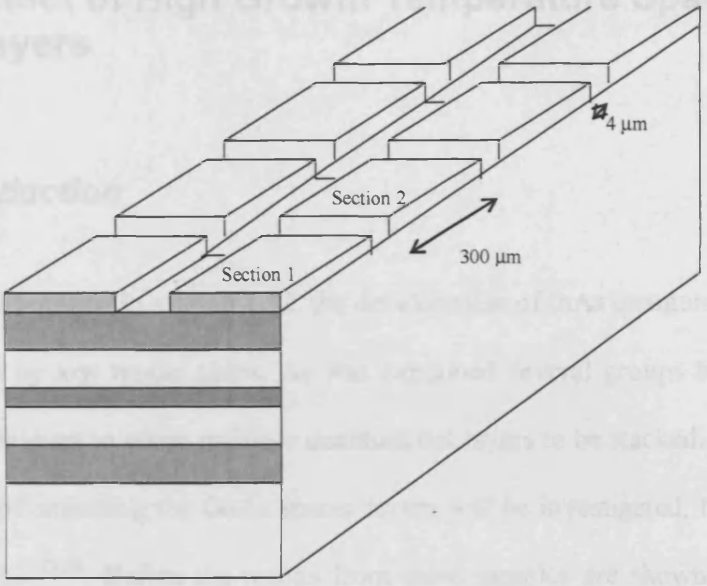

Figure 2.18: - Schematic Diagram of a Multi Section Device.

The front two sections could then be pumped independently by affixing a gold wire on to each section. The remaining sections at the back of the device (typically another 3 sections) were used as a passive absorber, so that the amplified spontaneous emission measured is that due to a single pass. To further suppress any round trip amplification of the light, the rear facet was damaged prior to mounting.

3. Effect of High Growth Temperature Spacer Layers

3.1 Introduction

As was outlined in section 1.12, the development of InAs quantum dot lasers has been hindered by low modal gains. As was explained several groups have developed annealing techniques to allow multiple quantum dot layers to be stacked. In this chapter the influence of annealing the GaAs spacer layers will be investigated, by studying the use of HGTSLs [52,53]. Before the results from these samples are shown and discussed initial AFM, TEM, and threshold current measurements will be discussed.

Both devices consisted of 5 DWELL layers, where the DWELL consisted of 3.0 mono layers of InAs grown on top of 2 nm of $In_{0.15}Ga0_{.85}As$ and then capped with 6 nm of $In_{0.15}Ga_{0.85}As$. The DWELLs were then separated by 50 nm of GaAs. For the standard sample the GaAs layer was grown at 510^0C and for the HGTSL the initial 15 nm of the GaAs are grown at 510^0C, before the temperature is increased to 580^0C for the remaining 35 nm before being decreased back to 510^0C for the next DWELL layer[52], this information is summarised in Table 3.1. The active region was incorporated into an $Al_{0.4}Ga_{0.6}As$ waveguide structure.

Name	Growth temperature of initial 15 nm of GaAs Spacer Layer (^{0}C)	Growth temperature of remainder of GaAs Spacer Layer (^{0}C)
Standard Sample	510	510
HGTSL Sample	510	580

Table 3.1: - Description of the samples studied

Transmission Electron Microscope (TEM) measurements performed at Sheffield University for the standard sample showed threading dislocations originating in the second layer and spreading through the device, however the inclusion of the HGTSL was shown to eliminate these [59]. Atomic Force Microscope (AFM) studies were also conducted on uncapped samples of the HGTSL sample at Sheffield University and showed a dot density of 4.3 x 10^{10} cm^{-2} [52]. The AFM measurements allowed surface morphology images to be generated for the structures. Without HGTSLs the surface was found to be rough, containing a series of mounds and pits. The inclusion of HGTSLs removed these features leaving the surface morphology similar to the initial GaAs buffer. Laser threshold measurements were conducted on 5 mm long devices on each structure. The standard sample failed to show lasing above 190 K, whereas the use of HGTSLs, produced ground state lasing to well over 300K, with a continuous wave room temperature threshold of 39 Acm^{-2}, with a wavelength of 1.31 μm [52,53].

3.2 Modal Absorption Data

The modal absorption spectrum obtained from each structure is shown below.

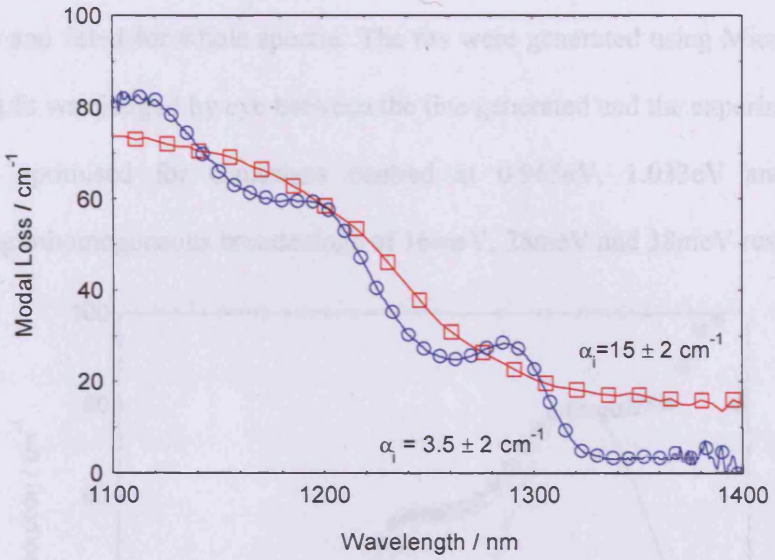

Figure 3.1: - Modal Loss Spectra for the standard sample (squares) and the HGTSL sample (circles).

There are several major differences between the two spectra, which will now be discussed. Firstly the internal scattering loss, α_i for the structures decreases from 15 cm^{-1} down to 3.5 cm^{-1}, giving experimental evidence of the reduced number of defects in the sample. Secondly a lot of information can be deduced by looking at the shape of the spectra in each case. There are no definite features in the spectra for the standard sample resulting in a general absorption edge. On the other hand the HGTSL sample shows 3 absorption peaks in the spectra, which can be attributed to the transitions within the quantum dots. This suggests that the dots formed via the inclusion of HGTSLs experience less inhomogeneous broadening during their formation leading to a more uniform dot distribution and clearer absorption features.

This hypothesis can be studied in more detail, by fitting Gaussian distributions for each absorption peak (once the value of α_i has been removed), each Gaussian distribution then represents a broadened quantum dot transition, and these can then be summed up and fitted for whole spectra. The fits were generated using Microsoft excel and the best fit was judged by eye between the line generated and the experimental data. The fit is optimised for Gaussians centred at 0.965eV, 1.033eV and 1.117eV experiencing inhomogeneous broadenings of 16meV, 28meV and 38meV respectively.

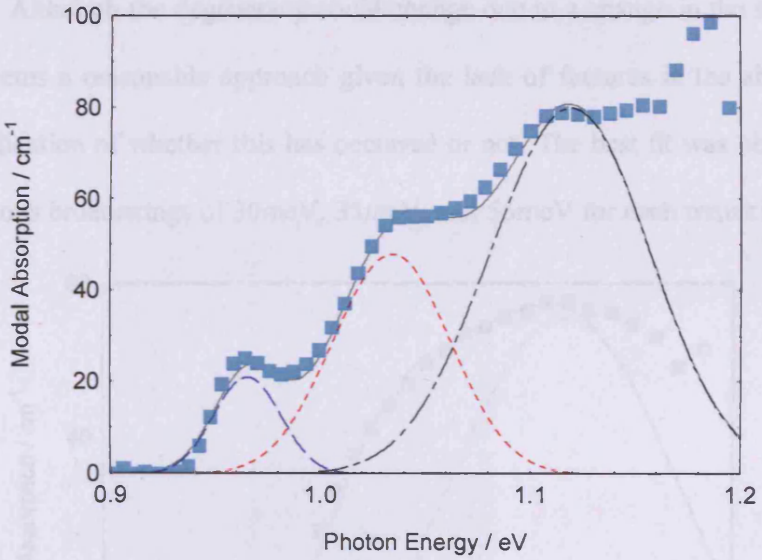

Figure 3.2: - Modal Absorption and Fitted Gaussian Functions for the HGTSL sample.

The square points represent the experimental data, and the dashed (solid) lines show the individual (combined) fits. The area under each individual Gaussian is proportional to the number of states at this transition energy. The ratio of the areas under the two lowest energy Gaussians is 1:(3.7±0.2). This is close to a ratio of 1:4 suggesting that the excited state has fourfold degeneracy, instead of the simple twofold degeneracy that may be expected due to the size / shape of the dot. Fourfold degeneracy has been reported previously [60-63] in In(Ga)As Quantum Dot systems for both

experimental and theoretical considerations and arises due to rotational symmetry and spin degeneracy in the excited state.

The absorption spectrum for the standard sample appears more difficult to fit, given that there are no definite absorption peaks. However as you would expect the dots to be similar it seems reasonable to use Gaussians centred at the same energies. The inhomogeneous broadening and scaling heights of each transition are used as fitting parameters, although the areas under the two lowest transitions are forced to stay in the ratio 1:3.75. Although the degeneracy could change due to a change in the shape of the dots, this seems a reasonable approach given the lack of features in the absorption to give any indication of whether this has occurred or not. The best fit was obtained with inhomogeneous broadenings of 30meV, 35meV, and 55meV for each transition.

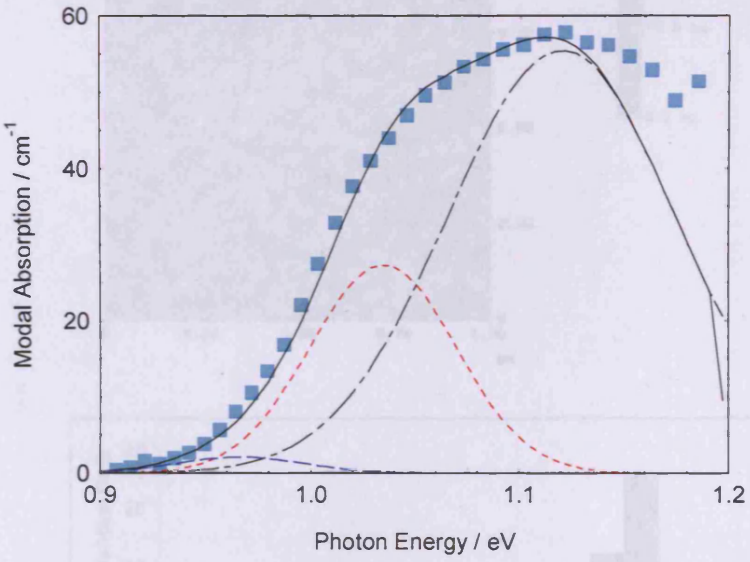

Figure 3.3: - Modal Absorption Spectra and Fitted Gaussian Functions for the standard sample

Again the square points show the experimental data and the dashed (solid) lines show the individual (combined) fits. Although the overall fit is not so good this time it still shows a reasonable approximation to the experimental data. For the HGTSL and the standard sample the ratio of the ground to the third state is 1:(9.1±0.3) and

1:(7.8±0.4) respectively. As well as clearly being different, which seems unreasonable given that the ground to excited state degeneracy was forced to stay the same; neither number has any physical justification. A further problem with this approach is the different broadenings required for each state. For both samples there is a large increase in the inhomogeneous broadening used for the excited state(s) when compared to the ground state Gaussian. Although a slight increase may be expected due to the dimension of the dots changing at different heights, the increase seen here is very substantial and lacks any physical reasoning. A previous AFM study[53] on these samples revealed a bi modal distribution of dot sizes, consisting of a majority of large dots, with a subset of smaller dots.

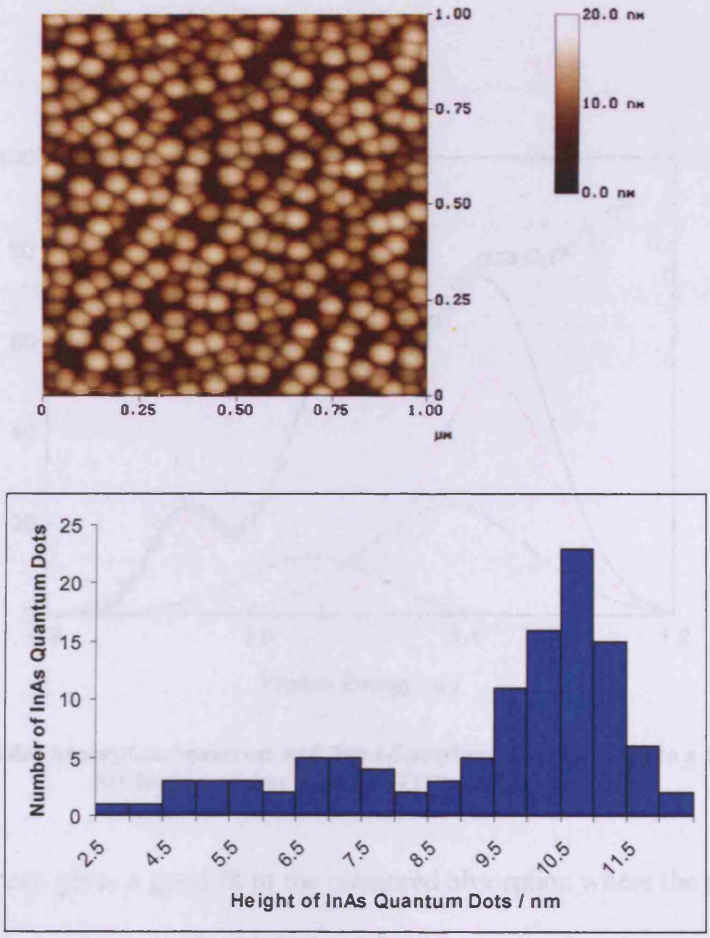

Figure 3.4: - AFM image and histogram of dot sizes. Image and data supplied by H. Y. Liu, Sheffield University.

The AFM data show the majority of the dots centred at a height of 11 nm, with a subset of smaller dots, centred around 7 nm. It was shown that the use of HGTSLs results in a similar distribution in each layer, whereas in the standard sample the number of large dots decreased while the density of smaller dots increased in the upper layers. Bi-modal distributions have been reported elsewhere[64-67] for InAs quantum dots grown by MBE techniques. It has also been shown that the ground state of the smaller dots can overlap the excited state of the larger dots[66,67], making it difficult to resolve the two subsets. To study the possibility of a changing bimodal distribution contributing to the observed absorption curves the data is fitted with five Gaussians due to ground and excited state(s) from each subset of dots, the best fit for the HGTSL sample is shown in Figure 3.4

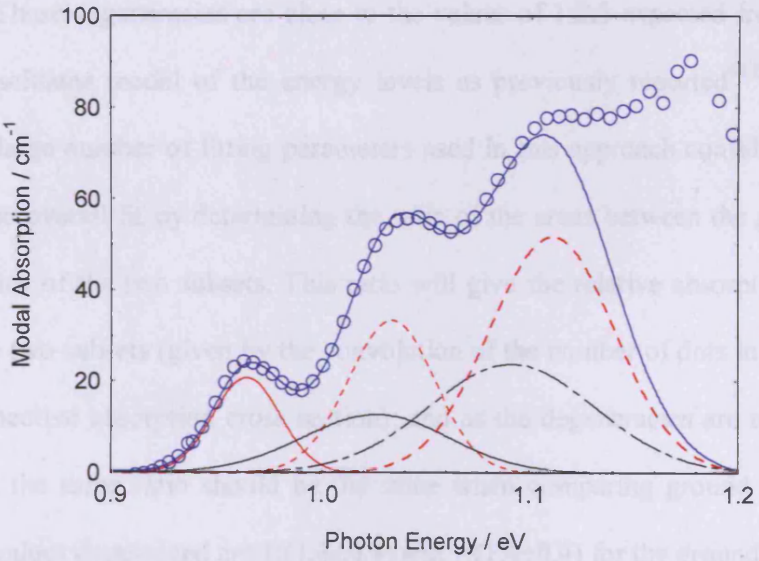

Figure 3.5: - Modal Absorption Spectrum and fitted Gaussians corresponding to a bimodal distribution of dots for the HGTSL sample.

This approach gives a good fit to the measured absorption where the parameters for the five Gaussians are summarised in Table 3.2.

	Centre Energy / eV	Broadening / meV
Large Subset of Dots		
Ground State	0.964	16
Excited State	1.033	21
2nd Excited State	1.11	24
Small Subset of Dots		
Ground State	1.025	35
Excited State	1.09	38

Table 3.2: - Fitting Parameters used for bimodal distribution fit of HGTSL absorption.

Using a bi-modal distribution gives a ground to excited state ratio of 1:(2±0.2) for both subset of dots and a ground to second excited state ratio of 1:(3.4±0.2) for the large dots. These degeneracies are close to the values of 1:2:3 expected from a simple harmonic oscillator model of the energy levels as previously reported[68,69]. Although there are a large number of fitting parameters used in this approach confidence can be gained in the overall fit by determining the ratio of the areas between the ground (and excited) states of the two subsets. This ratio will give the relative absorption strength between the two subsets (given by the convolution of the number of dots in each subset and the respective absorption cross section); and as the degeneracies are the same for each subset the same ratio should be the same when comparing ground and excited states. The values determined are 1:(1.3±0.4) and 1:(1.4±0.4) for the ground and excited states respectively. These numbers are very similar and give good confidence that the Gaussians do represent two subsets of dots. The increase in the broadening from ground to excited state(s) seems more reasonable now than in the first attempt to fit (Figure 3.2) where the broadening increased rapidly for each state. Now the width of the Gaussians

only increases slightly for the excited state(s). Figure 3.4 shows that the larger dots have a reasonable narrow energy distribution resulting in the relatively well defined ground state feature at 0.964 eV. The subsequent broadening in the higher energy features is then due to the effect of the wider distribution from the smaller set of dots.

A bimodal distribution has also been used to represent the transitions seen in the absorption from the standard sample. Due to the features being relatively undefined in the standard sample, the centre energies used in Table 3.2 have again been used. As was done previously the degeneracy of the states has been forced to be the same as observed in Figure 3.4. The fitted absorption and Gaussian parameters are in Figure 3.5 and Table 3.3 respectively.

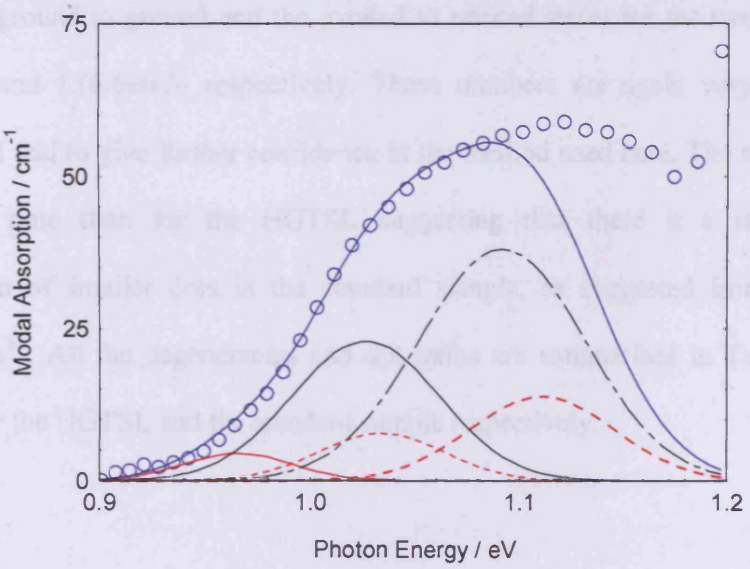

Figure 3.6: - Modal Absorption Spectrum and fitted Gaussians corresponding to a bimodal distribution of dots for the standard sample.

	Centre Energy / eV	Broadening / meV
Large Subset of Dots		
Ground State	0.964	26
Excited State	1.033	28
2nd Excited State	1.11	31
Small Subset of Dots		
Ground State	1.025	35
Excited State	1.09	38

Table 3.3: - Fitting Parameters used for bimodal distribution fit of standard absorption.

Again an excellent fit is obtained to the data using a bi-modal distribution. The ratio of the ground to ground and the excited to excited states for the two subsets are 1:(6.8±0.5) and 1:(6.6±0.5) respectively. These numbers are again very similar, as expected and add to give further confidence in the method used here. The ratio is much higher this time than for the HGTSL suggesting that there is a much higher concentration of smaller dots in the standard sample, as suggested from the AFM measurments[53]. All the degeneracies and dot ratios are summarised in Table 3.4 and Table 3.5 for the HGTSL and the standard sample respectively.

HGTSL Sample	Ratios
Large Dots	
Ground : Excited	1 : 2 ± 0.2
Ground : 3rd State	1 : 3.4 ± 0.2
Small Dots	
Ground : Excited	1 : 2 ± 0.1
Large : Small Dot Absorption (Ground State)	1 : 1.3 ± 0.4
Large : Small Dot Absorption (Excited State)	1 : 1.4 ± 0.4

Table 3.4: - Dot ratios and degeneracies for the fits used for the HGTSL sample.

Standard Sample	Ratios
Large Dots	
Ground : Excited	1 : 2 ± 0.2
Ground : 3rd State	1 : 3.4 ± 0.2
Small Dots	
Ground : Excited	1 : 2 ± 0.1
Large : Small Dot Absorption (Ground State)	1 : 6.8 ± 0.5
Large : Small Dot Absorption (Excited State)	1 : 6.5 ± 0.5

Table 3.5: - Dot ratios and degeneracies for the fits used for the standard sample.

By comparing the parameters used for the Gaussians as described in Table 3.2 and Table 3.3 several interesting conclusions can be drawn. Firstly the smaller subset of dots has the same centre energy and broadening in both samples, this implies that the smaller subset has the same distribution in both samples, and it is only the number of dots that are altered by the inclusion of HGTSLs. The broadening from the larger subset of dots is narrowed for the HGTSL sample with the ground state transition reducing by

61 %. By comparing the areas of the Gaussians in Figure 3.4 and Figure 3.5 it can also be seen the strength of the absorption from the larger subset of dots drastically increases with the inclusion of the HGTSLs.

These results go further to support the idea that by including HGTSLs the broadening can be reduced, leading to more uniform formation and improved performance. The mechanism most likely to have lead to this decrease in in-homogeneity is caused by the increased temperature of the spacer layer growth. The spacer layers are normally grown at the same temperature as the dot layers (510^0C), so not to have any adverse effect on the dots. However this temperature is substantially below the ideal temperature for GaAs. When the HGTSLs are used the increased growth temperature, will allow the Ga atoms to have an increased mobility, this allows them to re-planarise the surface, before the next well is grown. This re-planarisation, will remove any imprint of defects or dislocations from the previous layer. As well as improving the growth surface roughness, this will have two direct benefits on the device performance. Firstly the smother surface will lead to an improved homogeneity of the dots leading to a reduced linewidth as seen in the larger subset of dots. The smoother surface should also lead to fewer pits and troughs on the GaAs; this will suppress the growth of smaller dots and allow the formation of larger dots. This is supported by Table 3.4 and Table 3.5 where the ratio between the smaller and larger dots is seen to change by a factor of 5. Also as the first 15 nm of the spacers are still grown at 510^0C as was the 6 nm cap of $InGa_{0.15}As_{0.85}$, the dots should be sufficiently protected and not experience any adverse effects due to the temperature increase, supported by the fact the same centre energies can be used for the Gaussians in both samples.

One further insight this analysis yields on the samples is an increase in the dot density when HGTSLs are deployed. The ratio of the areas under the absorption curves

gives the ratio between the strength of absorption in the two samples. When this is done it is found that the area of the absorption increases by a factor of 1.6 for the HGTSL sample for both the mono-modal and bi-modal models. This strongly suggests that the number of dots has increased, supporting the evidence from the AFM and TEM studies [53,59]; this is again believed to be due to the improved growth conditions.

3.3 Modal Gain Measurements

The segmented contact technique can also be used to determine the modal gain spectra for these samples, at various values of drive current density and temperature. Modal gain spectra taken in TE polarisation at 300 K are shown for the standard sample at various drive current densities in Figure 3.6.

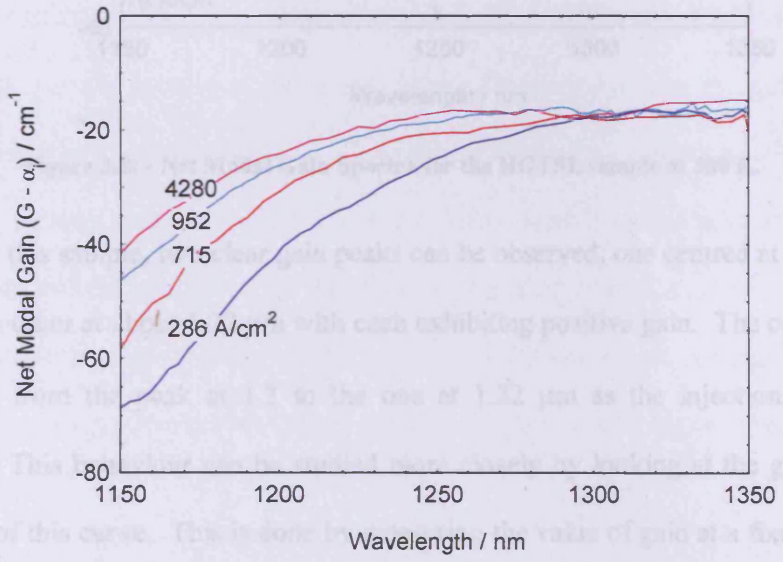

Figure 3.7: - Net Modal Gain Spectra for the standard sample at 300 K.

As expected, at long wavelengths the curves come together to give the previously measured value of α_i of 15 ± 2 cm^{-1}. The major point that is noticed about

these curves is that the gain is always negative, so even at the highest drive current densities the material will not lase. This result is consistent with the laser threshold measurements, where lasing could not be observed above 190 K. The gain spectra for the sample containing HGTSLs are shown in Figure 3.7 for increasing drive current densities at 300K under TE polarisation.

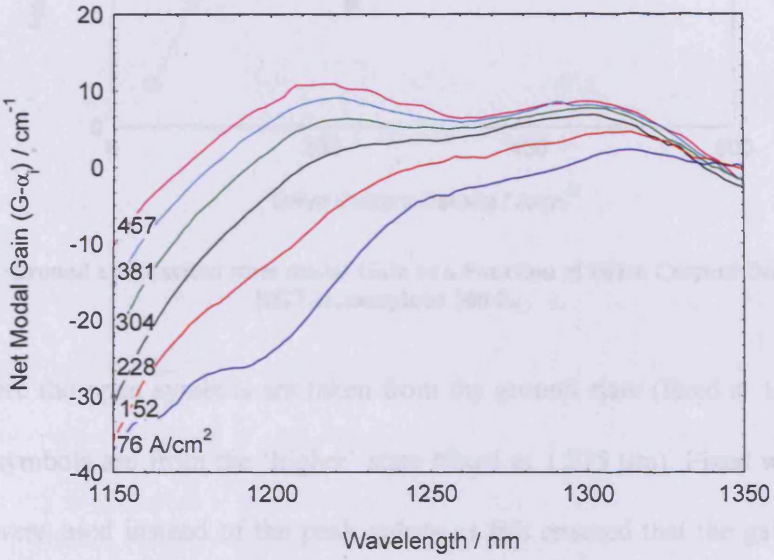

Figure 3.8: - Net Modal Gain Spectra for the HGTSL sample at 300 K.

For this sample, two clear gain peaks can be observed, one centred at around 1.3 μm and the other at about 1.22 μm with each exhibiting positive gain. The overall peak gain shifts from the peak at 1.3 to the one at 1.22 μm as the injection current is increased. This behaviour can be studied more closely by looking at the gain current behaviour of this curve. This is done by measuring the value of gain at a fixed point on each peak as a function of current.

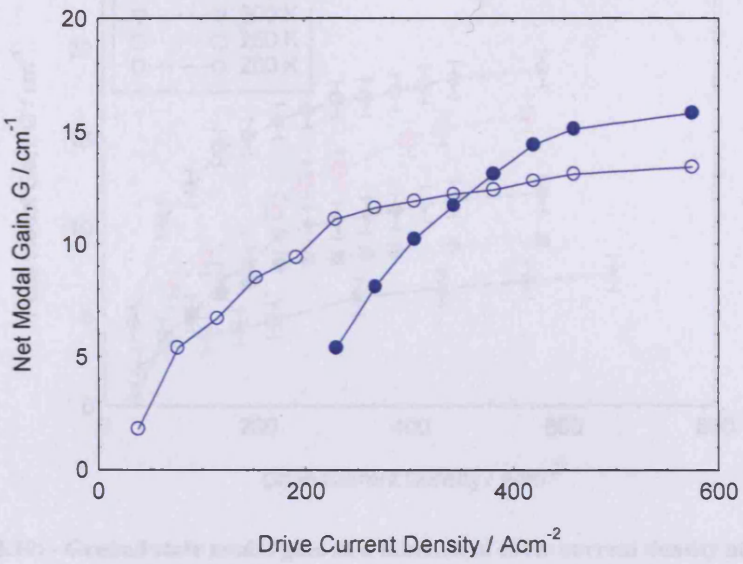

Figure 3.9: - Ground and Excited state modal Gain as a Function of Drive Current Density for the HGTSL sample at 300 K.

Where the open symbols are taken from the ground state (fixed at 1.3 μm) and the closed symbols are from the 'higher' state (fixed at 1.215 μm). Fixed wavelengths (energies) were used instead of the peak values as this ensured that the gain from the same dot states was always compared. The gain from both the ground and excited states can clearly be seen to be saturating. The ground state initially exhibits more gain, with the peak gain switching over to the 'higher' state at around 350 Acm^{-2}. The behaviour of the gain-current curves can also be observed as a function of temperature, to simplify this picture only the ground state curves are shown (although the higher state shows the same behaviour).

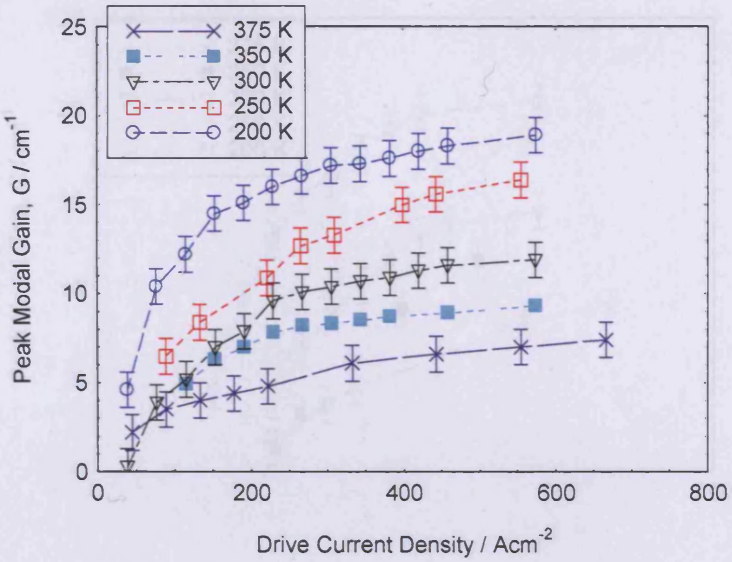

Figure 3.10: - Ground state modal gain as a function of drive current density at various temperatures for the HGTSL sample.

This shows the expected behaviour of the gain increasing with decreasing temperature, a result due to the reduced number of carriers being able to thermally escape to the wetting layer as the temperature is lowered [32]. The higher state gain also increases as the temperature is decreased (Figure 3.10), and the same behaviour is seen between the ground and 'higher' state as was observed at 300 K at all temperatures.

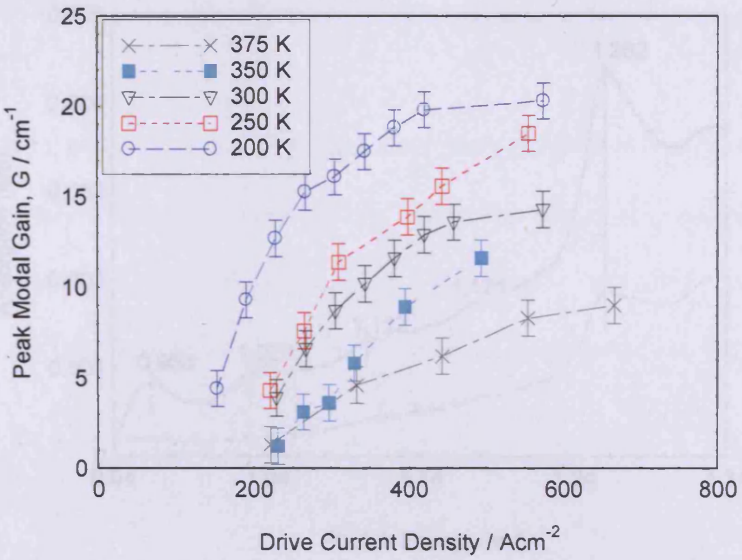

Figure 3.11: - Excited state modal gain as a function of drive current density at various temperatures for the standard sample.

3.4 Spontaneous Emission Data

The unamplified spontaneous emission has also been studied for the structure containing the HGTSLs. Unfortunately it is now not possible to study the effect of the HGTSLs, as the spontaneous emission cannot be determined in real units for the standard sample (see chapter 2). This is due to the fact that the modal gain in this device is negative, meaning that the P_f function cannot be used to calibrate the spontaneous emission because the function does not saturate at any value of energy.

Before going on to study in detail the recombination processes, a PVS spectrum (see chapter 2) was taken of the sample to identify the position of all the relevant transitions.

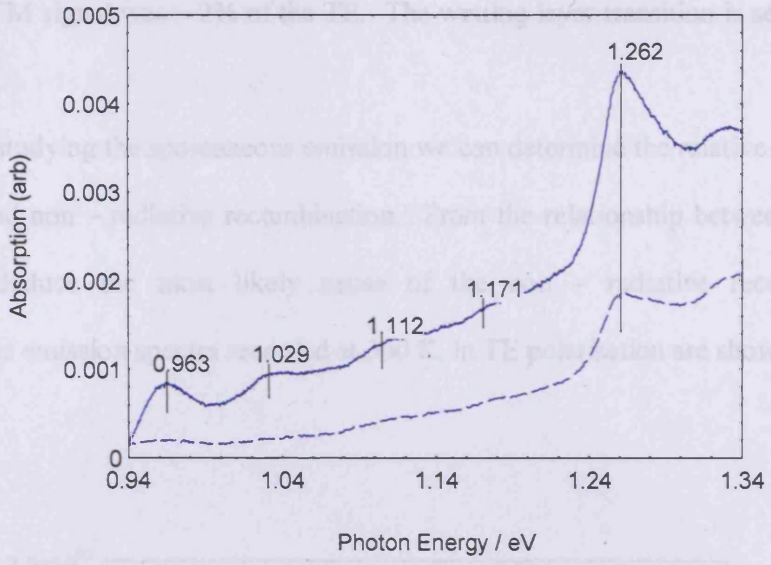

Figure 3.12: - Photo voltage Absorption Spectra of the HGTSL sample for TE polarisation (Solid Line) and TM polarisation (Dashed Line).

The first transition can clearly be seen identified at around 0.963 eV, with three higher quantum dot transitions subsequently seen (at 1.029, 1.112 and 1.171 eV respectively) and these are compared with the quantum dot transitions obtained from modal absorption measurements in Table 3.6.

	Modal Absorption Measurements / eV	**PVS Measurements / eV**
Ground State	0.964	0.963
Excited State	1.033	1.029
Third State	1.12	1.12

Table 3.6: - Comparison of peaks obtained from modal absorption and photovoltage measurements.

The signal from the quantum dot region is dominantly TE polarised, with very little signal seen in the TM spectra, agreeing with the segmented contact experiments

where the TM signal was ~ 2% of the TE. The wetting layer transition is seen at 1.262 eV.

By studying the spontaneous emission we can determine the relative amounts of radiative and non – radiative recombination. From the relationship between these we can then deduce the most likely cause of the non – radiative recombination. Spontaneous emission spectra recorded at 300 K, in TE polarisation are shown in Figure 3.12.

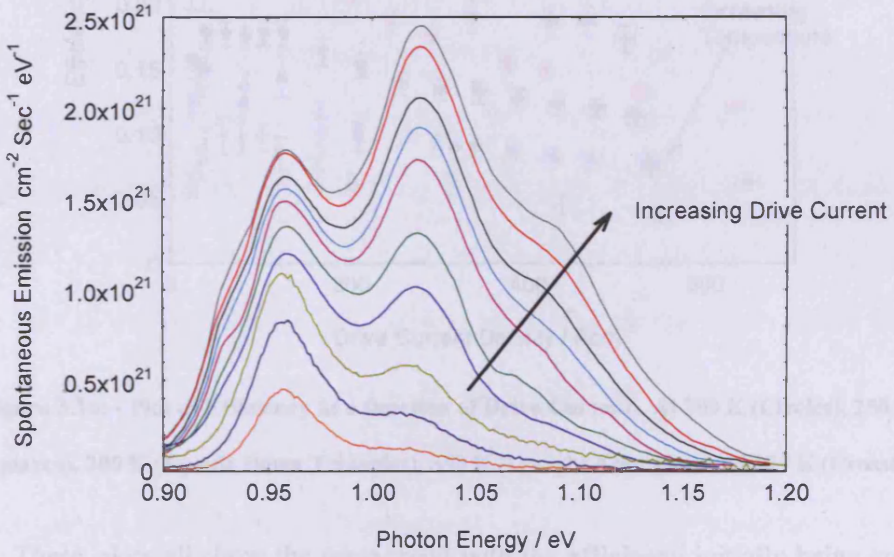

Figure 3.13: - Spontaneous Emission Spectra at 300 K and TE Polarisation for a range of drive current densities between 22 and 489 Acm^{-2}.

From this plot three transitions can be identified; the ground state transition of the large subset of dots is centred at 0.959 eV and two higher order transitions centred at 1.024 and 1.086 eV respectively. At the lowest injection level (22 Acm^{-2}); the emission is predominantly (~ 80 %) from the ground state transition, with the rest coming from the first excited state. By the highest injection level (489 Acm^{-2}) the ground state has

effectively saturated and the second peak is the dominant transition, with a large broad shoulder peak due to higher transitions.

From this data the radiative efficiency (chapter 2) has been determined for the device as a function of the drive current at various temperatures.

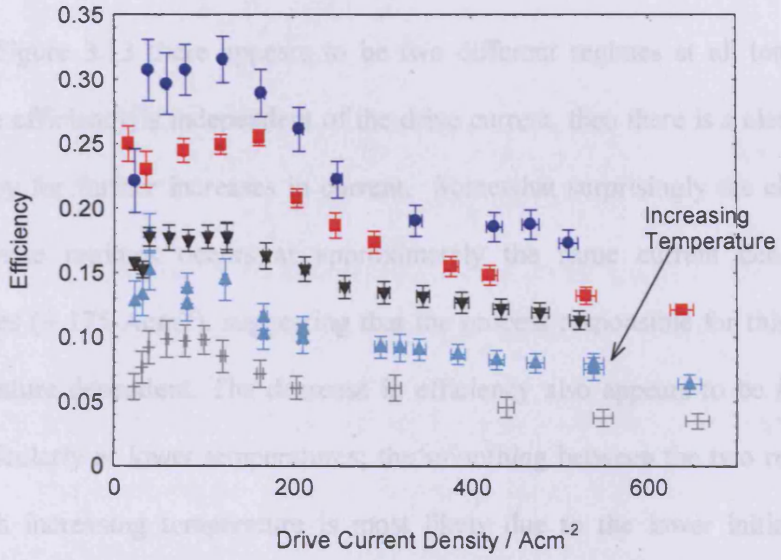

Figure 3.14: - Plot of Efficiency as a function of Drive Current. At 200 K (Circles), 250 K (Squares), 300 K (Upside Down Triangles), 350 K (Upright Triangles) and 375 K (Crosses).

These plots all show the same trend with the efficiency initially being constant with increasing current levels, then after approximately 250 Acm^{-2} there is a gradual decrease in the efficiency. The current density at which the efficiency begins to decrease seems to be independent of temperature, over the range studied here. At 300 K a maximum efficiency of around 17 % is observed, indicating that over 80 % of the current is made up of non radiative components. This result is consistent with a previous estimate of the proportion of non-radiative recombination in high quality QD lasers of approximately 90% at 300K, which was obtained with the assumption that the recombination was entirely radiative at low temperatures [27,69,70]. The present results

suggest that there is considerable room for further reduction of, an already low, threshold current density providing the origin of the non-radiative recombination can be identified and removed.

3.5 Radiative and Non – Radiative Current Densities

In Figure 3.13 there appears to be two different regimes at all temperatures, initially the efficiency is independent of the drive current, then there is a clear decrease in efficiency for further increases in current. Somewhat surprisingly the change over between these regimes occurs at approximately the same current density at all temperatures (~ 175 Acm^{-2}), suggesting that the process responsible for this change is not temperature dependent. The decrease in efficiency also appears to be sudden and sharp, particularly at lower temperatures; the smoothing between the two regimes that occurs with increasing temperature is most likely due to the lower initial value of efficiency, causing the second process to have a less dramatic effect.

To try and determine the origins of these two processes, the amount of non – radiative current as a function of the radiative current at each temperature has been calculated (plotted in Figure 3.14).

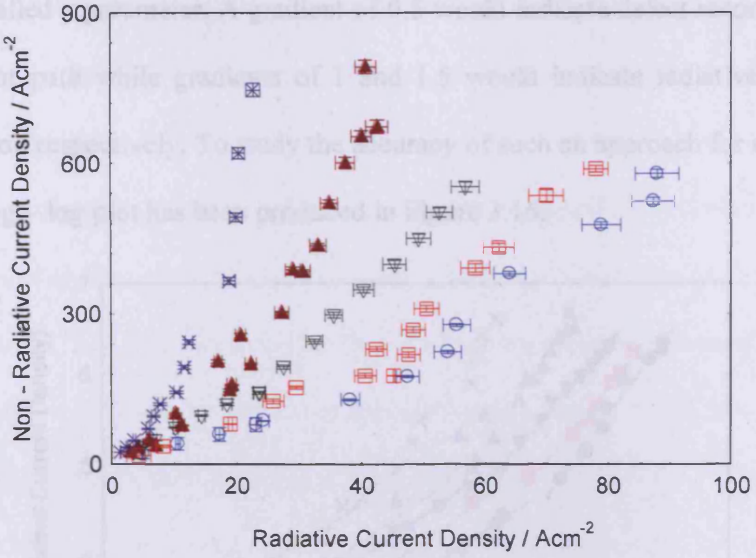

Figure 3.15: - Non – Radiative Vs Radiative Current Density. At 200 K (Circles), 250 K (Squares), 300 K (Upside Down Triangles), 350 K (Upright Triangles) and 375 K (Crosses)

Again there are two distinct regions at each temperature, as expected from Figure 3.14. The exact nature of the relationship between the radiative and non - radiative currents is important in determining the cause of the non-radiative current. The first process appears to have a linear dependence; this is as expected from Figure 3.13, as there the efficiency was static at low current levels. The second process is again much more pronounced than the first; however it still appears to have an approximately linear relationship.

In the past some groups [71-73] have used a power law analysis to try gain additional insight into the recombination processes in quantum well structures. Such an approach uses the An, Bn^2 and Cn^3 relationships to describe the monomolecular, radiative and Auger process respectively. To analyse the relative contributions a log – log plot of the radiative and non-radiative currents is produced, the x-axis in such a plot is then proportional to the log of n^2 (as the radiative current is equal to Bn^2 in a quantum well). By fitting lines to the data the dominant recombination process can be identified

via the so called z parameter. A gradient of 0.5 would indicate defect recombination as the dominant path while gradients of 1 and 1.5 would indicate radiative and Auger recombination respectively. To study the accuracy of such an approach for quantum dot systems a log – log plot has been produced in Figure 3.16.

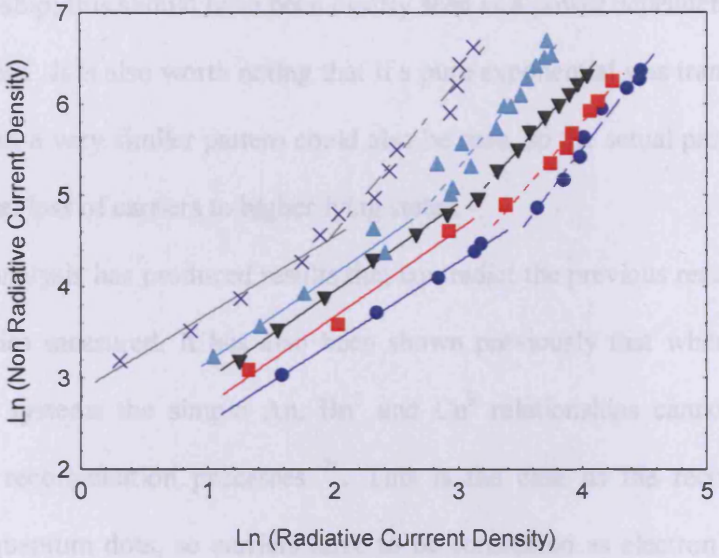

Figure 3.16: - Natural Logarithm Plot of the Non - Radiative Current Density as a Function of the Radiative Current Density. At 200 K (Circles), 250 K (Squares), 300 K (Upside Down Triangles), 350 K (Upright Triangles), 375 K (Crosses).

The region where the data is fitted with a solid line, gives the region where the first non – radiative process is dominant, while the dotted lines at each temperature represent where the second non – radiative process becomes dominant. The first process has a power relation of approximately 1 at all temperatures; this is not surprising as very linear behaviour was observed in both Figure 3.13 and Figure 3.14. A linear relationship such as this would strongly suggest that radiative recombination was dominating; however this seems unlikely given the low values of efficiency (Figure 3.13).

The second process gives a dependence in the region of 1.5 at all temperatures. Previously a dependence of 1.5 would have suggested that the second process is due to Auger recombination. This conclusion cannot be drawn so simply here, as this result seems to be in direct opposition to the previous result (Figure 3.14) which suggested a linear relationship; this should have been clearly seen as a power dependence of 1 as for the first process. It is also worth noting that if a pure exponential was transformed onto a log – log plot a very similar pattern could also be seen, so the actual process could be the exponential loss of carriers to higher lying states.

This analysis has produced results that contradict the previous results, given the low efficiencies measured. It has also been shown previously that when considering quantum dot systems the simple An, Bn^2 and Cn^3 relationships cannot be used to describe the recombination processes [74]. This is the case as the recombination is localised in quantum dots, so carriers have to be considered as electron – hole pairs. Therefore a more detailed analysis is required to determine the relative recombination processes in quantum dot systems.

Being able to determine which process is causing the loss of carriers is extremely important, as both Auger recombination [27,70]and carrier leakage to higher dot states [75] / and or the wetting layer states [69,75] have previously been reported as sources of non-radiative recombination in quantum dot systems. If the process turns out to be the exponential loss of carriers to higher lying states, where they then recombine non – radiatively, this could potentially be removed from future structures by improving the design and growth. However if the process is really due to Auger Recombination, little can be done to remove the problem, as this is an intrinsic process to the material.

An interesting point about the change over between the two processes is that it occurs for approximately the same value of drive current at all temperatures (~ 250

Acm^{-2}). Therefore looking at the individual spectra just before this change over at each temperature should give some insight into what is going on.

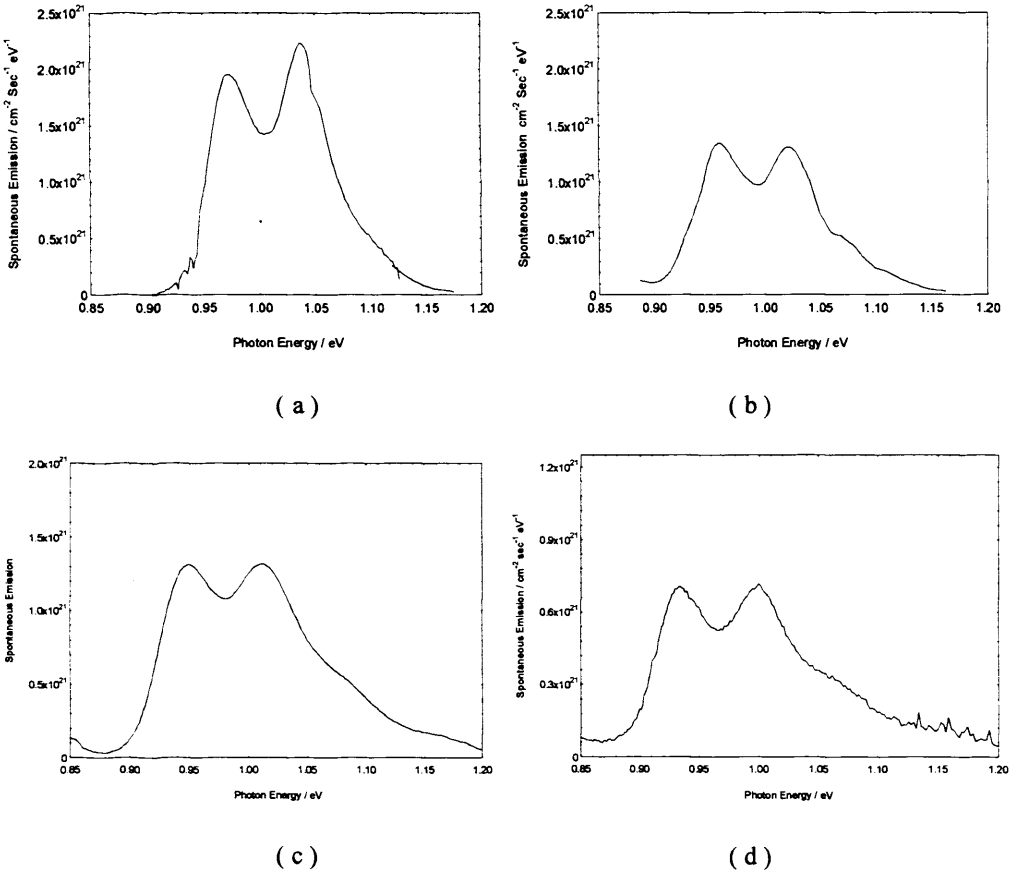

Figure 3.17: - Spontaneous Emission Spectrum for: (a) 200 K , (b) 300 K, (c) 350 K and (d) 375 K.

At all four temperatures the spectra are very similar. The change between the two non – radiative processes, seems to occur when the first and second peaks are approximately equal. Also at these currents the third peak is beginning to become noticeable. As discussed in section 1.2 there is strong evidence for a bimodal distribution of dots, therefore it is necessary to de-convolve the spontaneous emission spectra to be able to determine which transitions from which dots are involved in these spectra. To achieve this various Gaussians corresponding to the transitions in each subset of dots have been combined and fitted to the spontaneous emission spectra, in a

similar way as was done for the absorption in section 1.2. This approach assumes that the Loretenzian type line shape generated by homogenous broadening within the dots has a negligible effect on the overall shape of the spontaneous emission. This seems a reasonable assumption given previous measurements of the homogenous and inhomogeneous line widths [33-35] (giving values of 60 meV for the inhomogeneous and 8 meV for homogenous broadening at 300K).

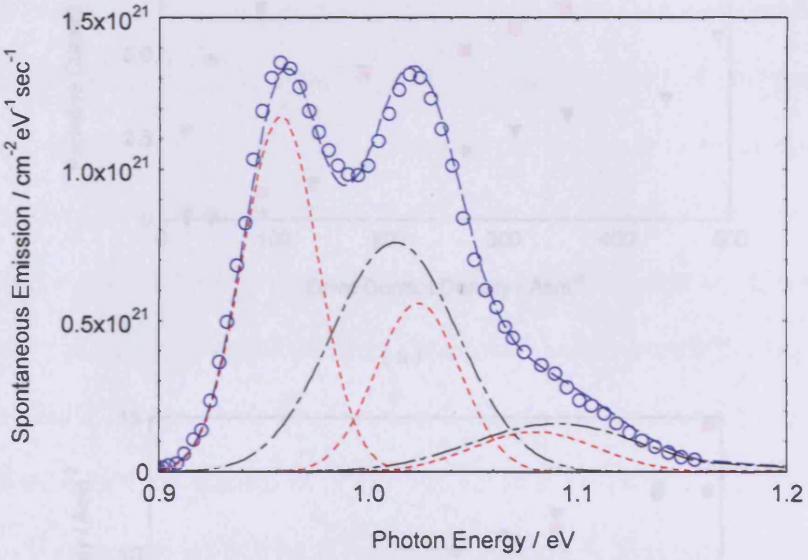

Figure 3.18: - Example spontaneous emission spectrum taken at 300 K, with Gaussian fits to represent a bimodal dot distribution.

This shows that the ground state of each dot subset has large a contribution at this current, the excited state from the larger set of dots is also reasonably populated, while there is only a small contribution from the higher energy transitions. Similar fits are obtained at the other temperatures, showing the majority of the radiative current from the two ground states for the spectra shown in Figure 3.16. From these Gaussians it is possible to determine the amount of radiative recombination from each state, therefore the light from each transition can be plotted as a function of the drive current. The presence of radiative recombination indicates electron-hole pairs within the same

dot; although this does not tell us about the non-radiative processes occurring, this method does give an indication as to the relative population of each state.

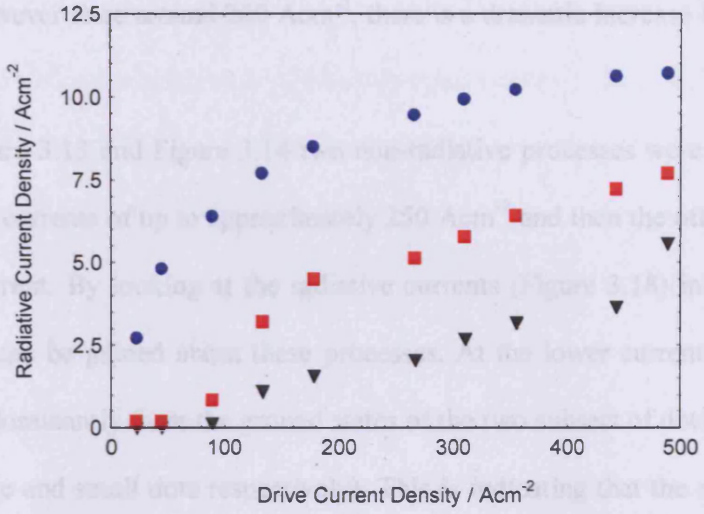

(a)

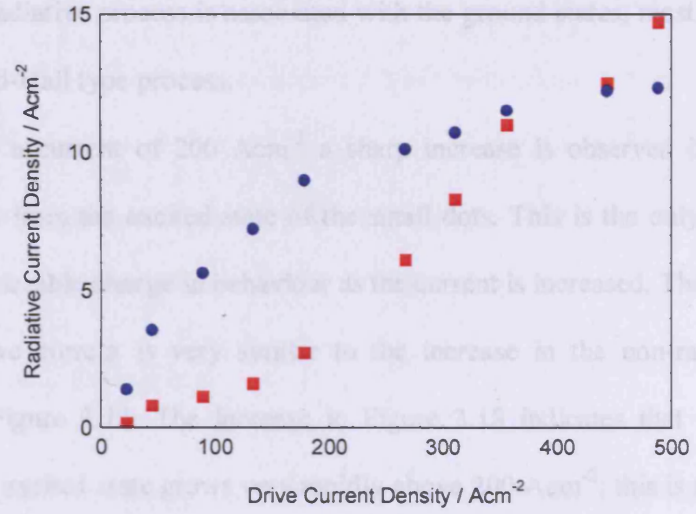

(b)

Figure 3.19: - Radiative current density as a function of drive current density for (a) the large dots, ground state (circles), excited state (squares) and second excited state (triangles) and (b) for the small dots ground state (circles) and excited state (squares).

For the large dots the radiative current from each state can be seen to slowly increase and then roll over. This is the behaviour that would be expected from the number of available states decreasing as the numbers of carriers are increased, resulting

in saturation of the radiative current. Similar behaviour can also be seen from the ground state of the smaller dots; however the excited state exhibits different behaviour. The radiative current for the excited state begins to increase slowly, as observed in the large dots, however once around 200 Acm^{-2}, there is a dramatic increase in the radiative current.

In Figure 3.13 and Figure 3.14 two non-radiative processes were observed, one dominating at currents of up to approximately 250 Acm^{-2} and then the other taking over above this current. By looking at the radiative currents (Figure 3.18) in these regimes some insight can be gained about these processes. At the lower currents the radiative current is predominantly from the ground states of the two subsets of dots (60 % and 75 % for the large and small dots respectively). This is indicating that the majority of the carriers are in the ground states of the dots. Therefore it seems reasonable to assume that the first non-radiative process is associated with the ground states, most likely due to a Shockley-Read-Hall type process.

Above a current of 200 Acm^{-2} a sharp increase is observed in the radiative recombination from the excited state of the small dots. This is the only transition that shows any noticeable change in behaviour as the current is increased. The steep increase in the radiative current is very similar to the increase in the non-radiative current observed in Figure 3.14. The increase in Figure 3.18 indicates that the number of carriers in the excited state grows very rapidly above 200 Acm^{-2}; this is most likely due to the thermal activation of the carriers from the ground to the excited state as the carrier density is increased. This results in a higher proportion of carriers in these states as the injection is increased, although the ground state emission also continues to increase due to the carriers being in a thermal distribution. Similar behaviour is also observed at all the temperatures studied, where a sudden increase in the radiative current from the

excited state is observed above current densities of around 200 Acm^{-2}. The large increase in the number of carriers present in the excited state of the smaller dots above this current, strongly suggests that the second non-radiative process occurs in this state.

Therefore it seems likely that both non-radiative processes are due to Shockley-Read-Hall recombination processes. The first process occurs in the ground state of one or both of the subset of dots, the second process is then caused by the thermal activation of carriers into the excited state of the smaller dots and there subsequent recombination there.

Although this analysis has shown Shockley-Read-Hall processes to be the most likely cause of the non-radiative recombination, these arguments have been based on the behaviour of the radiative recombination. The actual carrier concentrations may actually behave in a different way to the radiative recombination, meaning that the possibility of Auger recombination cannot be ruled out. The wetting layer could also be responsible for the non-radiative recombination; Figure 2.8 in chapter 2 showed approximately 1 % of the radiative current was from the wetting layer. This is therefore showing that the wetting layer has a large number of carriers present; therefore it is also possible that the non-radiative recombination also occurs in the wetting layer.

3.6 Additional Samples

The work presented so far in this chapter has illustrated the composition of the spacer layer can have a pronounced effect on the optical properties of quantum dot structures. It has been shown that by growing the spacer layer in two temperature steps, greatly enhanced performance can be achieved. However it needs to be considered whether the optimum design has been achieved for the spacer layers. The modal gain is determined by the overlap of the optical mode and the active region. As such if the

layers can be stacked closer together there will be a greater overlap between the mode and the active layers and hence a higher gain. Previous studies have shown good performance from stacked quantum dot layers using thin spacer layers of only 20 or 30 nm thick spacer layers [27,76,77]. Therefore it may be possible to further reduce the spacer layers studied in this work, however a reduction in the thickness may lead to an inadequate smoothing of the surface and result in an increased inhomogeneous broadening and a higher defect density as observed for the standard sample. A possible solution to this problem would be to increase the growth temperature of the high temperature GaAs step.

To look at possible improvements in the modal gain and efficiency by modifying GaAs spacer layers three further samples were grown and investigated. All three samples consisted of 5 DWELL layers of the same composition as previously. The first of these is essentially a repeat of the HGTSL structure studied above, however now the high temperature step is grown at 585 ^{0}C and the active region is incorporated into an $Al_{0.45}Ga_{0.55}As$ waveguide structure. A sample with a reduced spacer layer was also grown, this sample had an initial 15 nm GaAs cap grown at 510 ^{0}C, before 20 nm was deposited at 585 ^{0}C, hence reducing the overall thickness to 35 nm. A third sample was also grown in which the overall spacer layer thickness was kept at 35 nm, but the high temperature 20 nm step was grown at 620 ^{0}C. This information is summarised in Table 3.7.

Sample	GaAs Spacer Layer Temperatures		Total GaAs Spacer Layer Thickness / nm
	Initial Cap	High Growth Temperature Step	
Repeat HGTSL	15 nm (510^{0}C)	35 nm (585^{0}C)	50 nm
Thin HGTSL	15 nm (510^{0}C)	20 nm (585^{0}C)	35 nm
Hot HGTSL	15 nm (510^{0}C)	20 nm (620^{0}C)	35 nm

Table 3.7: - Spacer layer growth parameters

The initial cap was kept constant to protect the previous dot layer from any thermal annealing effects, while the high growth temperature step was altered. TEM studies on the three wafers performed by Dr San Lin Liew at Sheffield University revealed the dot densities to be the same in each sample within the limit of the technique. Along with a defect density of below 10^6 cm^{-2} for each wafer again set by the resolution of the system.

Therefore none of the structures exhibit the gross problems encountered by the standard sample studied previously[52,53]. The segmented contact method was again used to study the modal absorption, gain and un-amplified spontaneous emission from the three structures. The modal loss spectra for the three structures can be seen in Figure 3.19.

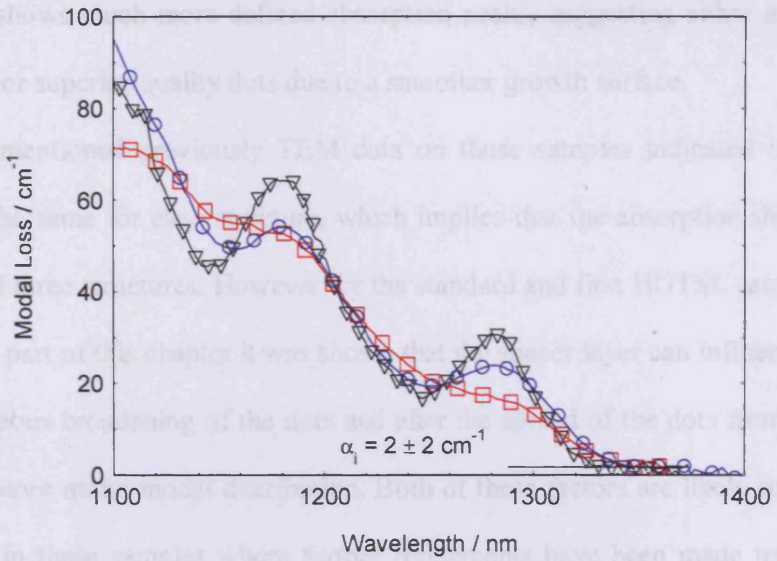

Figure 3.20: - Modal loss spectra at 300 K for the repeat (circles), thin (squares) and hot (triangles) HGTSL samples.

All three samples have the same value for the internal loss of 2 ± 2 cm^{-1}, indicating that no gross defects or dislocations occur in any of the samples which are in agreement with the TEM data. Two clear absorption peaks can be seen in each sample with approximately the same centre wavelength (energy), which indicates that the initial 15 nm cap is sufficient to inhibit any post growth annealing of the dots (resulting in a blue shift in the dot emission) even at the highest temperature of 620 ^{0}C. The repeat sample has a slightly reduced absorption height, when compared to the original HGTSL structure (Figure 3.1), with peak ground state absorptions of 29 cm^{-1} and 22 cm^{-1} respectively; (this is indicating) that there is a reduced dot density in this second growth set. The thin sample (square points) shows less well defined features than the repeat structure (circles), which suggests that the thinner high growth temperature region is not thick enough to allow sufficient smoothing of the GaAs surface. This will lead to an increased inhomogeneous broadening as was witnessed for the standard sample before. The sample with an increased temperature for the second stage of the GaAs cap

(triangles) shows much more defined absorption peaks, suggesting either an increased dot density or superior quality dots due to a smoother growth surface.

As mentioned previously TEM data on these samples indicated that the dot density is the same for each structure, which implies that the absorption should be the same for all three structures. However for the standard and first HGTSL sample studied in the main part of this chapter it was shown that the spacer layer can influence both the inhomogeneous broadening of the dots and alter the spread of the dots from a bimodal towards a more mono modal distribution. Both of these factors are likely to have been influenced in these samples where further refinements have been made to the spacer layer. A shift in the bi modal distribution between the samples could result in different absorption spectra being obtained for the samples. To study these effects Gaussian functions representing the ground and excited state(s) transitions from the two dot sizes have been fitted to the three absorption curves. The Gaussians have been fitted using the same degeneracies as before (a ratio of 1 : 2 : 3, for the ground to excited states), the centre energies and sigma values used for each structure are summarised in Table 3.8, while the ratio of large to small dots is summarised in Table 3.9.

		Centre Energy / eV	Broadening / meV
Repeat HGTSL Sample	**Large Subset of Dots**		
	Ground State	0.963	16
	Excited State	1.048	20
	2nd Excited State	1.12	25
	Small Subset of Dots		
	Ground State	1.021	35
	Excited State	1.115	38
Thin HGTSL Sample	**Large Subset of Dots**		
	Ground State	0.967	20
	Excited State	1.051	25
	2nd Excited State	1.135	28
	Small Subset of Dots		
	Ground State	1.029	32
	Excited State	1.11	35
Hot HGTSL Sample	**Large Subset of Dots**		
	Ground State	0.967	13
	Excited State	1.051	17
	2nd Excited State	1.135	21
	Small Subset of Dots		
	Ground State	1.029	30
	Excited State	1.11	32

Table 3.8: - Gaussian fitting parameters used.

	Ratio of Large to Small Dots
Repeat HGTSL Sample	1 : 2.5 ± 0.5
Thin HGTSL Sample	1 : 3.0 ± 0.5
Hot HGTSL Sample	1 : 1.9 ± 0.5

Table 3.9: - Ratio of large to small dots.

The centre energies and broadenings used for the three samples are approximately the same, with slighter broader Gaussians required for the thin sample and slightly narrower ones for the hot structure. This is consistent with the conclusions drawn from the absorption curves (Figure 3.19) concerning the smoothing of the GaAs surface prior to the dot deposition. The values for the repeat structure also agree reasonably well with those used to fit the original HGTSL structure (Table 3.2). The information in Table 3.9 shows that the major difference between the structures is in the changing ratio of large to small dots, suggesting an alteration in the concentration of small and large dots. Decreasing the thickness of the spacer layer can be seen to lead to an increase in the number of smaller dots, a subsequent increase in the growth temperature of this layer, results in a decrease in the number of smaller dots leading to a more mono-modal distribution. The increase in the percentage of larger dots results an increased number of long wavelength states as observed in the absorption spectrum of Figure 3.19. The relative number of small to large dots for the repeat structure has almost doubled compared to the original HGTSL sample, suggesting an inferior growth in this sample set compared to the initial growth run.

The absorption data has shown that by decreasing the thickness of the high temperature step, the GaAs surface is inadequately smoothed, resulting in an increased inhomoginaity of the dots as well as a higher percentage of small dots forming when compared to the control structure. By then increasing the growth temperature of this

thinner layer to 620 ^{0}C, sufficient smoothing of the surface occurs, due to the greater mobility of the Ga atoms. This results in less inhomogeneous broadening and a higher relative number of large dots compared to both the thin and the control sample.

The change in the broadening experienced by the dots along with the alteration in size distribution should result in drastically different performance for the three structures. The increase in the number of large dots for the hot HGTSL sample, will obviously result in a larger number of long wavelength energy states. This should allow higher ground state modal gains to be achieved for this structure. To investigate this; measurements were made of the modal gain for the three structures; the peak value of the modal gain is plotted as a function of the current density in Figure 3.20, where the solid lines provide a guide to the eye as to where the peak gain is from the ground state.

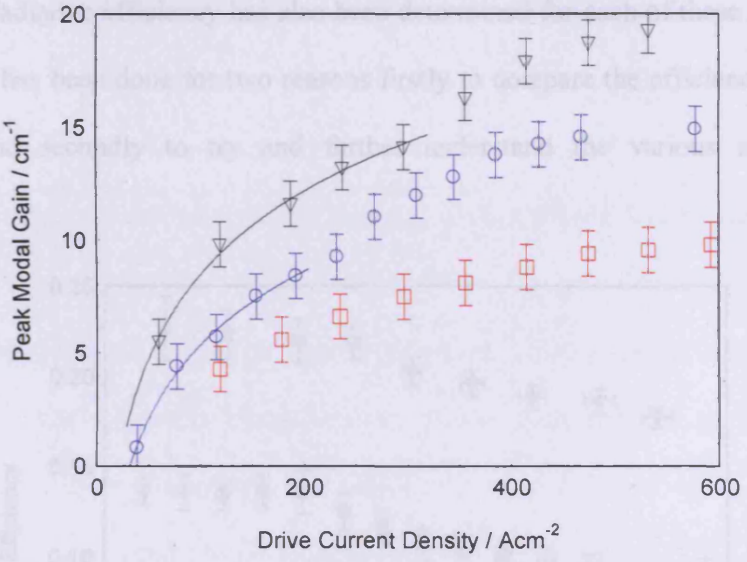

Figure 3.21: - Peak modal gain as a function of current density for the repeat (circles), thin (squares) and hot (triangles) HGTSL samples at 300 K.

The repeat structure shows a similar performance to the original HGTSL sample (Figure 3.9 and Figure 3.10). Reducing the spacer layer thickness lowers the modal gain that can be achieved, it should also be noted that the peak gain is always from the excited state in this device. The maximum peak gain that can be achieved from this

structure (over the current range studied) is approximately half the value from the repeat structure, however the excited state absorption for these two structures (Figure 3.19) is approximately the same, indicating an increase in the non-radiative currents in this structure. By then increasing the growth temperature of the spacer layer the gain greatly increases to a value higher than the control sample. More gain can be obtained from the ground state for this structure so it can be operated on the ground state up to higher currents. This is consistent with the absorption data, which showed a decreased broadening and a higher percentage of large dots, resulting in more states available to contribute to the gain at 1.3 μm. This results in a maximum modal gain from the ground state of approximately 14 cm^{-1}, which would be sufficient to allow ground state lasing in a 1 mm long cavity with as cleaved facets.

The radiative efficiency has also been determined for each of these structures at 300 K. This has been done for two reasons firstly to compare the efficiencies for each structure, and secondly to try and further understand the various non-radiative processes.

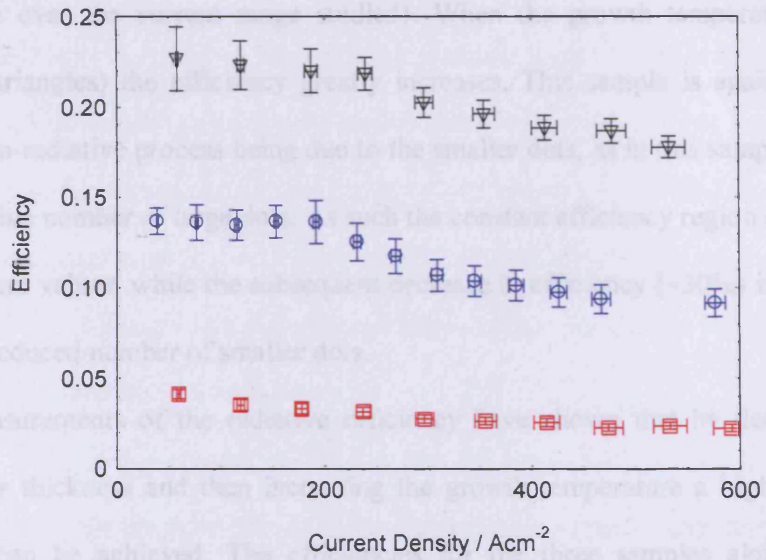

Figure 3.22: - Radiative efficiency as a function of current density for the repeat (circles), thin (squares) and hot (triangles) HGTSL samples at 300 K.

The repeat structure shows a similar performance to the original HGTSL sample studied previously. This shows an initial flat region giving an efficiency of approximately 14 %, before a decrease at higher currents. This decrease was previously shown to be most likely due to the escape of carriers to the excited state of the smaller dots and there subsequent non-radiative recombination there. Over the current range studied this second process leads to an approximately 50 % reduction in the radiative efficiency. The thin sample (squares) shows a drastic reduction in radiative efficiency to a maximum of around 4 %, is consistent with the absorption measurements (Figure 3.19) which showed an increased broadening and poorer quality growth in this sample. The absorption data also indicated a change in the bi-modal dot distribution for this sample, leading to an increase in the relative number of small dots. It has also been shown that the most likely cause of the second non-radiative process is the non-radiative recombination of carriers in the excited state of the smaller dots. The data here (Figure 3.21) is consistent with this idea, as a greater number of small dots will lead to a lower radiative efficiency as well as a sharper decrease in the efficiency (approximately a 110 % decrease over the current range studied). When the growth temperature is then increased (triangles) the efficiency greatly increases. This sample is again consistent with the non-radiative process being due to the smaller dots, as in this sample there is a higher relative number of large dots. As such the constant efficiency region occurs up to higher current values, while the subsequent decrease in efficiency (~30%) is less severe due to the reduced number of smaller dots.

Measurements of the radiative efficiency have shown that by decreasing the spacer layer thickness and then increasing the growth temperature a higher radiative efficiency can be achieved. The efficiencies for the three samples along with the

absorption data has helped support the idea that the second non-radiative process observed is due to the non-radiative recombination of carriers in the smaller dots.

It should be noted that these last three samples were grown as part of a much later growth run than the initial two structures studied in this chapter. As such the samples studied in the following chapters are based upon the original HGTSL sample, consisting of 50 nm wide spacer layers, with an initial 15 nm cap grown at 510 ^{0}C, followed by a 35 nm step grown at a temperature of 580 ^{0}C.

3.7 Conclusions

It has been shown that by using High Growth Temperature Spacer Layers, the level of defects can be reduced, as well as an increase in the number of quantum dots formed. It has also been illustrated that the amount of inhomogeneous broadening is reduced and the dot distribution is altered towards a more mono modal distribution through the use of this technique. These improvements lead to a dramatic increase in the level of modal gain that the material exhibits, hence leading to improved laser performance. However even in high quality material such as this, over 80 % of the current is used up in non radiative processes at room temperature. It has been illustrated that this non radiative recombination is due to two processes, the first is attributed to Shockley-Reed-Hall type recombination associated with the ground state. The second process has been shown to be a leakage problem to higher lying states where the carriers subsequently recombine non-radiatively.

The work in this chapter has shown that the most likely leakage path is due to the activation of carriers from the ground to excited state in the smaller dot distribution. This should mean that the performance of quantum dot lasers can be greatly enhanced, as the first non radiative process should be able to be reduced with superior quality

material. While the second process can theoretically be removed, by eliminating the smaller subset of dots; resulting in a mono modal distribution. Further refinements of the spacer layer growth has shown that a greater percentage of larger dots can be formed, leading to increased modal gain and radiative efficiencies.

4. Multi-Layer Samples

4.1 Introduction

As discussed previously (chapter 3) quantum dot structures experience low values of modal gain. As such quantum dot layers are often stacked[52,59,78,79], to increase the number of dots and hence the available gain. As also described in chapter 3 the use of multiple quantum dot layers can lead to an increased defect formation in the active layers[52,80-83]. As described the use of High Growth Temperature Spacer Layers (HGTSLs)[52,53] has led to the realisation of greatly improved growth of multi layer quantum dot samples, resulting in ultra-low threshold currents[52,53].

AFM and TEM studies suggested that there were no obvious changes in dot or defect density between the first and the fifth layers when HGTSLs were used[53]. However as only 5 layer samples were studied in chapter 3, it is possible that there are still small differences between the layers when stacked that cannot be resolved by AFM or TEM techniques. It is also feasible that more layers could be stacked without any significant degradation in the overall performance allowing higher modal gains to be achieved.

To perform a systematic study on the effects of using multi stacked quantum dot layers a series of samples were investigated using the segmented contact method. These structures all consisted of DWELL layers formed by depositing 3.0 mono layers of InAs onto 2 nm of $In_{0.15}Ga_{0.85}As$ and then being capped by a further 6 nm of $In_{0.15}Ga_{0.85}As$ these were then separated by 50 nm HGTSLs[52]. A total of four structures were investigated containing 3, 5 (a repeat of the structure studied in chapter 3), 7 and 10 DWELL layers.

4.2 Modal Absorption Data

The segmented contact method was used to obtain modal loss spectra for each structure (Figure 4.1). The reason for comparing these spectra is to see if the increased number of layers results in any increased scattering loss (signified by a change in α_i) or any change in the dot density or distribution (signified by variations in the absorption peaks). Due to the different number of DWELL layers in each sample, the overlap between the optical field and the active region will be different for each sample, with the ten layer sample having the smallest overlap. This difference in overlap will influence the measurements of the absorption, gain and spontaneous emission. To take account of this the effective mode width, ω_{mod} has been determined for each structure over all wavelengths, the results are then normalised to that of the three layer sample.

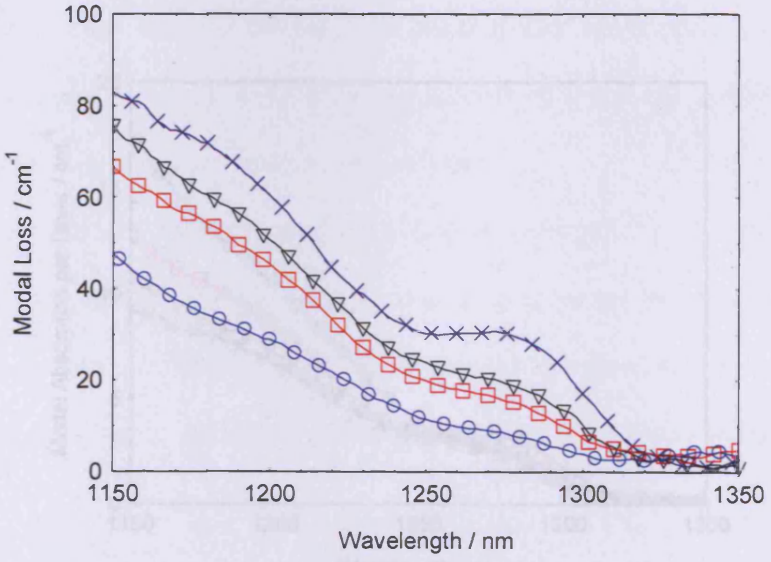

Figure 4.1: - Modal loss spectra for the 3 layer (circles), 5 layer (squares), 7 layer (triangles) and 10 layer (crosses) devices.

The value of values of α_i obtained for the four structures are the same within the experimental uncertainty at 3 ± 2 cm^{-1}. This indicates that there are no large defects or

dislocations forming in the higher layers as these would lead to an increased scattering loss. Two absorption peaks are seen for each of the devices centred at approximately 1276 and 1190 nm. As discussed previously (chapter 3) quantum dot structures grown via this technique seem to have a bi-modal dot distribution. The longer wavelength peak is attributed to the ground state transition in the larger subset of dots, while the second peak is due to the convolution of the first excited state in the larger dots and the ground state transition in the smaller dots. As the number of layers is increased the modal loss increases at a fixed wavelength, which is consistent with the increased number of states expected due to the additional layers. If the dot density and uniformity is the same in each layer grown, then the increasing loss should be proportional to the increase in the number of layers. To see if this is the case the value of α_i has been removed from each curve to obtain the modal absorption, this has then been plotted as the absorption per layer (Figure 4.2).

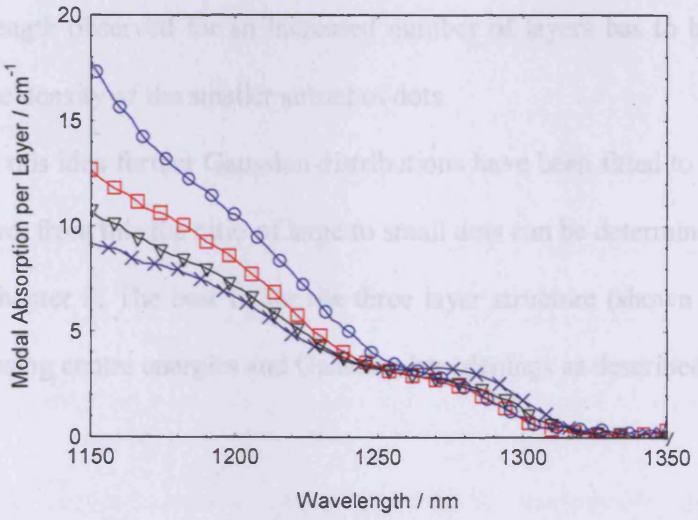

Figure 4.2: - Modal absorption divided by number of DWELL layers for the 3 layer (circles), 5 layer (squares) and 7 layer (triangles) and 10 layer (crosses) devices.

The long wavelength absorption peak (due to the ground state of the larger dots) has approximately the same magnitude and shape for each of the structures. This is

showing that the layers can be stacked without any significant alterations to dot density or distribution. However the absorption at shorter wavelengths appears to contradict this first result. The three layer device exhibits the most absorption per layer at shorter wavelengths the magnitude of the absorption per layer then decreases with increasing layer number. This seems to be suggesting that a lower dot density is achieved for each additional layer added. The two absorption peaks observed in Figure 4.2 appear to be giving different results as to the effect on dot density due to stacking quantum dot layers.

The explanation for this behaviour would appear to be due to a change from a bi modal towards a more mono modal dot distribution as the number of layers is increased. As the longer wavelength absorption peak does not significantly change with the number of layers, it seems reasonable to assume that the density of large dots is approximately the same in each layer. Therefore the absorption from the excited state of the larger dots must also be the same for each structure. As such the decreasing absorption strength observed for an increased number of layers has to be caused by a reduction in the density of the smaller subset of dots.

To test this idea further Gaussian distributions have been fitted to the absorption from each curve, from this the ratio of large to small dots can be determined for each, as described in chapter 3. The best fit for the three layer structure (shown in Figure 4.3) was obtained using centre energies and Gaussian broadenings as described in Table 4.1.

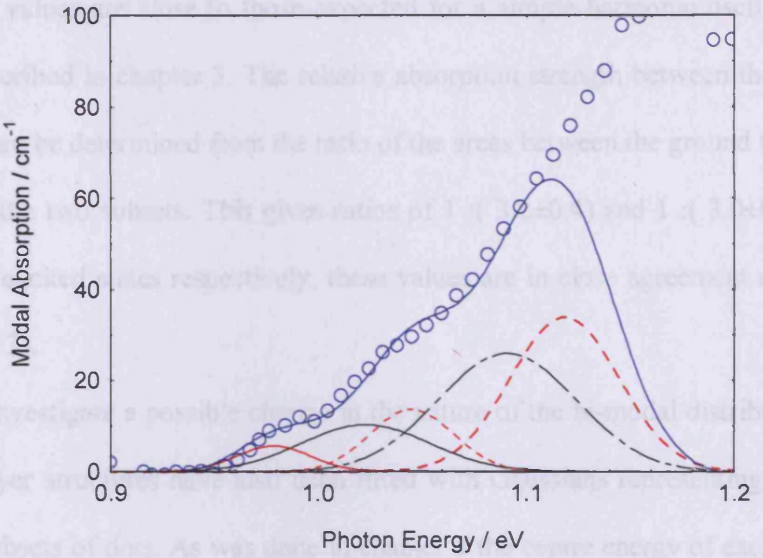

Figure 4.3: - Modal absorption spectra with Gaussian fits for the 3 layer sample.

	Centre Energy / eV	Gaussian Broadening / meV
Large Subset of Dots		
Ground State	0.978	18
Excited State	1.045	20
2nd Excited State	1.118	24
Small Subset of Dots		
Ground State	1.022	31
Excited State	1.09	34

Table 4.1: - Fitting parameters used for Gaussians representing the 3 layer structure.

Figure 4.3 shows an excellent agreement between the experimental data and the Gaussian fits. For the large subset of dots the ratio of the areas of the ground to excited and second excited state are 1 :(2.2±0.3) and 1 :(3.9±0.4) respectively, while for the smaller subset of dots a ratio of 1 :(2.1±0.3) is obtained for the ground to excited state

area. These values are close to those expected for a simple harmonic oscillator[68,69] of 1:2:3 as described in chapter 3. The relative absorption strength between the large and small dots can be determined from the ratio of the areas between the ground (or excited) states from the two subsets. This gives ratios of 1 :(3.2±0.4) and 1 :(3.0±0.4) for the ground and excited states respectively, these values are in close agreement as expected (see chapter 3).

To investigate a possible change in the nature of the bi-modal distribution the 5, 7 and 10 layer structures have also been fitted with Gaussians representing transitions from two subsets of dots. As was done in chapter 3 the centre energy of each transition is kept the same as those used in Table 4.1 for each device. The broadenings and heights were then used as fitting parameters. The degeneracies for the ground to excited state(s) were forced to stay in the ratio 1:2:3 for both subsets of dots, as was done previously (see chapter 3). The ratio of the absorption between the large abd small dots was allowed to change between samples; however the ratio had to be the same for both ground and excited state. The best fits obtained for each sample are shown in Figures 4.4 to 4.6.

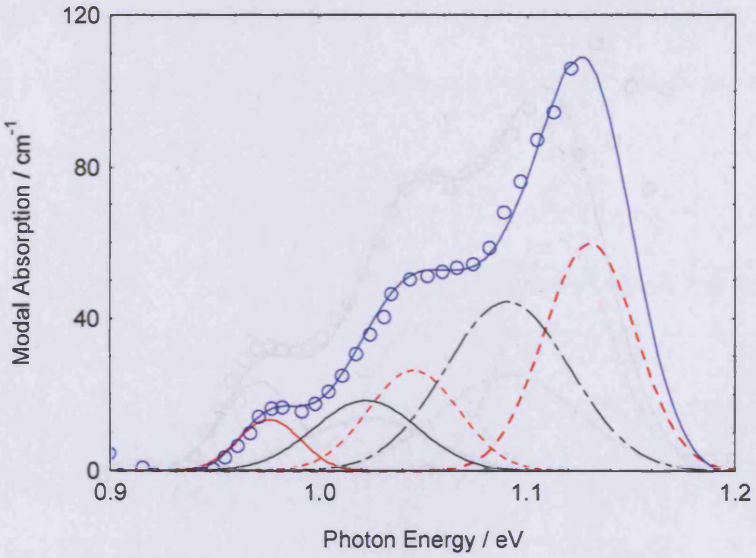

Figure 4.4: - Modal absorption spectra with Gaussian fits for the 5 layer sample.

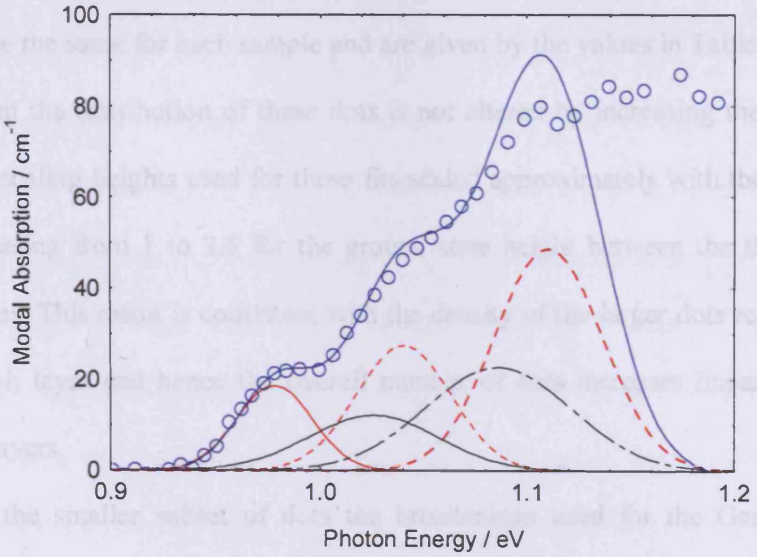

Figure 4.5: - Modal absorption spectra with Gaussian fits for the 7 layer sample.

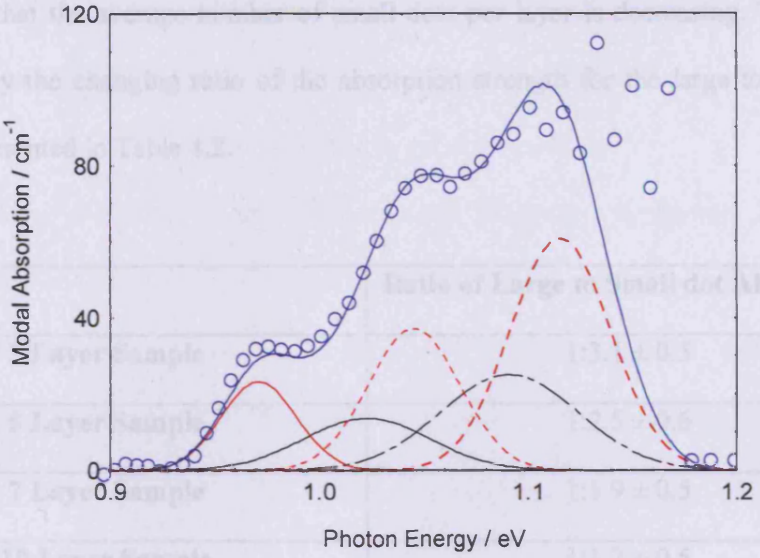

Figure 4.6: - Modal absorption spectra with Gaussian fits for the 10 layer sample.

For the large subset of dots the broadening values used for each Gaussian transition are the same for each sample and are given by the values in Table 4.1. This is implying that the distribution of these dots is not altered by increasing the number of layers. The scaling heights used for these fits scaled approximately with the number of layers increasing from 1 to 3.5 for the ground state height between the three and 10 layer samples. This result is consistent with the density of the larger dots remaining the same in each layer and hence the overall number of dots increases linearly with the number of layers.

For the smaller subset of dots the broadenings used for the Gaussians also remain constant and are given by the values in Table 4.1. This again suggests that an increase in the number of layers does not have an effect on the size or composition distribution of the dots. However the scaling heights used for these fits only increases slightly with an increasing layer number changing from a value of 3 for the ground state of the three layer sample to a value of 4.5 for the ground state of the ten layer device. As the width of the Gaussians remains constant as the number of layers increases this is

suggesting that the average number of small dots per layer is decreasing. This idea is supported by the changing ratio of the absorption strength for the large to small dots which is presented in Table 4.2.

	Ratio of Large to Small dot Absorption
3 Layer Sample	1:3.1 ± 0.5
5 Layer Sample	1:2.5 ± 0.6
7 Layer Sample	1:1.9 ± 0.5
10 Layer Sample	1:1.2 ± 0.5

Table 4.2: - Ratio of the number of large to small dots.

From this data it is clear that the number of large dots increases relative to the number of smaller dots. As the number of layers is increased from three to ten layers; the dot distribution changes, with the number of small dots decreasing, resulting in a larger percentage of larger dots in the ensemble. As the number of large dots is approximately the same in each layer yet this ratio is decreasing it would appear that fewer small dots are formed in the higher layers. The same amount of material is deposited in each layer (3.0 mono layers) to form the wetting layer and dots, however fewer dots are formed in the higher layers. There are two possible processes that could account for this additional material; it may be that thicker wetting layers are formed in the higher layers using this material. However it would be expected that smaller dots form first, some of which would then go on to form larger dots. Therefore it would seem reasonable to expect a lower density of larger dots to form, which is in contrast to the data presented in Figures 4.4 to 4.6. Another possible explanation to account for this

excess material is an increased number of non coherent islands forming defect sites instead of quantum dots. Again it is difficult to understand why this would prevent the formation of smaller dots while leaving the larger dots unchanged.

Although the origin of this change in dot distribution is unclear, it may have potential benefits on the performance at 1.3μm. This is the case as a higher percentage of the total states are at 1.3 μm as the number of layers is increased. To look at this effect the modal gain, along with the radiative and non-radiative currents have been determined.

4.3 Modal Gain

The TE polarised modal gain was measured for each sample at 300 K using the segmented contact method, example spectra are shown in Figure 4.7 for the 10 layer sample.

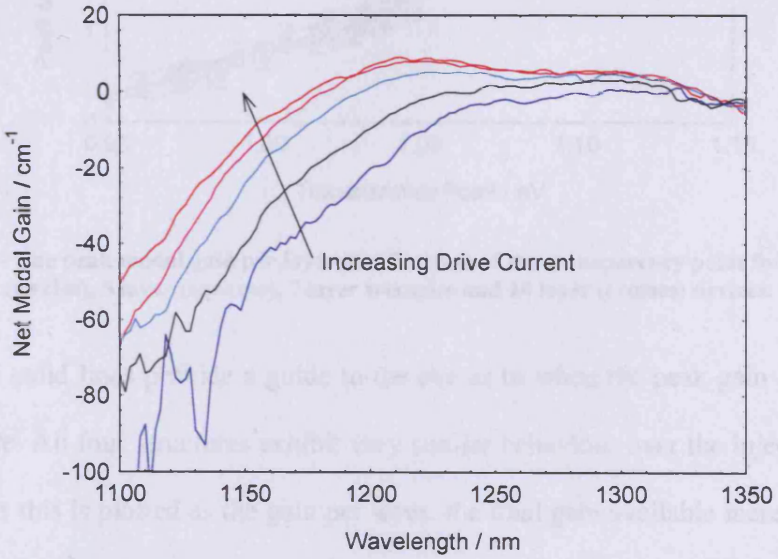

Figure 4.7: - Example modal gain spectra recorded at various drive current densities for the 10 layer sample.

As expected from previous samples and the absorption spectra in Figure 4.1 two gain peaks can clearly be resolved. At low injection the gain is predominantly from the long wavelength peak and as the current is increased the peak gain switches to the shorter wavelength. From the gain curves it is possible to determine the peak modal gain as a function of the transparency point as described previously (chapter 2) for each device. Obviously each sample will exhibit different levels of gain due to the different number of layers, therefore to make comparison easier the data has been plotted as the peak modal gain per layer.

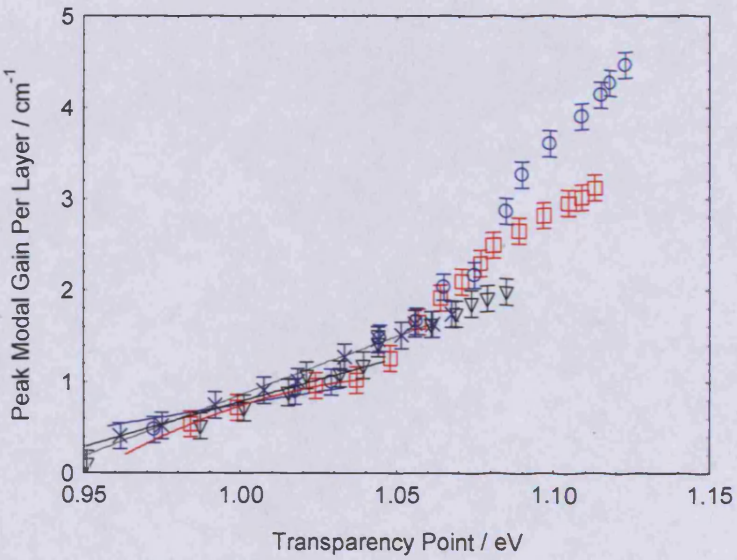

Figure 4.8: - The peak modal gain per layer as a function of the transparency point for the 3 layer (circles), 5 layer (squares), 7 layer triangles and 10 layer (crosses) devices.

The solid lines provide a guide to the eye as to when the peak gain is from the ground state. All four structures exhibit very similar behaviour over the injection range studied. As this is plotted as the gain per layer, the total gain available increases as the number of layers is increased. While operating on the ground state all four devices exhibit the same amount of gain per layer within the experimental uncertainty. The point at which the peak gain switches from the ground to excited state increases to

higher energies as the number of layers is increased. This increase goes from a value of 1.030 ± 0.005 eV for the three layer sample, to 1.065 ± 0.005 eV for the ten layer sample. Once operating on the excited state the three layer structure exhibits the most gain per layer, with a decreasing gain as the number of layers is subsequently increased. These two results are consistent with the conclusions drawn from the absorption data described previously suggesting there are a smaller percentage of high energy (short wavelength) states as the number of layers is increased. The higher layer samples can operate on the ground state up to higher injections as there are fewer higher energy states to contribute to the gain. Once the higher energy gain has become dominant it will be unable to reach such high gain values in the higher layer samples due to the reduced number of available states.

The data presented so far in this chapter has shown that the stacking of quantum dot layers is possible. The absorption data has illustrated that the density per layer of the larger dots is unaffected by the addition of extra layers, while the density of the smaller dots decreases in the higher layers. This results in devices operating on the ground state up to higher injection levels as the number of layers is increased (Figure 4.8). Combined with the higher total gain available for the structures with the largest number of layers, improved laser performance should be observed for these structures. To see if the predicted improvements occur, the gain-current characteristics can be determined and plotted for each structure. To enable direct comparison with laser performance the gain-current has been plotted as the total gain against the total current.

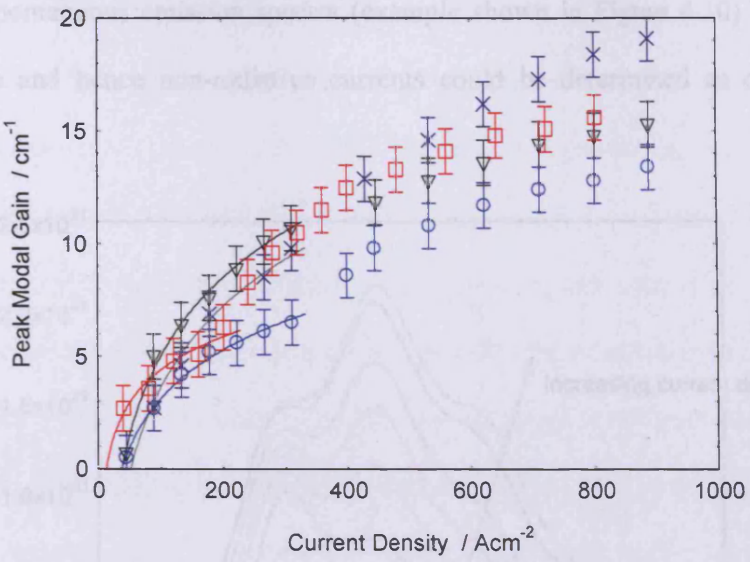

Figure 4.9: - Peak modal gain as a function of the drive current for the 3 layer (circles), 5 layer (squares), 7 layer (triangles) and 10 layer (crosses) structures.

The solid lines provide a guide to the eye to indicate when the peak gain is from the ground state transition, the gain available increases from the 3 to the 5 layer device; this is the expected result due to the increased number of quantum dots. However there is no subsequent increase as the number of layers increases to 7 and then 10 layers. The gain transparency relationships (Figure 4.8) indicated that higher gains could be achieved by increasing the number of stacked layers. The reason for these differences must be due to a change in the average current per layers as the number of layers is increased.

4.4 Radiative and non-radiative currents

The current is composed of radiative and non-radiative contributions; therefore both of these constituent parts need to be studied to account for the difference between Figure 4.8 and Figure 4.9. To achieve this, the segmented contact method was used to

obtain the spontaneous emission spectra (example shown in Figure 4.10) from which the radiative and hence non-radiative currents could be determined as described in chapter 2.

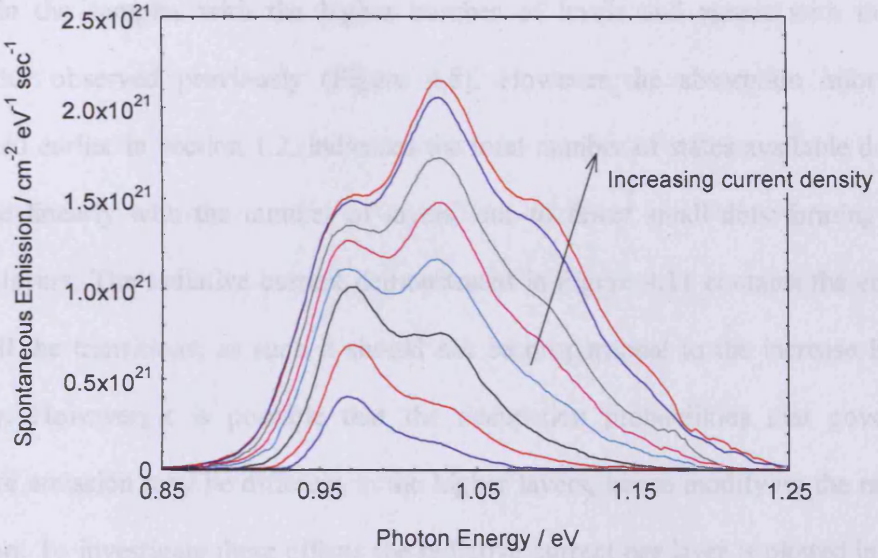

Figure 4.10: - Example spontaneous emission spectra for the 5 layer device.

The total radiative current from each device is plotted as a function of the transparency point in Figure 4.11.

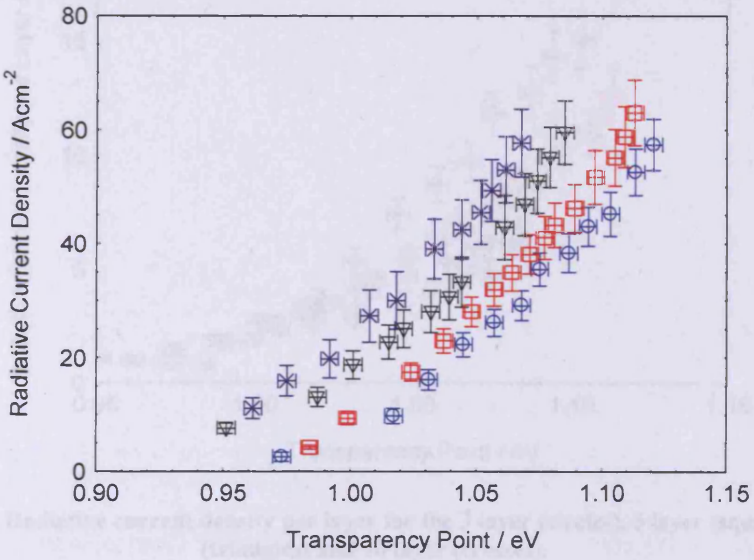

Figure 4.11: - Radiative current density as a function of transparency point for the 3 layer (circles), 5 layer (squares), 7 layer (triangles) and 10 layer (crosses) devices.

The radiative current achieved at a fixed injection level increases as the number of layers increases. This is again the expected behaviour due to the increased number of states in the samples with the higher number of levels and agrees with the gain behaviour observed previously (Figure 4.8). However the absorption information presented earlier in section 1.2, indicated the total number of states available does not increase linearly with the number of layers, due to fewer small dots forming in the higher layers. The radiative current demonstrated in Figure 4.11 contains the emission from all the transitions; as such it should not be proportional to the increase in layer number. However it is possible that the occupation probabilities that govern the radiative emission may be different in the higher layers, hence modifying the radiative emission. To investigate these effects the radiative current per layer is plotted in Figure 4.12.

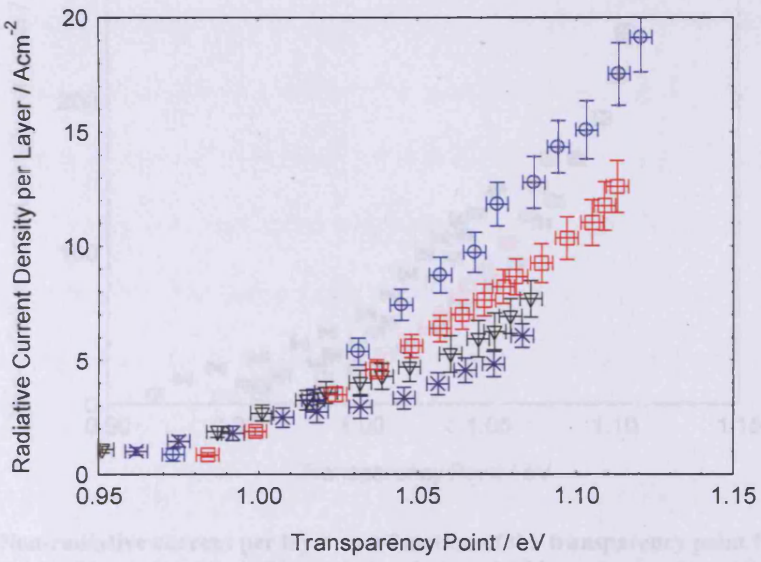

Figure 4.12: - Radiative current density per layer for the 3 layer (circles), 5 layer (squares), 7 layer (triangles) and 10 layer (crosses).

At low injection levels the radiative current per layer is approximately the same in each structure, this seems reasonable as at these injection values the light is predominantly from the ground state transition (~ 80% for the lowest injection shown in Figure 4.10). As was illustrated in the absorption data (section 1.2) the density of the larger dots is approximately the same in each layer, the light per layer from these states should be the same in each structure. At higher injection levels there is a much greater contribution from the higher states towards the spontaneous emission (Figure 4.10) and as described in section 1.2 there are a decreased number of states in the higher layers at these energies. It would be expected to observe reduced recombination per layer at these levels of injection and this is the trend observed in Figure 4.12.

The non-radiative current has then been determined by subtracting the radiative current from the total current as described in chapter 3 and is shown in Figure 4.13 for each structure as the non-radiative current per layer.

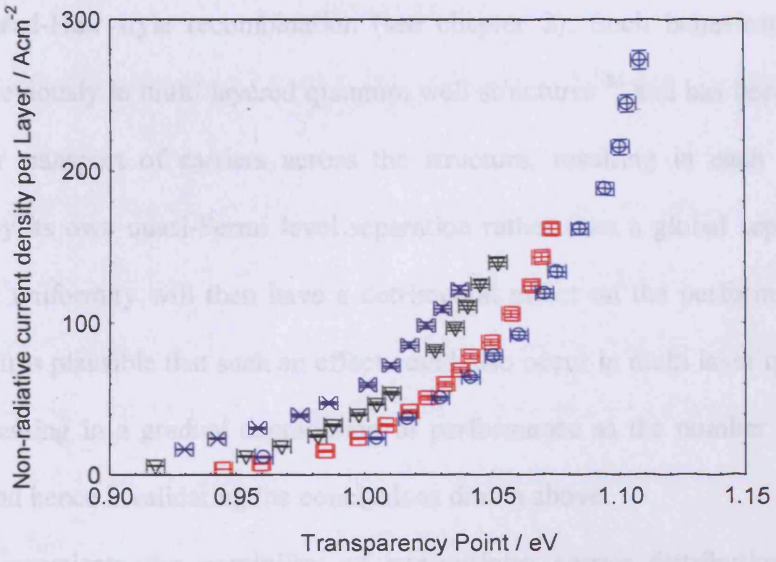

Figure 4.13:- Non-radiative current per layer as a function of the transparency point for the 3 layer (circles), 5 layer (squares), 7 layer (triangles) and 10 layer (crosses) samples.

The non-radiative current per layer increases as the number of layers is increased. The reason for this increase could be due to either an increase in defect

related recombination or elevated levels of Auger recombination. As discussed previously (chapter 3) Auger[27,70] recombination has been suggested to be the major source of non-radiative recombination in quantum dot structures, however the information in Figure 4.13 offers an alternative explanation. In this work the non-radiative current has been determined as a function of the transparency point. The transparency point is a measure of the injection level in the device (in other words the carrier density in the intrinsic region) therefore at a fixed transparency point for each structure the carrier density per dot is the same. Figure 4.13 shows that for a fixed transparency point a higher non-radiative current is obtained as the number of layers is increased, so the non-radiative rate increases as the number of dots are increased.

It is also possible that the cause of the additional non-radiative current is due to defect related processes. As the number of layers is increased it is conceivable that carriers are no longer injected equally over the whole structure, leading to a rise in Shockley-Read-Hall style recombination (see chapter 2). Such behaviour has been observed previously in multi layered quantum well structures [84] and has been attributed to the poor transport of carriers across the structure, resulting in each well being described by its own quasi-Fermi level separation rather than a global separation[85,86]. Such a non uniformity will then have a detrimental effect on the performance of the device[85,86]. It is plausible that such an effect could also occur in multi layer quantum dot devices, resulting in a gradual degradation of performance as the number of layers is increased and hence invalidating the conclusions drawn above.

To investigate the possibility of non-uniform carrier distributions in these samples the P_f function (equations 1.43 and 1.44) has been evaluated for each structure. If the entire structure can be described by a global quasi-Fermi level separation then the P_f function can be described by Fermi-Dirac statistics (as given in equation 1.44 and

illustrated in Figure 20, chapter 2). P_f functions recorded at various drive currents are shown in Figure 4.14, for the three layer sample, the solid lines are theoretical expressions obtained with Fermi-Dirac statistics using the relevant quasi-Fermi level separation (transparency point) obtained from the gain curves.

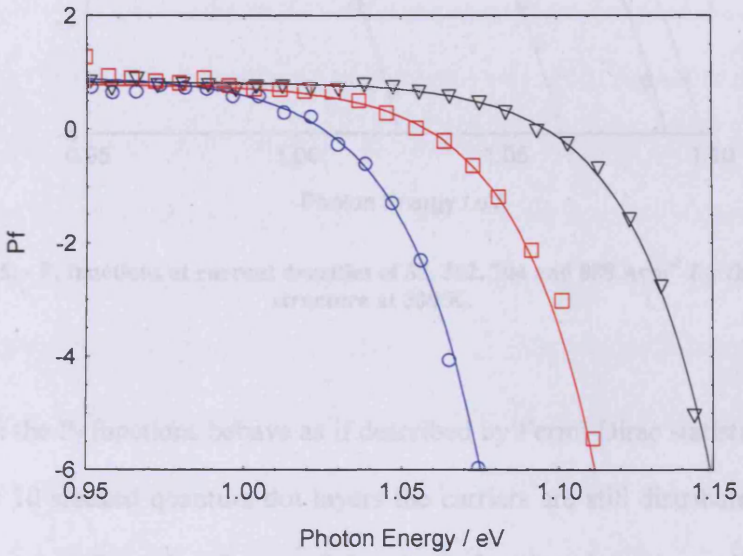

Figure 4.14: - P_f functions at drive current densities of 88, 352 and 704 Acm^{-2} for the three layer sample at 300 K.

These results show a good agreement between the experimentally obtained data and the expected thermal distributions over a range of injection currents. This is illustrates that up to three quantum dot layers can be stacked with the carriers still being injected uniformly. However it is possible that as the number of layers is increased further the carriers become less able to travel through the structure, resulting in a non-uniform distribution. To evaluate this, the Pf functions for the 10 layer structure along with the corresponding thermal fits are shown in Figure 4.15.

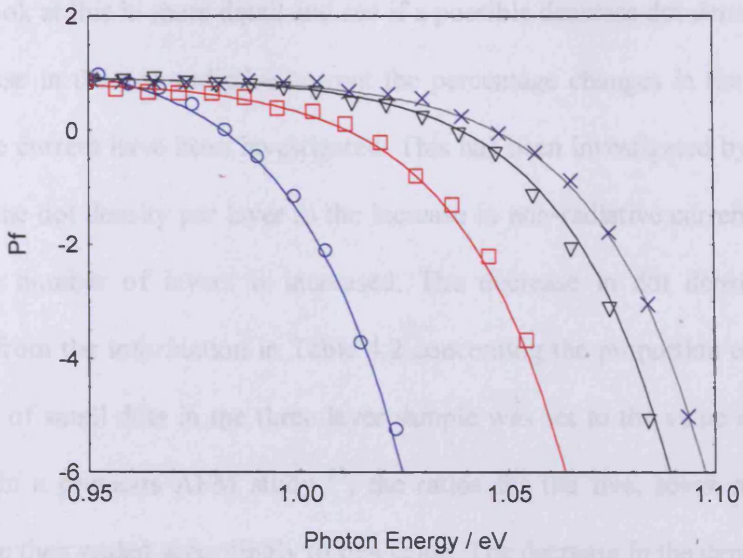

Figure 4.15: - P_f functions at current densities of 88, 352, 704 and 888 Acm^{-2} for the 10 layer structure at 300 K.

Again the P_f functions behave as if described by Fermi-Dirac statistics, implying that even for 10 stacked quantum dot layers the carriers are still distributed uniformly across the structure. Therefore from studying the P_f functions it has been shown that the carriers are distributed uniformly in the structures studied.

The additional non-radiative process could still however be linked to the number of defects present in each sample. If the density of defects was increased in each layer as the number layers was increased, the number of carriers per dot would decrease due to an elevated percentage of carriers recombining in the defects. At the same time the total amount of non-radiative recombination would also increase due to the elevated levels of defect (i.e. Shockley-Read-Hall) recombination. This scenario is consistent with the data recorded and presented in Figure 4.13, therefore suggesting that the dominant non-radiative channel in these structures could be defect related recombination.

To look at this in more detail and see if a possible decrease dot density is related to the increase in the non-radiative current the percentage changes in the density and non-radiative current have been investigated. This has been investigated by relating the decrease in the dot density per layer to the increase in non-radiative current density per layer as the number of layers is increased. The decrease in dot density has been determined from the information in Table 4.2 concerning the proportion of small dots. The number of small dots in the three layer sample was set to the value of small dots determined in a previous AFM study [53], the ratios for the five, seven and ten layer samples were then scaled accordingly to this value. The decrease in the density per layer relative to the three layer sample was then determined, giving three data points corresponding to the five, seven and ten layer samples. The relative increase in the non-radiative current density per layer was then determined from the information in Figure 4.13. This was again calculated relative to the three layer sample (i.e. the value of non radiative current for the three layer sample was subtracted from the five, seven and ten layer sample respectively). This analysis was performed at three values of transparency point of 1.00, 1.03 and 1.05 eV, while the uncertainties were determined using standard error analysis techniques and the values given in Table 4.2 and Figure 4.13.

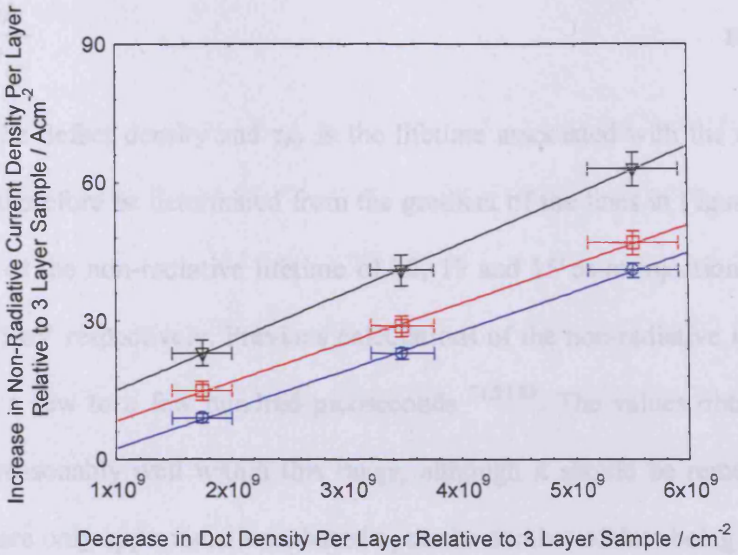

Figure 4.16: - Increase in the non-radiative current as function of the decreasing dot density at transparency points of 1.00 (circles), 1.03 (squares) and 1.05 (triangles) eV

All three injection levels show a linear relationship between the decreasing number of small dots per layer and the increasing amount of non-radiative current per layer. As the injection level is increased, the amount of non-radiative current increases, as expected from Figure 4.13. This data supports the idea postulated above that as the number of layers is increased, more defects are formed leaving less material for the formation of dots. To gain additional insight into whether this process is physically reasonable an estimate of the non-radiative lifetime associated with these defects can be calculated.

If it is assumed that the decrease in dot density corresponds exactly to the increase in the defect density (so for each additional defect there is one less dot), then the x-axis on Figure 4.16 can be thought of as the defect density. The y-axis then gives the non-radiative current associated with that number of defects. The non-radiative recombination associated with this process is then given by,

$$J_{Non-Rad} = \frac{eN}{\tau_{Nr}}$$ **Equation 4.1**

where N is the defect density and τ_{Nr} is the lifetime associated with the defects. The lifetime can therefore be determined from the gradient of the lines in Figure 4.16. This gives values of the non-radiative lifetime of 20, 19 and 15 ns at injection levels of 1, 1.03 and 1.05 eV respectively. Previous calculations of the non-radiative lifetime have ranged from a few to a few hundred picoseconds [74,87,88]. The values obtained in this work agree reasonably well within this range, although it should be remembered that these values are only approximations, based upon the number of dots being calibrated to previous AFM data on a different sample [53] and assuming that each defect formed results in one less dot.

The exact origin of the additional defects as the number of layers is increased is unclear, although a variety of defects and dislocations have been described previously in multi layered samples [80-82]. The formation of additional defects would also explain the reduced dot density observed in the higher layers (see section 1.2); however it still remains unclear as to why the defects appear to only inhibit the formation of smaller dots. It may be the case that the additional defects are formed from the larger dots, at the same time that this occurs the number of small dots going to form larger dots may also increase as the number of layers is increased at approximately the same rate. As such an equilibrium situation would be created where the number of large dots remains constant in each layer, while the number of small dots decreases.

4.5 Conclusions

The work described in this chapter has been concerned with evaluating the effects of stacking quantum dot layers. From modal absorption and gain measurements it has been shown that as additional layers are added to the structure the overall dot density distribution alters, resulting in a higher fraction of large dots. This occurs due to the density of the larger subset of dots remaining constant across the layers, while the density of the smaller dots decreases in the higher layers. This seems to occur due to an increased number of defects being formed in the higher layers, reducing the amount of material available to form dots.

The possibility that the structures do not have a uniform carrier distribution has been investigated. Through studying the behaviour of the P_f functions it has been possible to show that the carriers are evenly distributed across all the structures and that up to 10 layers can be stacked without any detrimental effects due to the carrier distributions.

By being able to determine the non-radiative current as a function of the carrier density it has been shown that the most likely cause of the additional non-radiative process is due to an increased number of defect states. This has been supported with good agreement between the decrease in dot density and corresponding increase in non-radiative current, along with the determination of a physically reasonable non-radiative lifetime. However the possibility of Auger style processes cannot be entirely discounted from having an effect.

5. The effect of modulation doping on the performance of InAs Quantum dots

5.1 Introduction

The work in the previous two chapters has investigated the possibility of increasing the available modal gain in quantum dot lasers by increasing the number of states (i.e. the number of dots). This has been attempted by careful engineering of the GaAs spacer layer and through stacking quantum dot layers. However these structures still suffer from lower than expected values of modal gain, due to the incomplete occupation of these states. This incomplete state filling shall now be discussed along with a possible solution.

It was initially predicted that quantum dot lasers would exhibit near ideal laser performance[89-91] due to the use of only a single hole and electron being required to reach transparency. However as the valence mass in III – V material systems is much larger than the corresponding conduction mass, the allowed hole energy levels are much closer spaced than the electron levels. A further complication of this difference in masses is the much larger density of states for the holes in the wetting layer compared to the holes. These factors result in an asymmetric movement in the quasi-Fermi levels into the conduction or valence bands. This situation has been modelled using Simwin version 1.5 [92,93] and an example is illustrated in Figure 5.1 for a typical quantum dot system under flat band conditions, with charge neutrality (i.e. $n = p = 2 \times 10^{17}$ cm^{-3}). Flat band conditions were achieved by applying a forward bias of 1.43 V across the structure. Simwin is a commercially available software package that simulates semiconductor device performance by solving semiconductor equations in one

dimension (therefore variables vary parallel to the flow of the current and are uniform perpendicular to it).

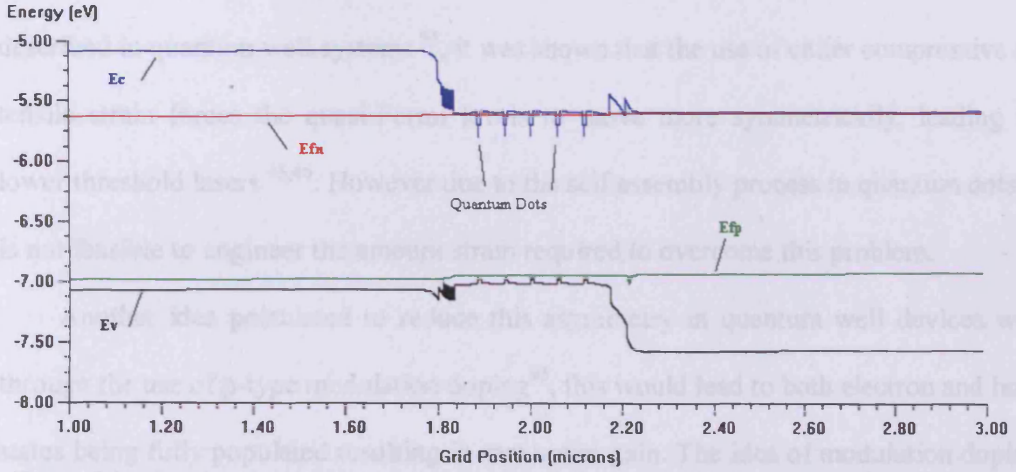

Figure 5.1: - Conduction and Valence band diagram for a typical InAs quantum dot system, also illustrated are the positions of the quasi-Fermi levels for the electrons and holes.

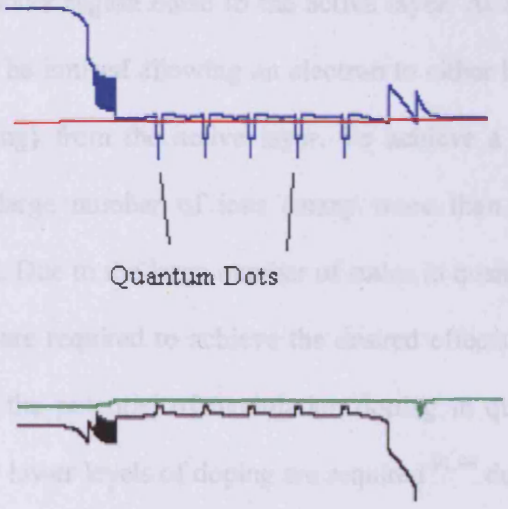

Figure 5.2: - Conduction and Valence band diagram across the active region.

Here it can clearly be seen that the electron quasi-Fermi level is situated well within the electron dot states, resulting in a high occupation of electrons. However the hole quasi-Fermi level is still placed above all the valence band states. The occupation of these states is then determined by the product of the density of states and the Fermi function. Therefore due to the large number of wetting layer states and the given Fermi

function there is only a small probability of the dot valence states being occupied with holes. This will then have limiting effects on the level of gain that can be achieved.

Although similar asymmetric behaviour in the quasi-Fermi levels has been described in quantum well systems [94], it was shown that the use of either compressive or tensile strain forces the quasi-Fermi levels to move more symmetrically, leading to lower threshold lasers [45,46]. However due to the self assembly process in quantum dots it is not feasible to engineer the amount strain required to overcome this problem.

Another idea postulated to reduce this asymmetry in quantum well devices was through the use of p-type modulation doping[95], this would lead to both electron and hole states being fully populated resulting in maximum gain. The idea of modulation doping involves placing a concentration of either acceptor or donor ions (for p or n type doping respectively) in the barrier region close to the active layer. At an appropriate thermal energy these will then be ionised allowing an electron to either be donated or removed (for n or p type doping) from the active layer. To achieve a modest population of additional carriers a large number of ions (many more than the number of states available) are required. Due to the large number of states in quantum well systems very high levels of doping are required to achieve the desired effects making this approach un feasible. However the potential of modulation doping in quantum dot systems is much more realistic as lower levels of doping are required [91,96] due the lower number of available states within the dots.

The idea of incorporating p type modulation doping in quantum dot systems has attracted a lot of interest over the past few years. This has been generated by reports from several groups of improved device performance (temperature insensitive threshold current and increased modulation bandwidths)[77,97,98]. Detailed modelling of p doped quantum dot structures [96,99] has predicted reduced threshold current and improved

modulation response due to an increased peak modal gain and differential gain. These results have also been shown to be consistent with experimental data including laser wavelength measurements as a function of cavity length[100]. High modal gain has also been reported from p doped quantum dots that incorporate tunnelling injection structures and emit at 1.1 μm [101].

However there have also been reports of increasing non radiative recombination in p doped quantum dot structures [102-104], measured by increasing threshold current densities when compared to intrinsic structures. This has resulted in claims that the benefits of p doping are limited, at best.

In this work the effect of modulation doping on quantum dot structures emitting at 1.3 μm is evaluated using a set of intrinsic, p and n type modulation doped structures. The segmented contact method (described in chapter 2) has been used to fully characterise the modal absorption, modal gain and the relative fractions of radiative and non-radiative recombination in all the structures.

Initially five structures were studied in this part of the work, the first of these was an undoped control structure; this was simply a repeat of the growth of the HGTSL sample studied in chapter 3 [52]. Along with this two p–type modulation doped structures were grown, one that had 15 acceptors ions per dot and one with 50 acceptors per dot. Similarly two n – type doped devices were also grown with 15 and 50 donors per dot. All the doped devices had the same nominal design as the control sample except for the presence of the dopants, which were placed in a 6 nm region of GaAs positioned 9 nm before the start of each DWELL. The dopants consisted of Be atoms for the p – type doping and of Si for the n – type. The number of dots present was previously determined by AFM measurements on un capped samples of the HGTSL device[53] (4 X 10^{10} cm^{-2}) and it was this density that was used to determine the density of dopants

required. To try and inhibit the dopants from diffusing through the barrier and into the active region, the temperature was lowered for the dopant-containing region of GaAs, as outlined in Table 5.1. This means that for the four doped structures the first 15 nm of GaAs were grown at 510 ^{0}C, before being increased to 580 ^{0}C (as in the control sample), the temperature was cooled to 510 ^{0}C for the final 15 nm to allow the dopants to be incorporated.

	Growth temperature of 1st 15 nm of GaAs / ^{0}C	**Growth temperature of next 20 nm of GaAs / ^{0}C**	**Growth temperature of final 15 nm of GaAs / ^{0}C**
Un doped	510	580	580
p X 15 dopants	510	580	510
p X 50 dopants	510	580	510
n X 15 dopants	510	580	510
n X 50 dopants	510	580	510

Table 5.1 : - Details of the GaAs spacer layer growth temperatures for the 5 structures.

5.2 Modal Absorption Data

The segmented contact method was used to obtain modal absorption plots for all five devices. They are shown in Figure 5.3 in two plots, one with the n – type doped devices plotted along the nominally undoped device and a second plot showing the p – type devices with the undoped structure.

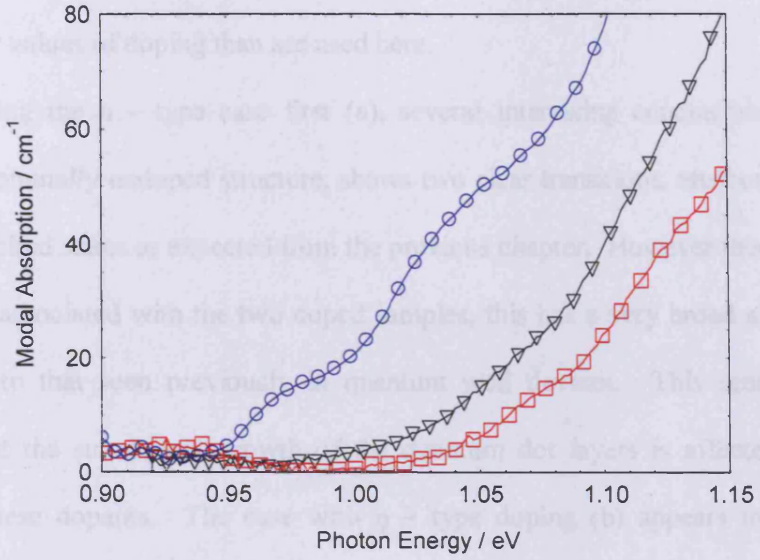

(a)

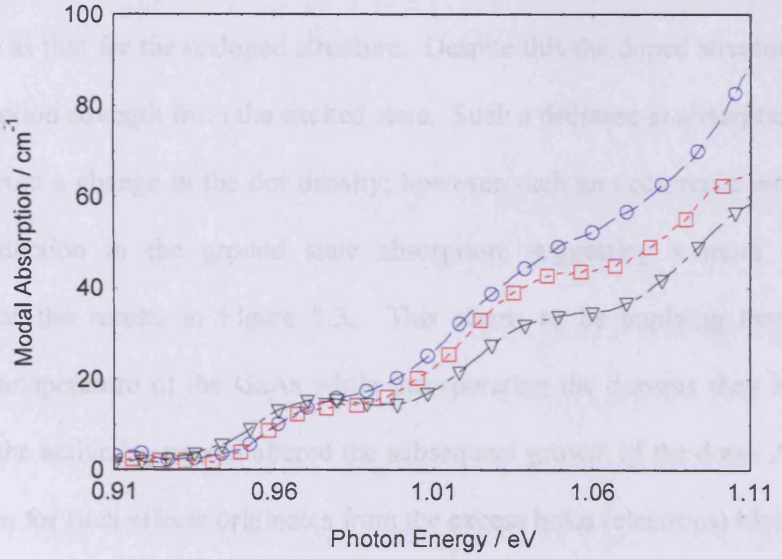

(b)

Figure 5.3: - Modal Absorption plots for undoped, n - type and p -type modulation doped devices. (a) Undoped device (Circles), n - type X 15 (Squares), n - type X 50 (Triangles). (b) Un doped (circles), p - type X 15 (Squares) amd p - type X 50 (Triangles).

All five samples have the same value of internal loss, within the accuracy of the experiment yielding a result of 2 ± 2 cm^{-1}. This agrees with a previous study, where the waveguide loss was inferred from laser results taken as a function of cavity length[105].

In that study only a small increase was observed in the waveguide loss and this occurred at much higher values of doping than are used here.

By studying the n – type case first (a), several interesting conclusions can be drawn. The nominally undoped structure, shows two clear transitions, attributed to the ground and excited states as expected from the previous chapter. However there is only one transition associated with the two doped samples, this has a very broad absorption edge, similar to that seen previously in quantum well devices. This seems to be suggesting that the subsequent growth of the quantum dot layers is affected by the presence of these dopants. The case with p – type doping (b) appears to be very different, here both the doped devices have two transitions corresponding to the ground and excited state transitions. Furthermore the transitions occur at approximately the same energies as that for the undoped structure. Despite this the doped structures show reduced absorption strength from the excited state. Such a decrease in absorption would be expected from a change in the dot density; however such an occurrence would also lead to a reduction in the ground state absorption, suggesting a more complex explanation for the results in Figure 5.3. This seems to be implying that despite reducing the temperature of the GaAs while incorporating the dopants they have still diffused into the active layers and altered the subsequent growth of the dots. A second possible reason for such effects originates from the excess holes (electrons) blocking the true absorption. If some of the dots are occupied by excess holes (or electrons) they will not undergo absorption and lead to a reduced value being measured due to Pauli state blocking. Evidence for this claim, is found by repeating the absorption measurement, with a reverse bias being applied across the passive segment. This voltage helps extract the excess carriers allowing an increased absorption to be

measured; Figure 5.4 shows how the absorption alters for the 50 p dopant sample as a function of the reverse bias.

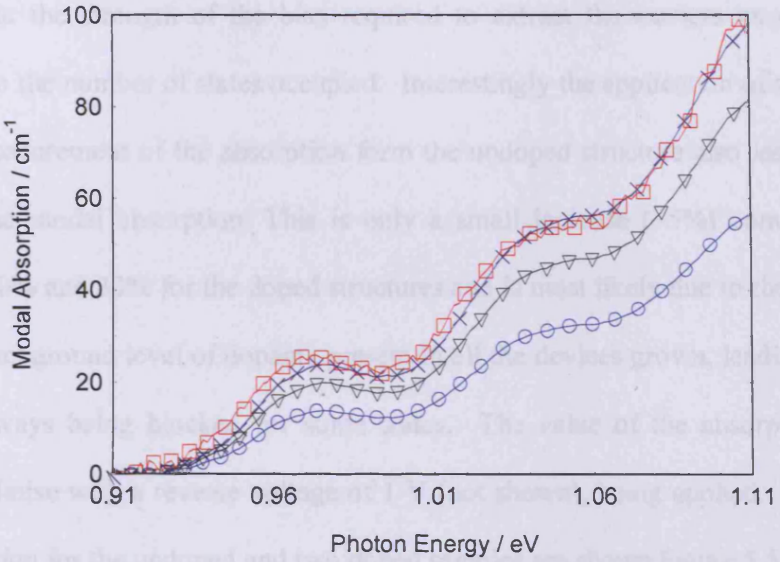

Figure 5.4: - Modal Absorption as a function of photon energy for P X 50 Dopants. For reverse biases of 0 V (circles), 1 V (triangles), 2 V (squares) and 3 V (crosses).

As the bias is changed from 0 to 2 V, a clear increase in the magnitude of the absorption can be seen. This is due to the fact that the holes occupying the highest energy states will be extracted first. A final increase to a reverse bias of 3 V shows no further change, indicating that the maximum (true) absorption is obtained with a 2 V bias. Other studies on quantum dot structures have shown evidence of a Quantum Confined Stark Effect, by measuring the absorption as a function of bias[106,107]. Such an effect is caused by a misalignment of the electron and hole wavefunctions due to the inbuilt field within the p-i-n junction. A reverse bias then sets up a field to counteract this effect enabling the wavefunctions to be aligned. As well as leading to increased absorption strength the transition peaks are also shifted by this effect. As in these measurements no change in the ground or excited state peak positions is observed, any Quantum Confined Stark Effect is evidently small in these samples. This screening of the excess absorption, obviously also affects the lower p doped sample (15 acceptors

per dot), as before a reverse bias extracts the excess holes allowing the true absorption to be measured. The maximum absorption is again reached for a reverse bias of 2 V, suggesting that the strength of the bias required to extract the carriers may not be proportional to the number of states occupied. Interestingly the application of a reverse bias to the measurement of the absorption form the undoped structure also leads to an increase in the modal absorption. This is only a small increase (~5%) compared to increases of 20% and 33% for the doped structures and is most likely due to there being an inherent background level of dopants present in all the devices grown, leading to the absorption always being blocked for some states. The value of the absorption was found to maximise with a reverse voltage of 1 V (not shown), being applied. The true modal absorption for the undoped and two doped samples are shown Figure 5.5.

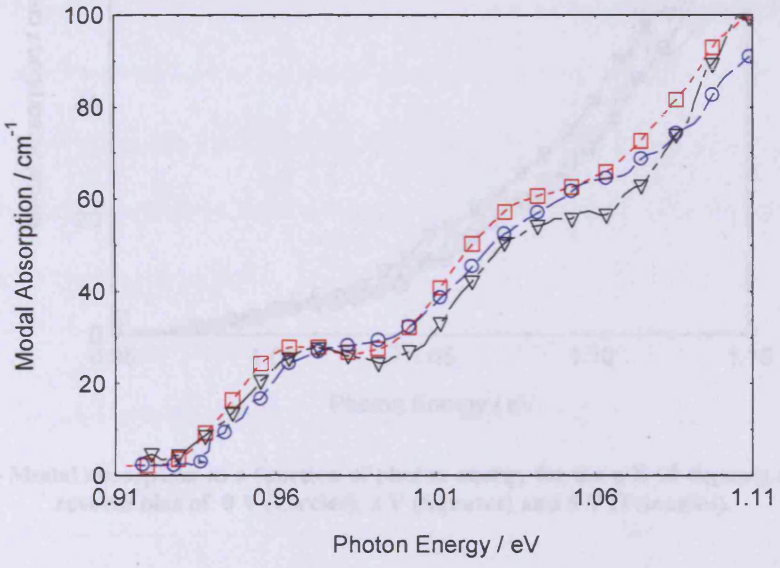

Figure 5.5: - Modal absorption as a function of photon energy, with a reverse bias of 2 V applied for the undoped (Circles), P X 15 (Squares) and P X 50 (Triangles) doped devices.

As well as the ground and excited state transitions occurring at the same energies the samples now exhibit a similar level of broadening and strength for the transitions. This result means that the electronic states of the quantum dots have not been affected by the introduction of the dopants. The values of the waveguide loss from

all three samples have not been affected by the application of the bias, and still give the same value within the experimental uncertainty.

Having observed this effect of changing the absorption by applying a reverse bias, it is prudent to re consider our earlier conclusions on n type doping, drawn from Figure 5.3. Here we concluded that the presence of the dopants resulted in different dot growth leading to the broad and shifted absorption curve shown. However it could be the case that the excess electrons are also causing the true absorption to be blocked in the same way. To evaluate this possibility a reverse bias was also applied across the n – doped devices.

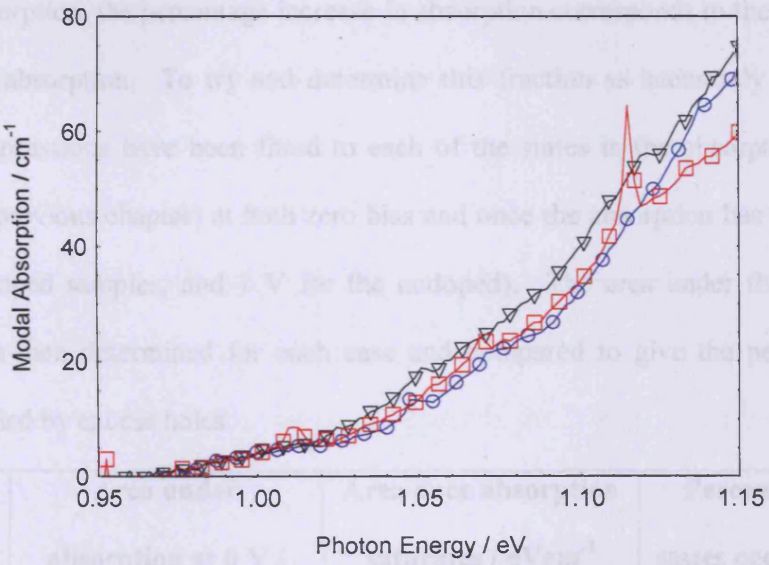

Figure 5.6: - Modal absorption as a function of photon energy for the n X 50 dopants device with a reverse bias of 0 V (Circles), 2 V (Squares) and 5 V (Triangles).

Here there is very little effect with the application of the reverse bias (only a slight increase at high energies for the largest bias used, confirming the earlier conclusion that the presence of n type dopants results in different dot formation. The same result (no shift in absorption with increasing reverse bias) was observed for the lower doped (15 n-dopants per dot) device. These results have shown that the introduction of n type modulation doping leads to a change in the formation of the

quantum dots. This results in a higher energy (hence shorter wavelength) absorption peak as well as a broader transition energy. However the incorporation of p type modulation has no effect on the growth of the quantum dots. As n type results in the formation of different dots any comparisons on performance (gain, efficiency, etc.) with the undoped or p doped structures would be invalid. As such the remainder of this chapter will only be concerned with the p type and the undoped structures.

The increase in the absorption strength for the p-doped structures should allow the percentage of states occupied by excess holes to be determined. As the increase in the absorption is attributed to the removal of excess carriers, enabling more states to undergo absorption, the percentage increase in absorption corresponds to the extra states that exhibit absorption. To try and determine this fraction as accurately as possible Gaussian expressions have been fitted to each of the states in the absorption (as was done in the previous chapter) at both zero bias and once the absorption has saturated (2 V for the doped samples, and 1 V for the undoped). The area under the combined Gaussians is then determined for each case and compared to give the percentage of states occupied by excess holes.

	Area under absorption at 0 V / $eVcm^{-1}$	**Area once absorption saturates / $eVcm^{-1}$**	**Percentage of states occupied by excess holes.**
Un doped	12.1	12.74	**5**
P X 15	9.96	12.51	**20**
P X 50	8.69	12.98	**33**

Table 5.2: - Reference table giving the percentage of states occupied by excess carriers.

So for the undoped sample, 5 % of the states are occupied by excess holes due to background impurities when the sample was grown. The results for the two doped structures are rather interesting, despite being doped to a level of 15 (or 50) acceptors per dot, only 20 % (or 33%) of the dot states are occupied by these holes. The greater the number of ionised acceptors, the larger the number of excess holes provided to the system, therefore this fraction needs to be maximised. The occupation numbers obtained here seem rather low and there are several reasons for this. Firstly the concentration of acceptor ions used was determined from AFM of measurements the dot density on a similar un capped device[53]; obviously the density in these samples could be different. However it is unlikely that the density has changed by such a large factor to result in these relatively low numbers. We know that in quantum dot lasers there are many more wetting layer states than dot states (several orders of magnitude) [32] and that for a thermal distribution of carriers amongst the available states the population of these wetting layer states is a significant contributing cause of the gain saturation we are trying to overcome with p-doping. Therefore it seems more likely that the excess holes are occupying states in the wetting layer (and possibly the DWELL states), reducing the number of dot states being occupied. This result is therefore a further indication that the low population of the hole dot states is an important mechanism in dot lasers.

5.3 Modal Gain Data

The segmented contact technique has again been utilised to obtain modal gain spectra (see chapter 2), for the undoped and both of the p doped structures. Example spectra are shown below for the undoped structure at a range of drive currents.

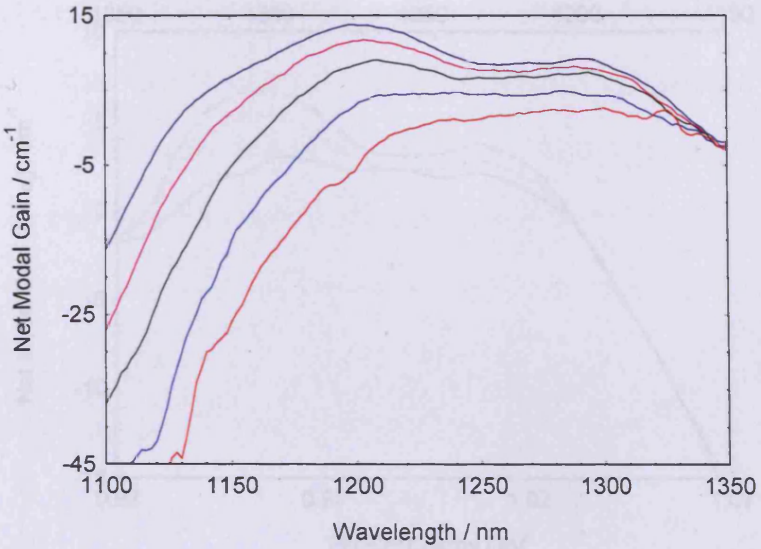

Figure 5.7: - Modal Gain Spectra for the undoped device at current densities of 122, 222, 344, 532 and 668 Acm^{-2}

Similar spectra were also recorded for the two doped structures. As with the HGTSL sample, described in the previous chapter, gain is exhibited from both the ground and excited state. The energy at which peak gain occurs switches between the states after the second curve (at a current density of 222 Acm^{-2}). It can also be seen that the curves come together well at long wavelength to give a value of α_i ($2 \pm 2cm^{-1}$) in good agreement with that obtained from the absorption spectra seen previously. Gain spectra are compared in Figure 5.7 for the undoped and doped samples, for the same transparency point (but requiring different injection currents).

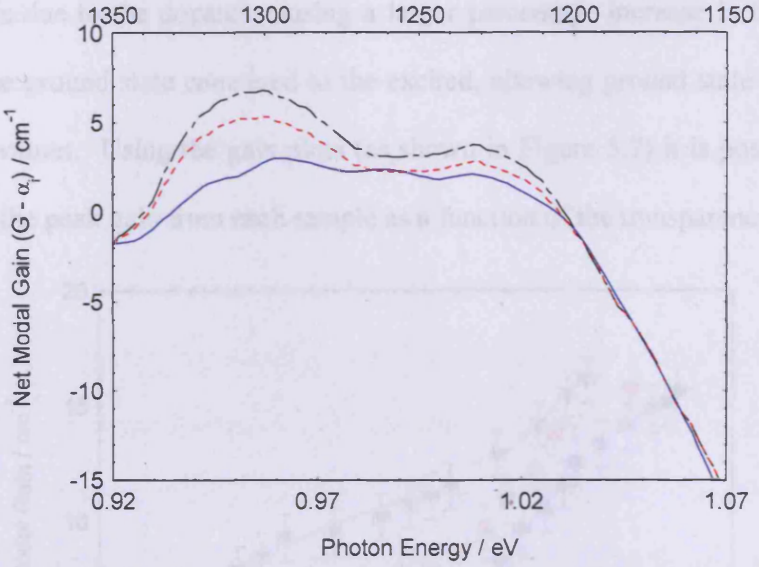

Figure 5.8: - Modal gain spectra at a transparency point of 1.035 eV for the undoped (solid line), 15- p dopant (dashed line) and 50 p-dopant (dashed and dotted line) samples.

Several interesting points can be noted about this plot, firstly all three samples, give the same value of α_i of 2 ± 2 cm^{-1} which is in agreement with the absorption data shown in Figure 5.3. At energies above the transparency point all three samples exhibit the same gain. This is the behaviour expected as once above the transparency point the samples undergo negative gain (absorption) and as Figure 5.5 showed the three devices all have the same absorption. Although all three curves show gain from both the ground and excited states (situated at 0.955 and 1.011 eV respectively) the amount of gain available is drastically different in the three cases. As the level of doping is increased from 0 to 15 acceptors per dot; the amount of gain increases, for both ground and excited states. As the doping is further increased to 50 acceptors per dot the gain continues to increase at both states. The ground and excited peaks also appear to be sharper for the two doped cases than the intrinsic sample due to the higher levels of gain that can be obtained in these samples. The value of the peak gain from the ground and excited states is approximately the same for the intrinsic sample, however for both of the doped samples there is clearly more gain from the ground state than the excited.

This effect is due to the dopants causing a larger percentage increase in the available gain from the ground state compared to the excited, allowing ground state operation at higher gain values. Using the gain plots (as shown in Figure 5.7) it is possible to plot (Figure 5.9) the peak gain from each sample as a function of the transparency point.

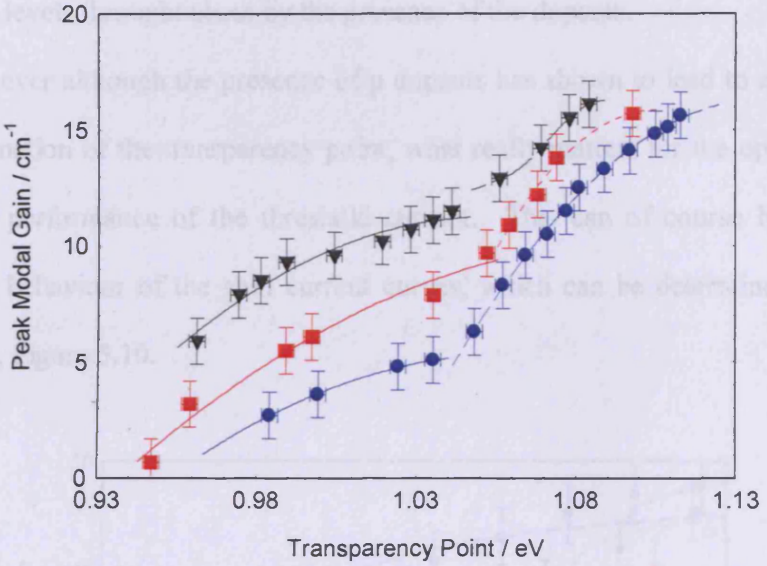

Figure 5.9: - Modal Gain as a function of the transparency point for the undoped (circles), the P X 15 (squares) and P X 50 (triangles) doped structures.

For each curve the solid line represents a guide to the eye to demonstrate where the peak gain is from the ground state, while the dashed lines form a guide to the eye as to where the gain is from the excited state.

This plot clearly shows that the dopants have increased the amount of gain available at all energies (as expected from Figure 5.7). Figure 5.7 showed the change over from ground to excited state being delayed for the doped devices, this is further supported by the data in Figure 5.8. Here it can be seen that the undoped device switches to the excited state at an energy of 1.040 eV, however the 15 and 50-p dopant samples do not switch to the excited state until 1.047 and 1.052 eV respectively. This illustrates that the doped samples can be driven harder before the gain switches to shorter wavelengths. As mentioned in chapter 2 if the carriers are described by a

thermal distribution then the transparency point is equal to the quasi-Fermi level separation. Therefore Figure 5.9 is showing that for a fixed quasi-Fermi level separation an increased gain is achieved from the p-doped structures, supplying evidence that improvements in p-doped structures are due to a reduction in the asymmetry of the quasi-Fermi levels, brought about by the presence of the dopants.

However although the presence of p dopants has shown to lead to an improved gain as a function of the transparency point, what really matters for the operation of a laser is the performance of the threshold current. This can of course be predicted through the behaviour of the gain current curves, which can be determined from the gain spectra, Figure 5.10.

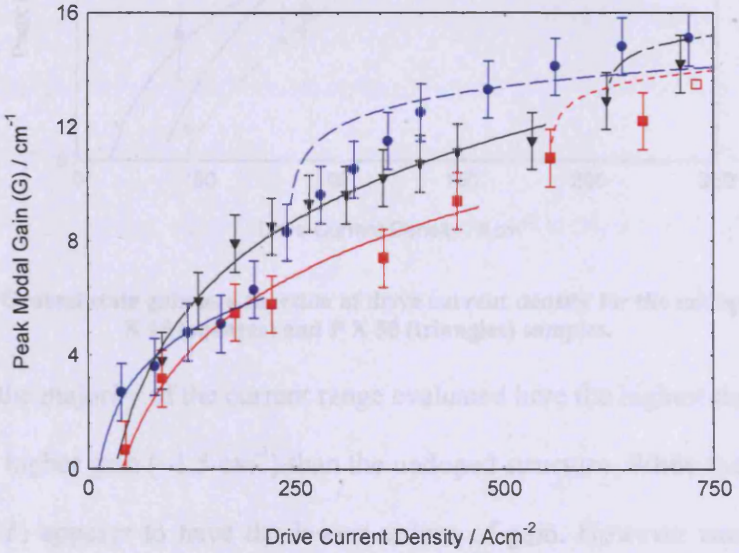

Figure 5.10: - Peak Gain as a function of drive current for the undoped (circles), P X 15 (squares) and P X 50 (triangles) samples.

In Figure 5.10 the solid (dashed) lines represent a guide to the eye as to when the peak gain is from the ground (excited) state. From this graph the operation of the three samples appears to be much more complicated. Above a current of 250 Acm^{-2} the undoped device clearly has a higher level of gain until we reach very high currents. However over this range the undoped device is operating on the excited state while the

two doped samples are both still operating on the ground state. Therefore although a greater gain can be obtained from the standard structure, this will be of no use for laser operation at 1.3 μm.

Below a current of 250 Acm^{-2} where all the devices are still operating on the ground state the behaviour is much more complex than that expected from Figure 5.8.

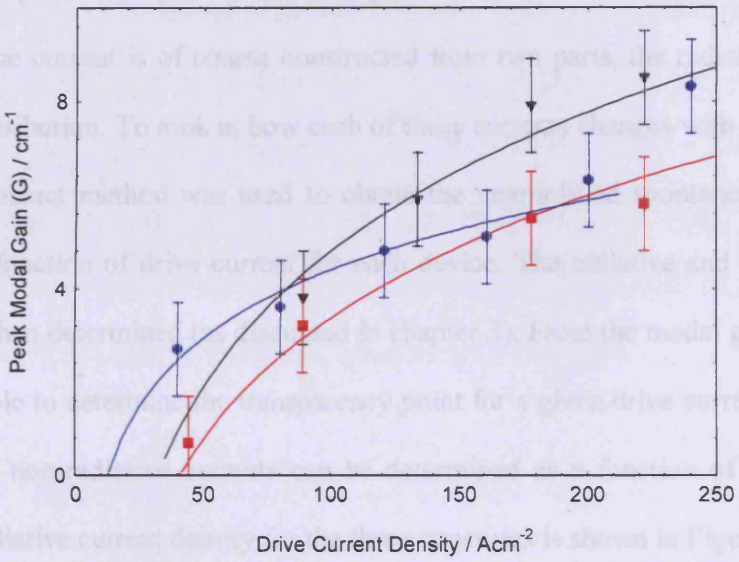

Figure 5.11: - Ground state gain as a function of drive current density for the undoped (circles), P X 15 (squares) and P X 50 (triangles) samples.

Over the majority of the current range evaluated here the highest doped structure has a slightly higher gain (~1.5 cm^{-1}) than the undoped structure. While the lower doped device (p x 15) appears to have the lowest values of gain. However each of the data points has an error of around ± 1 cm^{-1}, which is of a comparable size to the differences seen in Figure 5.10. These uncertainties make it unfeasible to distinguish between the three samples at these low current densities.

5.4 Radiative and Non-Radiative Recombination

Although Figure 5.8 shows that the highest doped device exhibits more than twice as much gain from the ground state at a fixed transparency point when compared to the intrinsic device, as a function of current, there is only a small improvement. As the transparency point gives the level of carrier injection, this implies that equal currents do not correspond to equal levels of injection between the doped and undoped structures. The current is of course constructed from two parts, the radiative and non-radiative contribution. To look at how each of these currents changes with injection, the segmented contact method was used to obtain the unamplified spontaneous emission spectra as a function of drive current for each device. The radiative and non-radiative currents are then determined (as discussed in chapter 3). From the modal gain spectra it is then possible to determine the transparency point for a given drive current; hence the radiative and non-radiative currents can be determined as a function of the injection level. The radiative current density for the three structures is shown in Figure 5.12.

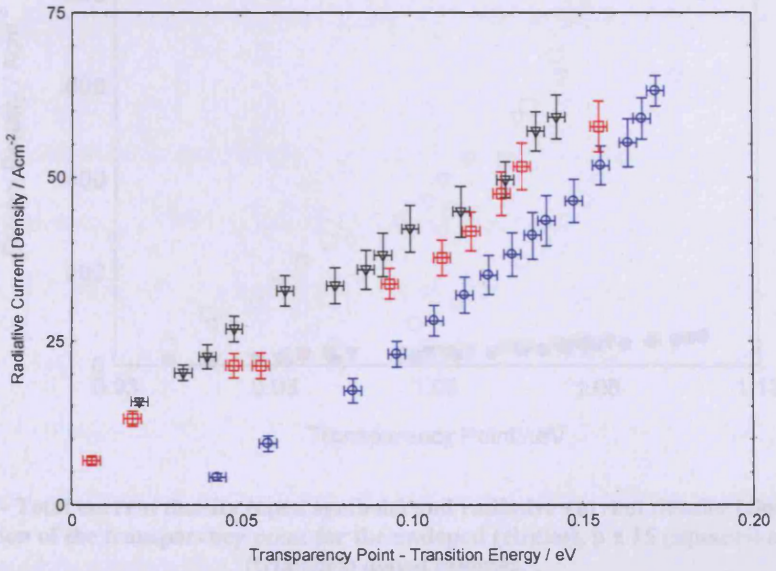

Figure 5.12: - Radiative current density as a function of transparency point for the undoped (circles), p x 15 (squares) and p x 50 (triangles) doped samples.

The amount of radiative current at a fixed injection level, increases for the 15-dopant structure relative to the undoped, there is then a slight further increase as the doping is increased to 50 dopants. An increased radiative current would lead to a rise in the total current density. However the dramatic change of form between the gain as a function of transparency point to a function of current (Figure 5.8 to Figure 5.9) cannot be accounted for by this increase in radiative current. Figure 5.11 shows an increased radiative current of ~ 20 – 30 Acm^{-2}, however this is only a small fraction (<10%) of the total current required to achieve high values of gain (Figure 5.9). Therefore it seems likely that there must also be higher levels of non-radiative recombination in the doped structures, a result seen previously[103] along with reports of a decreased non-radiative lifetime[102]. The non-radiative current can be determined from the difference between the radiative and the total current; these are plotted together in Figure 5.13.

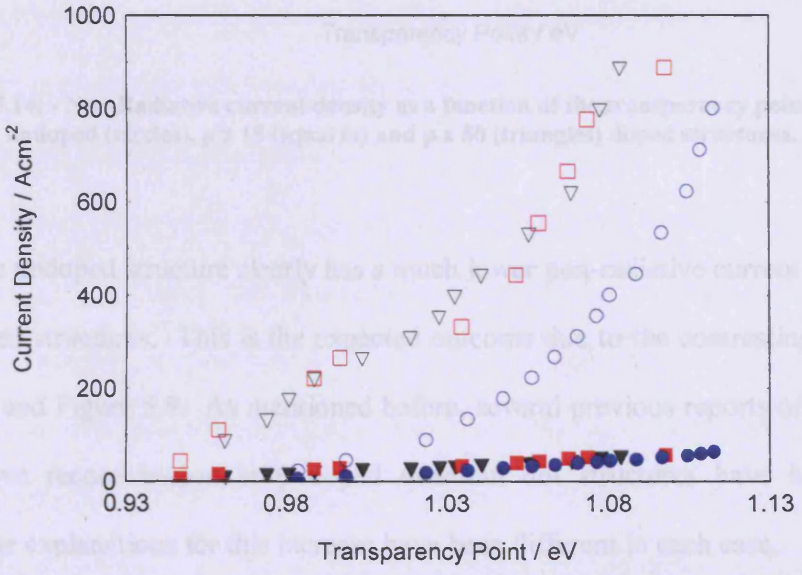

Figure 5.13: - Total current density (open symbols) and radiative current density (closed symbols) as a function of the transparency point for the undoped (circles), p x 15 (squares) and p x 50 (triangles) doped samples.

The total non-radiative current can then be determined from the difference between the total current (open symbols) and the radiative current contribution (closed

symbols) for each structure. It can clearly be seen that although the radiative current increases with the presence of p-type dopants (Figure 5.11), there is also a much larger increase in the total current at a fixed transparency point. Therefore the difference between the curves (the non-radiative current) is increasing for the structures containing p dopants and this is shown explicitly in Figure 5.14.

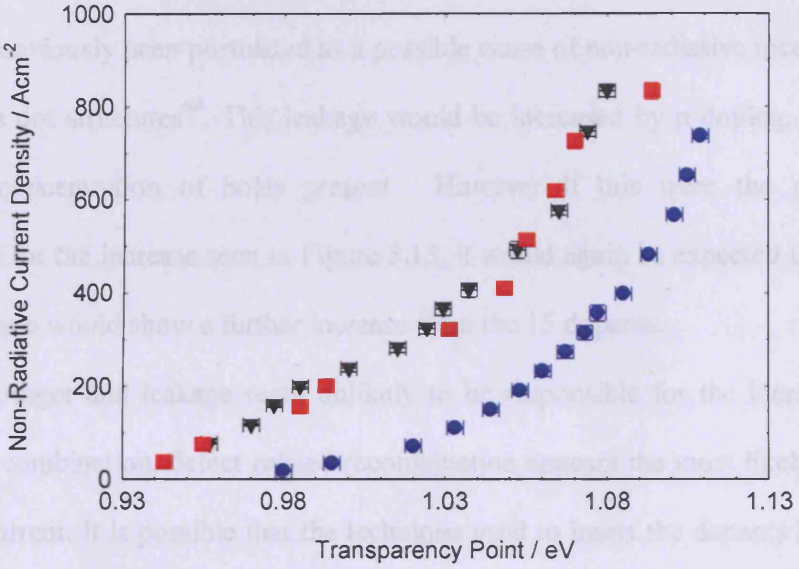

Figure 5.14: - Non-Radiative current density as a function of the transparency point for the undoped (circles), p x 15 (squares) and p x 50 (triangles) doped structures.

The undoped structure clearly has a much lower non-radiative current than either of the doped structures. This is the expected outcome due to the contrasting results in Figure 5.8 and Figure 5.9. As mentioned before, several previous reports of increasing non-radiative recombination in p doped quantum dot structures have been made, although the explanations for this increase have been different in each case.

Several authors have attributed the increased non-radiative recombination to increased Auger recombination[77,103,104] caused by the large number of additional holes supplied by p doping. However if an Auger process were responsible for the extra non-radiative recombination, the process should get worse as the number of holes (the

doping concentration) increases, unless it undergoes saturation for high carrier concentrations. Figure 5.13 clearly shows that the two doped structures have very similar levels of non-radiative current associated with them. This seems to suggest that the increased non-radiative current is not due to an Auger process, as the non-radiative current seems independent of doping level (between 15 and 50 acceptors per dot).

The leakage of holes from quantum dot states to wetting layer and higher lying states has previously been postulated as a possible cause of non-radiative recombination in quantum dot structures[69]. This leakage would be increased by p doping, due to the increased concentration of holes present. However if this were the mechanism responsible for the increase seen in Figure 5.13, it would again be expected that the 50-dopant sample would show a further increase from the 15 dopants.

As Auger and leakage seem unlikely to be responsible for the increased non-radiative recombination, defect related recombination appears the most likely origin of the extra current. It is possible that the technique used to insert the dopants has lead to an increase in the number of non-radiative centres resulting in an increase in Shockley-Read-Hall recombination (see chapter 1).

As mentioned previously, due to concerns that the dopants would diffuse through the active region, the temperature of the GaAs containing dopants was decreased. Therefore the intrinsic device had 50 nm GaAs spacers, of which 35 nm were grown at elevated temperatures, and as shown in chapter 3, this results in the GaAs being successfully re-planarised resulting in enhanced device performance. However the two doped samples (which also had 50 nm thick spacer layers) only had 20 nm grown at a higher temperature. This could have lead to lower quality GaAs spacer layers, with a higher concentration of defects, resulting in an increased non-radiative current. Such a process would be governed by the thickness and temperature of the

GaAs layers and therefore would be independent of the level of the doping, which is consistent with Figure 5.13.

5.5 Additional Samples

To allow further study on the role of p dopants in InAs quantum dot samples and validate the results presented in the previous sections of this chapter, two further structures were grown. The structures were largely identical to the ones discussed previously, with the only differences being that 7 DWELL layers were used this time and the active region was now incorporated into an $Al_{0.45}Ga_{0.55}As$ waveguide cladding structure. The structures were nominally doped to a level of 0 or 18 acceptor ions per dot, where the acceptors were again Be and incorporated in the same way as before.

Again the modal absorption spectra were obtained to ensure that the electronic states were the same for each device, as before a reverse bias was required to allow the excess carriers to be extracted and the true absorption to be seen. Figure 5.15 shows the modal absorption for the two structures under reverse biases of 0.5 and 2 V for the intrinsic and doped structure respectively.

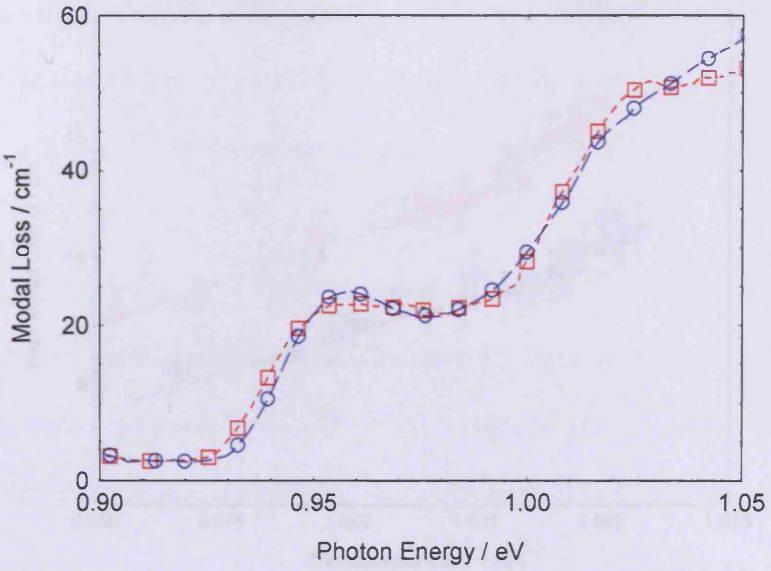

Figure 5.15: - Modal loss spectra for the undoped and p x 18 doped samples under reverse biases of 0.5 and 2 V respectively.

As seen previously the inclusion of dopants has not resulted in any change in the dot states or of the internal waveguide loss, α_i, of 2 ± 2 cm^{-1}. Again by comparing the area under the absorption curves at 0 V bias and once the absorption has saturated it is possible to determine the percentage of states occupied by excess holes. This yields values of 4 % and 19 % for the undoped and 18 p-dopant sample, which agree well with the values in Table 5.2 for the undoped and 15 p-dopant samples. Again this is a low percentage due to the influence of the wetting layer states. These results show that samples can be reliably and repeatable grown to a given level of doping.

As with the previous samples the modal gain was also measured, allowing the peak gain to be plotted as a function of both the transparency point and of current density.

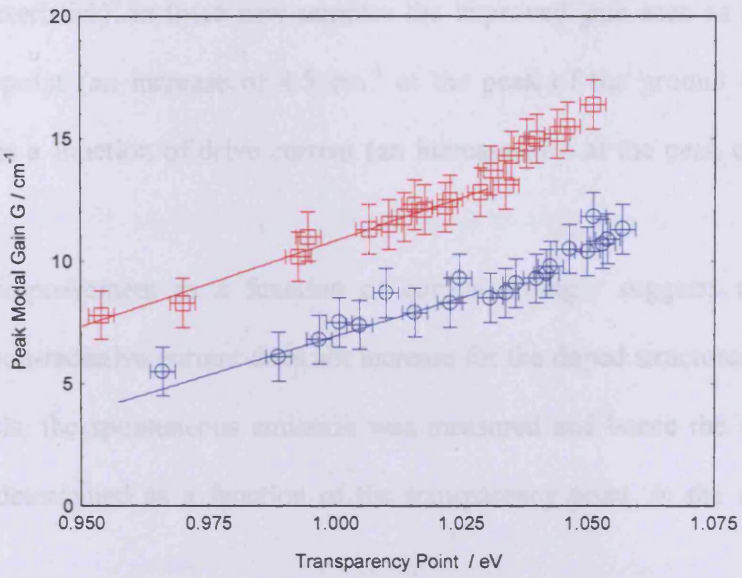

Figure 5.16: - Peak modal gain as function of transparency point for the undoped (circles) and P X 18 dopants (squares) samples.

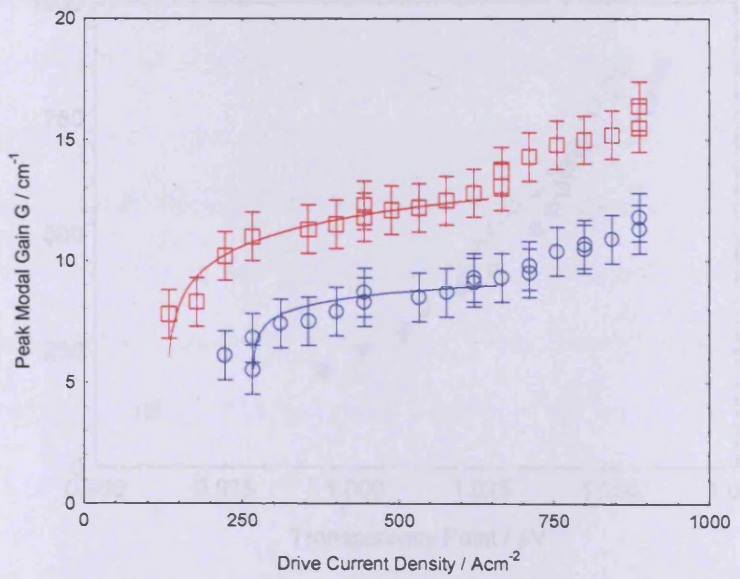

Figure 5.17: - Peak modal gain as a function of the drive current density for the undoped (circles) and P X 18 dopants (squares) samples.

Figure 5.16 shows the same behaviour as seen previously (Figure 5.8), with the doped structure always exhibiting an increased gain when compared to the undoped device. However Figure 5.17 shows dramatically different behaviour to that expected from Figure 5.9 (in which the previous undoped and doped samples all showed very

similar characteristics). In these new samples the improved gain seen as a function of transparency point (an increase of 4.5 cm^{-1} at the peak of the ground state) is also clearly seen as a function of drive current (an increase of 4 at the peak of the ground state).

This improvement as a function of current strongly suggests that in these samples the non-radiative current does not increase for the doped structure. To validate this hypothesis, the spontaneous emission was measured and hence the non-radiative current was determined as a function of the transparency point, in the same way as before.

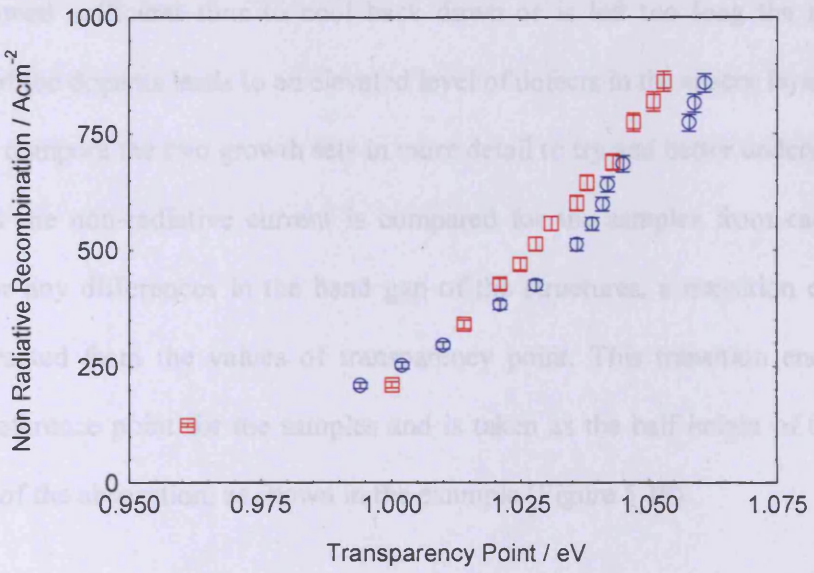

Figure 5.18: - Non-Radiative current density as a function of the transparency point for the undoped (circles) and P X 18 doped (squares) sample.

As expected from Figure 5.17 the two samples have very similar amounts of non-radiative current, with only a very slight (~ 10 %) increase for the doped structure. Several interesting points are raised by this result, as discussed above several groups have previously suggested Auger recombination as the cause of additional non-radiative

recombination in p doped structures [77,103,104]. In conjunction with the previous arguments (section 1.4) this seems even less likely with this result, as Auger is an intrinsic process and would always be present in doped samples. The same reasoning also applies to the idea that the leakage of holes leads to an increased non-radiative rate.

The most likely cause of the extra non-radiative current seen in section 1.4 was an increased number of defects in the GaAs spacer due to the decreased thickness at high temperature. However if this was the cause the same effect should also be seen here as the temperature was again decreased for the Be containing regions. It seems likely that the origin of the additional non-radiative process is exceptionally sensitive to the initial conditions when the dopants are included. It may be the case that if the GaAs is not allowed sufficient time to cool back down or is left too long the subsequent inclusion of the dopants leads to an elevated level of defects in the spacer layer.

To compare the two growth sets in more detail to try and better understand these differences the non-radiative current is compared for the samples from each set. To account for any differences in the band gap of the structures, a transition energy has been subtracted from the values of transparency point. This transition energy is an arbitrary reference point for the samples and is taken as the half height of the ground state peak of the absorption, as shown in the example (Figure 5.19).

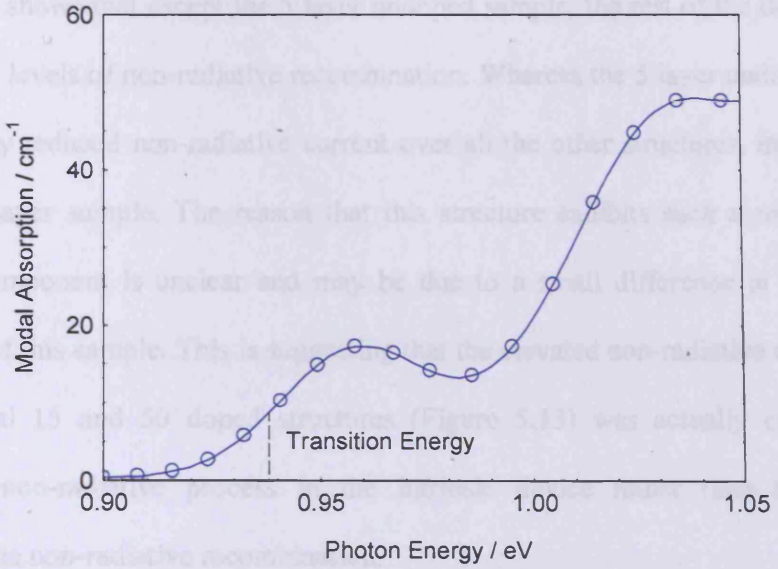

Figure 5.19: - Example modal absorption spectra for the 7 layer undoped sample.

By taking account of any change in the band gap between the two growth sets, it is possible to determine the non-radiative current at the same injection level for each device. The non-radiative current has also been re plotted as the current per layer to enable a direct comparison between the growth sets.

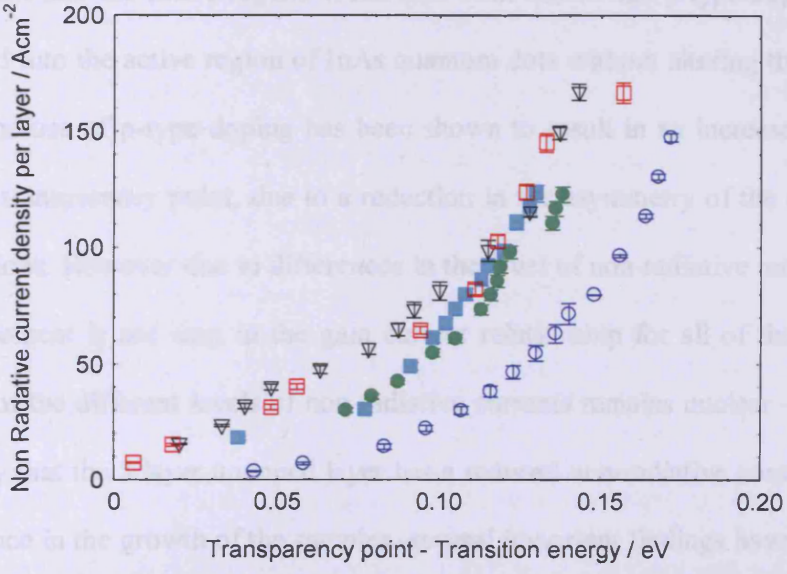

Figure 5.20: - Non-Radiative current as a function of transparency point minus transition energy for the 5 layer un doped sample (open circles), 5 layer p X 15 dopants (open squares), 5 layer p X 50 dopants (open triangles), 7 layer un doped (closed circles) and the 7 layer p X 18 dopants (closed squares) samples.

This shows that except the 5 layer undoped sample, the rest of the devices have very similar levels of non-radiative recombination. Whereas the 5 layer undoped device has a greatly reduced non-radiative current over all the other structures, including the intrinsic 7 layer sample. The reason that this structure exhibits such a reduced non-radiative component is unclear and may be due to a small difference in the growth conditions of this sample. This is suggesting that the elevated non-radiative current seen in the initial 15 and 50 doped structures (Figure 5.13) was actually caused by a decreasing non-radiative process in the intrinsic device rather than the dopants increasing the non-radiative recombination.

5.6 Conclusions

This chapter has studied the effects of incorporating modulation doping on InAs quantum dot structures. It has shown that the use of n-type doping leads to a change in the dot size and distribution. This effect is most likely caused by the interdiffusion of the Si dopants into the active region. It has also been shown that p-type dopants can be incorporated into the active region of InAs quantum dots without altering the growth of the dots. The use of p-type doping has been shown to result in an increased gain as a function of transparency point, due to a reduction in the asymmetry of the quasi-Fermi levels positions. However due to differences in the level of non-radiative recombination this improvement is not seen in the gain current relationship for all of the structures. The origin of the different levels of non-radiative currents remains unclear - although it seems likely that the 5 layer undoped layer has a reduced non-radiative component, due to a difference in the growth of the samples -several important findings have been made in this work. Although there have been many studies on p-doped quantum dot studies, these have relied on measurements of the threshold current of laser structures [100,103,104,108]. This results in the contrasting effects on the modal gain and the non-

radiative current being combined leading to conflicting reports on the effects of incorporating the dopants. By studying the material properties it has been possible to separate the effects of the gain and the recombination currents. This work has shown that the presence of p-type dopants leads to an increase in the available modal gain at a fixed injection level (Figure 5.9 and Figure 5.16) as initially predicted [91,95]. By also studying the non-radiative recombination it has been shown that the overall level of non-radiative current can be increased in doped samples. It is therefore the combination of these two effects that gives rise to the differing behaviour seen in threshold current measurements. The following chapters will go on to discuss the temperature performance of the undoped and doped structures.

This chapter has studied the effects of incorporating modulation doping on InAs quantum dot structures. It has shown that the use of n-type doping leads to a change in the dot size and distribution. This effect is most likely caused by the interdiffusion of the Si dopants into the active region. It has also been shown that p-type dopants can be incorporated into the active region of InAs quantum dots without altering the growth of the dots. The use of p-type doping has been shown to result in an increased gain as a function of transparency point. However due to differences in the level of non-radiative recombination this improvement is not seen in the gain current relationship for all of the structures. The origin of the different levels of non-radiative currents remains unclear - although it seems likely that the 5 layer undoped layer has a reduced non-radiative component, due to a difference in the growth of the samples -several important findings have been made in this work. Although there have been many studies on p-doped quantum dot studies, these have relied on measurements of the threshold current of laser structures [100,103,104,108]. This results in the contrasting effects on the modal gain and the non-radiative current being combined leading to conflicting reports on the effects of

incorporating the dopants. By studying the material properties it has been possible to separate the effects of the gain and the recombination currents. This work has shown that the presence of p-type dopants leads to an increase in the available modal gain at a fixed injection level (Figure 5.8 and Figure 5.15) as initially predicted [91,95]. By also studying the non-radiative recombination it has been shown that the overall level of non-radiative current can be increased in doped samples. It is therefore the combination of these two effects that gives rise to the differing behaviour seen in threshold current measurements. The following chapters will go on to discuss the temperature performance of the undoped and doped structures.

6. The temperature dependence of p-doped quantum dot lasers

6.1 Introduction

As discussed previously an early expectation of p-type modulation doped quantum dot structures was a temperature insensitive threshold current[105]. This performance has been reported by several groups [77,97,100,109], with some even showing a decreasing threshold with increasing temperature [98,103]around room temperature. Recently several authors have attributed this behaviour to the temperature dependence of the Auger recombination process in doped structures [77,103,104], although the particulars of the explanation differed in each case. In the first of these Fathpour et al.[77] modelled temperature insensitive threshold data by considering the contributions to the current due to recombination in the dots, wetting layer and barrier/waveguide regions; they also considered Auger recombination in the dots. It had previously been argued that the temperature dependence of electron-hole scattering (where an excited state electron scatters from holes in the ground state) decreases with an increasing temperature[110,111]. This results in the Auger recombination behaving in the same way and this decrease counteracts the increased recombination in the barrier/waveguide regions as the temperature is increased, leading to a temperature invariant threshold current. Marko et al.[103] explained the same phenomena by considering a thermal re-distribution of carriers. In this paper it was claimed that p-doped structures have an increased Auger recombination due to the large built-in hole concentration and that the Auger recombination increases with temperature. It was also postulated that in p-doped structures carriers go from a random to a thermal population over the temperature range

160-280 K. The reason for this high temperature re-distribution (compared with intrinsic quantum dot structures) was attributed to the increased confinement of electrons due to electrostatic attraction with the holes. Such a carrier re-distribution would cause the threshold current to decrease as the temperature is increased and this interplay with the increasing Auger rate leads to the observed threshold performance. Mokkapati et al.[104] modelled the gain and recombination rates in p-doped quantum dots. Their model explained the threshold performance by considering that an increased gain in doped devices allow lasing at lower transparencies, but that this is offset by increased Auger recombination due to the excess hole concentration. Although each of these models showed consistency with experimental data none considered the effects of leakage and defect related recombination. Also no measurements of how the gain alters with temperature were included in these works.

In this chapter threshold current as a function of temperature data is presented for the intrinsic, 15-p and 50-p dopant devices discussed previously (chapter 5). Data will then be presented from the segmented contact measurements (chapter 2) allowing the relative effects of the gain, radiative and non-radiative currents to be determined.

6.2 Threshold Current Measurements

Light current characteristics were recorded as a function of temperature (see chapter 2) for the un doped, 15-p and 50-p dopant structures. Measurements were performed on 2 mm long cavities with a 50 μm wide oxide stripe, multiple devices (four from each wafer) were tested for each structure and the average values are shown in Figure 6.1.

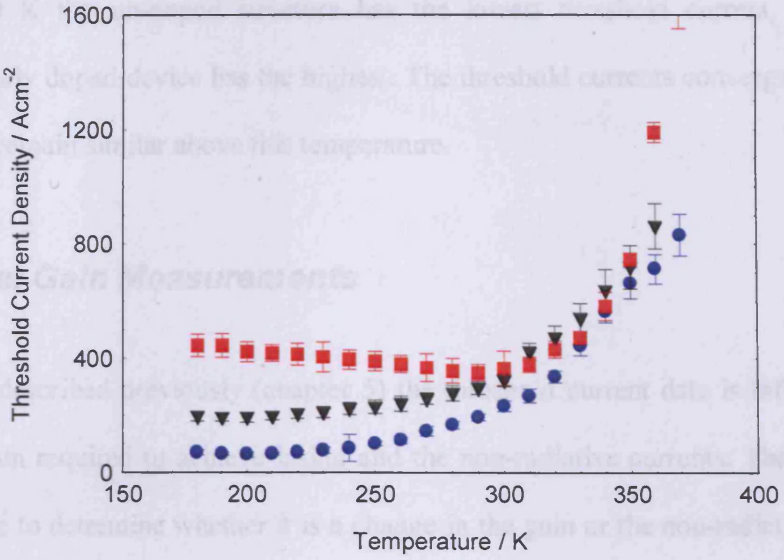

Figure 6.1: - Threshold current density as a function of temperature for a 2 mm long cavity for the un doped structure (circles), 15-p dopant sample (squares) and 50-p dopant sample (triangles).

The un doped device has a steadily increasing threshold current over the temperature range studied here, this is the same behaviour that has been observed previously in both quantum dot and quantum well lasers. Such behaviour occurs in quantum well and dot structures due to increasing amounts of non-radiative current and leakage as the temperature is increased; raising the total current required to achieve lasing. An increasing threshold current also occurs in quantum dot structures, due to the available modal gain at a fixed current decreasing with increasing temperature (see chapter 4) caused by carriers escaping to the wetting layer as the temperature is increased[32]. The highest doped structure has an approximately temperature independent threshold up to around 240 K when it then begins to increase. The 15-p dopant sample has a decreasing threshold current from 180 K to 280 K, before it begins to increase again. This decreasing threshold behaviour has been observed previously [77,103], although the origin is still a matter of debate.

Below 300 K the un-doped structure has the lowest threshold current, while the intermediately doped device has the highest. The threshold currents converge at around 300 K and remain similar above this temperature.

6.3 Modal Gain Measurements

As described previously (chapter 5) the threshold current data is influenced by both the gain required to achieve lasing and the non-radiative currents. Therefore it is not possible to determine whether it is a change in the gain or the non-radiative process as a function of temperature which gives rise to the different behaviour seen in each structure (Figure 6.1) from the threshold current data alone.

To differentiate between these two factors, segmented contact experiments have been performed on the three devices at various temperatures, allowing the relative contributions of the gain, radiative and non-radiative recombination to be determined. The peak modal gain has been determined for each structure at various temperatures; gain spectra for a constant ground state peak net modal gain of 6 cm^{-1} at temperatures of 250, 300 and 375 K are plotted in Figure 6.2, Figure 6.3 and Figure 6.4 for the intrinsic, 15 and 50-p dopant structures respectively.

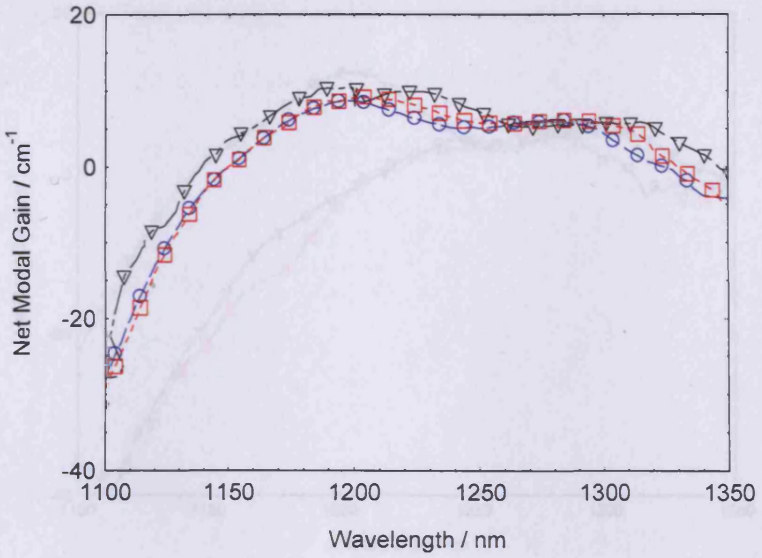

Figure 6.2: - Modal gain spectra for the un-doped structure at temperatures of 250 (circles), 300 (squares) and 375 K (triangles).

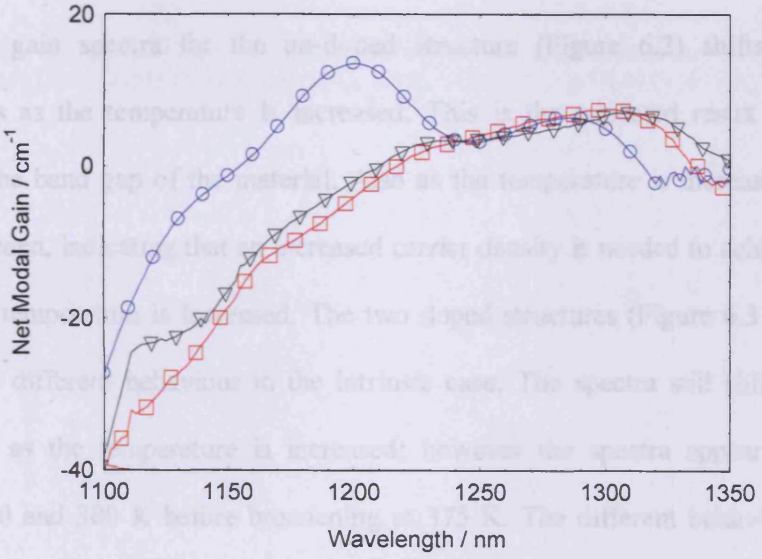

Figure 6.3: - Modal gain spectra for the 15-dopant structure at temperatures of 250 (circles), 300 (squares) and 375 K (triangles).

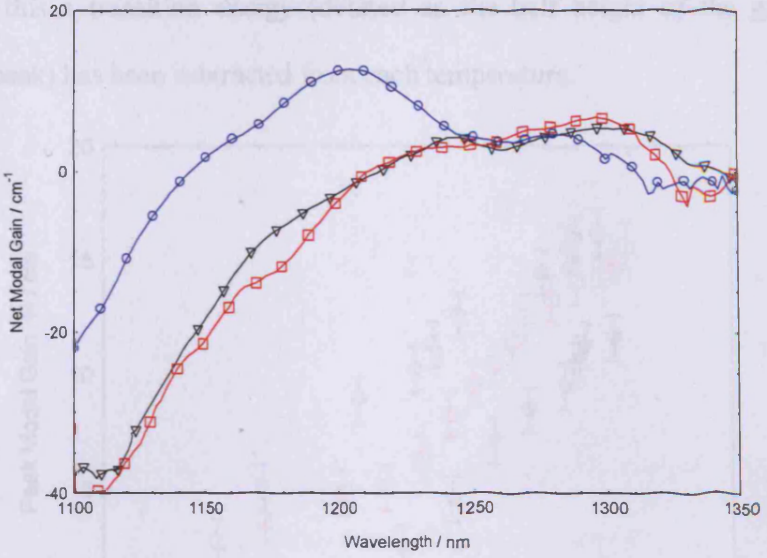

Figure 6.4: - Modal gain spectra for the 50-dopant structure at temperatures of 250 (circles), 300 (squares) and 375 K (triangles).

The gain spectra for the un-doped structure (Figure 6.2) shifts to longer wavelengths as the temperature is increased. This is the expected result due to the change in the band gap of the material. Also as the temperature is increased the gain spectra broaden, indicating that an increased carrier density is needed to achieve a fixed gain as the temperature is increased. The two doped structures (Figure 6.3 and Figure 6.4) exhibit different behaviour to the intrinsic case. The spectra still shift to longer wavelength as the temperature is increased; however the spectra appear to narrow between 250 and 300 K before broadening at 375 K. The different behaviour for the doped and intrinsic samples suggests that the carrier distributions behave in very different ways in each sample. To look at this in more detail, the peak gain has been determined as a function of the transparency point at each temperature for each device. The transparency point is related to the injection level required to achieve a given level of gain and as such allows the gain to be studied as a function of the injection. However as mentioned previously the band gap also changes with temperature, therefore to take

account of this a transition energy (defined as the half height of the ground state absorption peak) has been subtracted from each temperature.

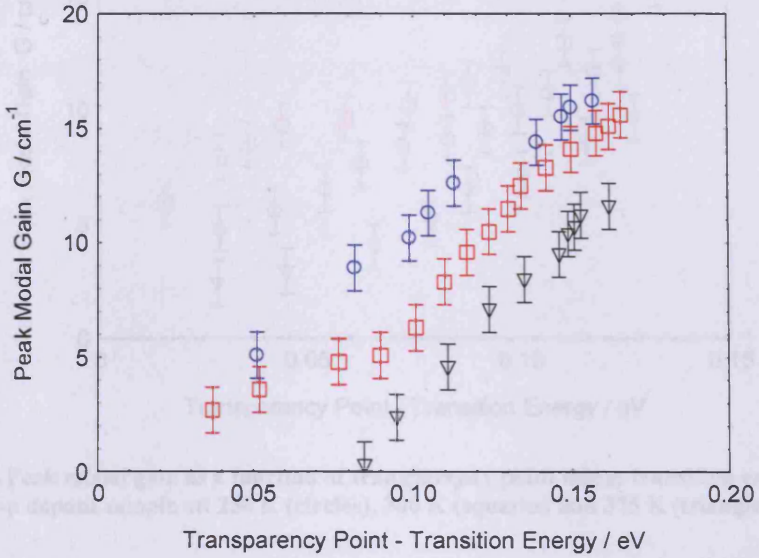

Figure 6.5: - Peak modal gain as a function of transparency point - transition energy for the intrinsic sample at: 250 K (circles), 300 K (squares) and 375 K (triangles).

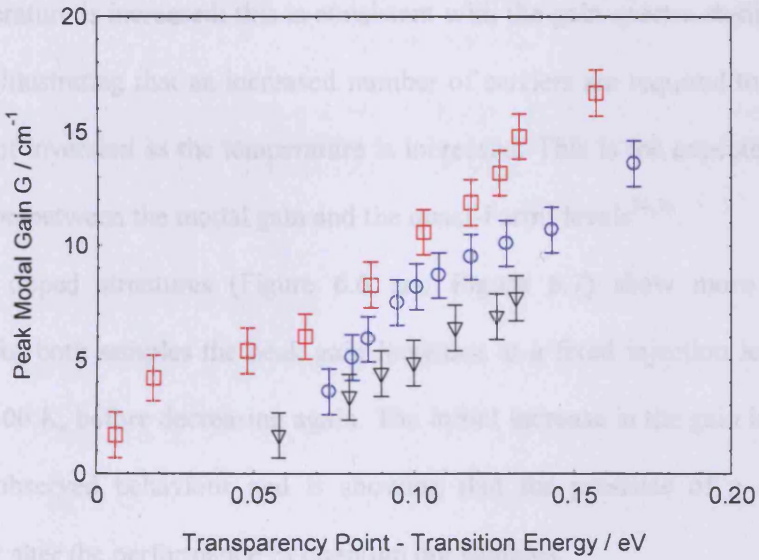

Figure 6.6: - Peak modal gain as a function of transparency point minus transition energy for the 15-p dopant sample at: 250 K (circles), 300 K (squares) and 375 K (triangles).

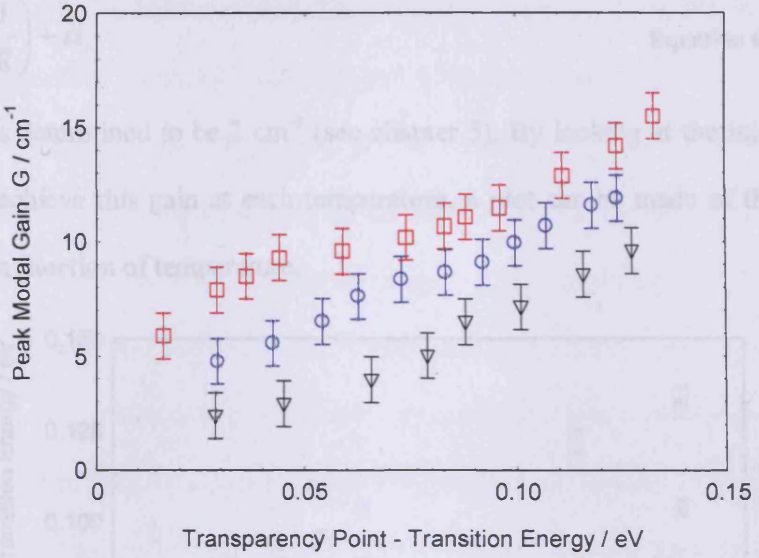

Figure 6.7: - Peak modal gain as a function of transparency point minus transition energy for the 50-p dopant sample at: 250 K (circles), 300 K (squares) and 375 K (triangles).

The intrinsic device (Figure 6.5) has a decreasing gain for a fixed injection level as the temperature is increased; this is consistent with the gain spectra studied in Figure 6.2. This is illustrating that an increased number of carriers are required to achieve the same level of inversion as the temperature is increased. This is the expected result due to the relation between the modal gain and the quasi-Fermi levels[24,36].

The doped structures (Figure 6.6 and Figure 6.7) show more unexpected behaviour, for both samples the peak gain increases at a fixed injection level between 250 K and 300 K, before decreasing again. The initial increase in the gain is contrary to previously observed behaviour and is showing that the presence of p dopants can significantly alter the performance of quantum dot samples.

To look at how the injection level (transparency point minus transition energy) changes as a function of temperature for the lasers studied in Figure 6.1, the modal gain, G, required to achieve lasing was calculated to be 8 cm^{-1} using,

$$G = \frac{1}{L}\ln\left(\frac{1}{R}\right) + \alpha_i \qquad \textbf{Equation 6.1}$$

where α_i was determined to be 2 cm^{-1} (see chapter 5). By looking at the injection level required to achieve this gain at each temperature, a plot can be made of the changing injection as a function of temperature.

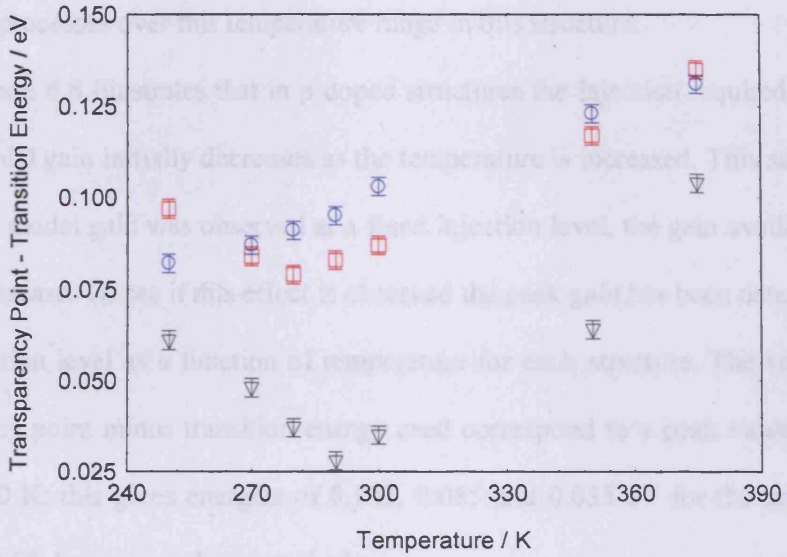

Figure 6.8: - The transparency point minus transition energy required to achieve a peak modal gain of 8 cm^{-1} as a function of temperature for the un doped (circles), 15-p dopant (squares) and 50-p dopant (triangles) samples.

The un-doped device requires a higher injection level as the temperature is increased to maintain the same gain; this is the expected behaviour from considering the relationship between the gain and the occupation probabilities (assuming a thermal distribution of carriers). The doped structures exhibit quite different behaviour, the injection level required to achieve the same peak modal gain initially decreases, reaching minima at around 280 and 290 K for the 15 and 50-p doped samples respectively. Above this temperature the injection level then increases to maintain the same gain, in the same way as for the un-doped structure. The minimum occurring at slightly different temperatures in the two structures, suggests that this phenomenon is

sensitive to the doping concentration. The minimum temperature of 280 K agrees well with the minimum in the threshed data for the 15-p dopant sample. The minima appear to be more pronounced for the higher doped structure suggesting that the process becomes more severe at higher doping levels. However no minimum is detected in the threshold data for the 50-p dopant device (Figure 6.1), suggesting that there must be additional processes over this temperature range in this structure.

Figure 6.8 illustrates that in p doped structures the injection required to achieve a fixed modal gain initially decreases as the temperature is increased. This suggests that if the peak modal gain was observed at a fixed injection level, the gain available should initially increase. To see if this effect is observed the peak gain has been determined at a fixed injection level as a function of temperature for each structure. The values of the transparency point minus transition energy used correspond to a peak modal gain of 8 cm^{-1} at 300 K; this gives energies of 0.103, 0.085 and 0.035 eV for the un-doped, 15 dopant and 50 dopant sample respectively.

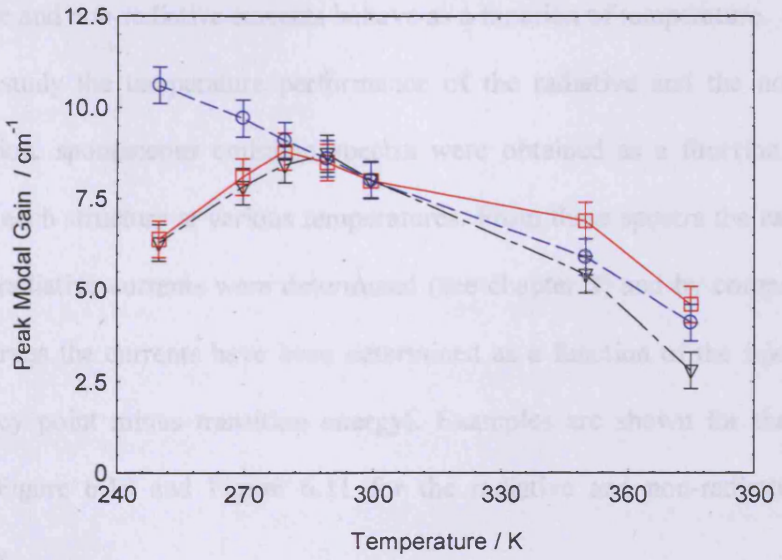

Figure 6.9: - Peak modal gain as a function of temperature for a fixed transparency point minus transition energy of: 0.103 eV for the un doped (circles), 0.085 eV for the 15-p dopant (squares) and 0.035 eV for the 50-p dopant (triangles) samples.

This shows the behaviour predicted from Figure 6.8, with the peak gain increasing at a fixed injection for the doped structures and reaching maximum values of 9 and 9.5 cm^{-1} at approximately 280 and 290 K for the 15 and 50-doped structures respectively. The un-doped device exhibits a steadily decreasing gain from 250 to 375 K, as expected from Figure 6.8. The two doped structures exhibit relatively similar behaviour up to approximately 300 K, this is in contrast to the previous plot (Figure 6.8), in which the higher doped sample exhibited a much sharper minima.

6.4 Non-Radiative Current

The temperature dependence of the threshold current observed in Figure 6.1 and in previous studies [77,103,104] could be due to the temperature variation of the gain (as observed in the previous section) or to the change in recombination processes as a function of temperature as suggested previously. To determine the relative effect that these two processes have on the threshold current and hence fully understand the temperature dependence of p-doped quantum dot lasers it is necessary to determine how the radiative and non-radiative currents behave as a function of temperature.

To study the temperature performance of the radiative and the non-radiative recombination, spontaneous emission spectra were obtained as a function of current density for each structure at various temperatures. From these spectra the radiative and hence non-radiative currents were determined (see chapter 2) and by comparison with the gain curves the currents have been determined as a function of the injection level (transparency point minus transition energy). Examples are shown for the un-doped device in Figure 6.10 and Figure 6.11 for the radiative and non-radiative currents respectively.

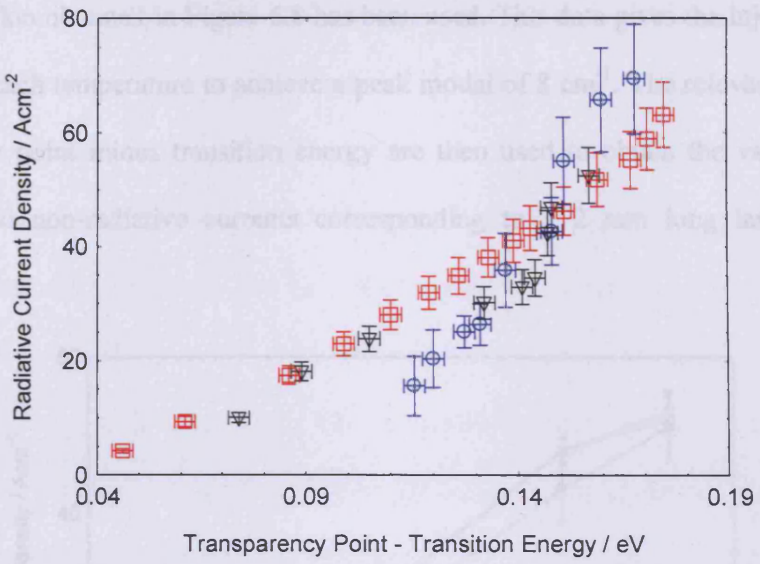

Figure 6.10: - Radiative current density as a function of the transparency point minus transition energy for the un doped device at 250 K (circles), 300 K (squares) and 375 K (triangles).

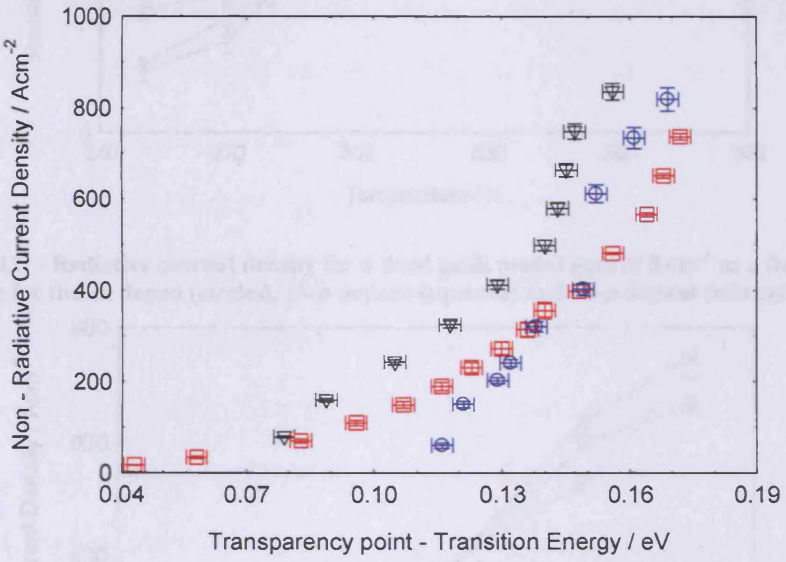

Figure 6.11: - Non-radiative current density as a function of the transparency point minus transition energy for the un doped device at 250 K (circles), 300 K (squares) and 375 K (triangles).

The radiative current is approximately constant over the temperature range studied for a given injection level whereas the non-radiative current (Figure 6.11) shows approximately the same non-radiative recombination for a fixed injection level at 250 and 300 K, but exhibits an increase in non-radiative current at higher temperatures. To study how the radiative non-radiative currents vary for the lasers studied in Figure 6.1

the information obtained in Figure 6.8 has been used. This data gives the injection level required at each temperature to achieve a peak modal of 8 cm^{-1}. The relevant values of transparency point minus transition energy are then used to obtain the values of the radiative and non-radiative currents corresponding to a 2 mm long laser at each temperature.

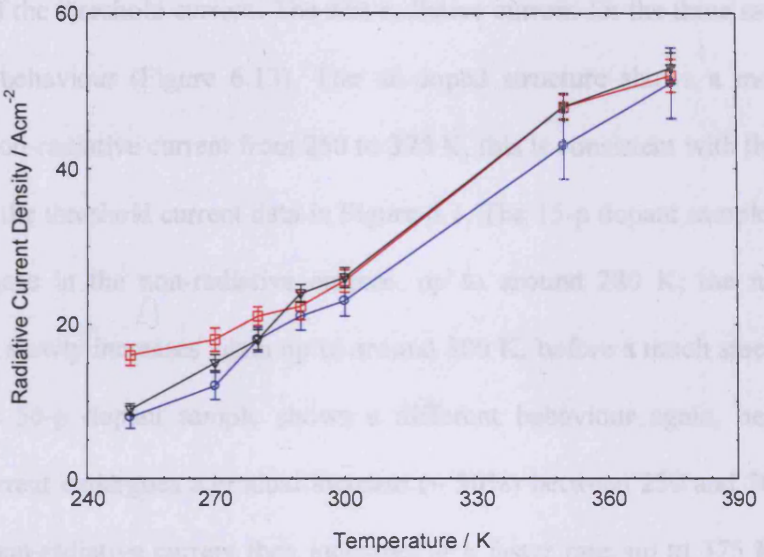

Figure 6.12: - Radiative current density for a fixed peak modal gain of 8 cm^{-1} as a function of temperature for the un doped (circles), 15-p dopant (squares) and 50-p dopant (triangles) samples.

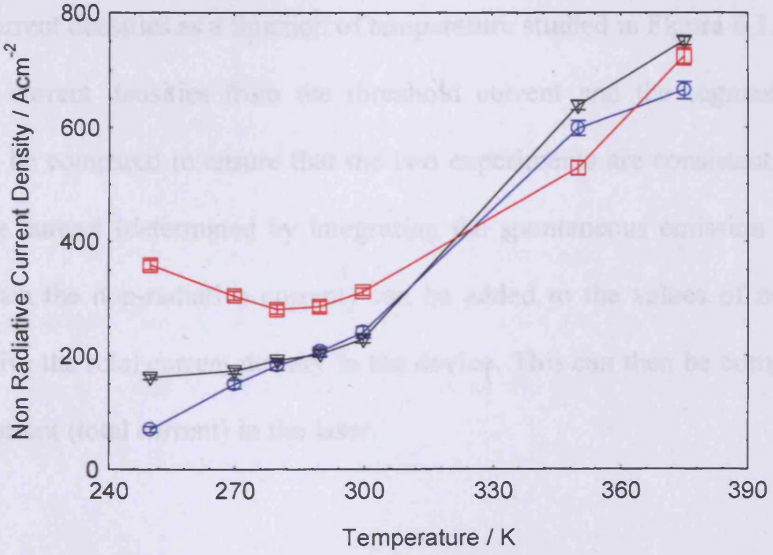

Figure 6.13: - Non-radiative current density for a fixed peak modal gain of 8 cm^{-1} as a function of temperature for the un doped (circles), 15-p dopant (squares) and 50-p dopant (triangles) samples.

The radiative current from all three samples is very similar, with a monotonically increasing radiative current. All three structures also exhibit very similar values of radiative current, which is dramatically less than the non-radiative contribution to the current (less than 10 % at all temperatures). These factors suggest that the radiative current does not have any significant influence on the temperature behaviour of the threshold current. The non-radiative current for the three samples show contrasting behaviour (Figure 6.13). The un-doped structure shows a monotonically increasing non-radiative current from 250 to 375 K, this is consistent with the behaviour observed in the threshold current data in Figure 6.1. The 15-p dopant sample exhibits an initial decrease in the non-radiative current, up to around 280 K; the non-radiative current then slowly increases again up to around 300 K, before a much steeper increase occurs. The 50-p dopant sample shows a different behaviour again, here the non-radiative current undergoes a gradual increase (~ 30%) between 250 and 300 K; above 300 K the non-radiative current then increases at a faster rate, up to 375 K. The three differing behaviours observed in Figure 6.13, each agree well with the shapes of the threshold current densities as a function of temperature studied in Figure 6.1.

The current densities from the threshold current and the segmented contact method can be compared to ensure that the two experiments are consistent. To do this the radiative current (determined by integrating the spontaneous emission spectra and used to obtain the non-radiative current) can be added to the values of non-radiative current to give the total current density in the device. This can then be compared to the threshold current (total current) in the laser.

	Radiative Current Density / Acm^{-2}	**Non-Radiative Current Density / Acm^{-2}**	**Total Current Density / Acm^{-2}**	**Threshold Current Density / Acm^{-2}**
Un doped				
250 K	12 ± 3	71 ± 4	**83 ± 4.5**	**93 ± 8**
300 K	23 ± 4	241 ± 13	**264 ± 13.1**	**290 ± 27**
350 K	52 ± 9	601 ± 25	**653 ± 26.2**	**645 ± 36**
15-p dopants				
250 K	16 ± 3	354 ± 18	**370 ± 18.3**	**385 ± 23**
300 K	24 ± 2	316 ± 12	**330 ± 12.6**	**339 ± 19**
350 K	48 ± 4	629 ± 27	**677 ± 27.1**	**577 ± 41**
50-p dopants				
250 K	9 ± 1	162 ± 10	**171 ± 10.2**	**214 ± 28**
300 K	26 ± 3	229 ± 13	**255 ± 13.4**	**293 ± 31**
350 K	48 ± 3	633 ± 25	**681 ± 25.1**	**697 ± 43**

Table 6.1: - Comparison of total current densities at a peak modal gain of 8 cm^{-1} and threshold current densities for 2 mm long lasers.

The information in Table 6.1 shows that the two experimental procedures give a reasonable agreement (less than 17% difference, apart from for the 50 dopant case at 250 K). This data provides strong evidence that using the segmented contact method is a feasible and accurate technique to evaluate the performance of laser devices at threshold.

The temperature behaviour observed in Figure 6.13 is the expected performance from the threshold current data (Figure 6.1), however it does not allow the origin of the changing non-radiative current to be determined. Either the changing injection level required to achieve a fixed gain (Figure 6.8) or a change in the non-radiative processes with temperature (as proposed previously[77,103]) could account for this behaviour. It is also conceivable that both of these factors have an effect and that the result observed (Figure 6.1 and Figure 6.13) is due to the combination of them.

To try and determine the relevant magnitudes of each of these effects the non-radiative current density has been determined for a fixed injection level as a function of temperature for the three samples. This has been achieved by plotting the non-radiative recombination for a fixed transparency point minus transition energy (Figure 6.14). The values correspond to the injection level required to achieve a gain of 8 cm^{-1} at 300 K (0.103, 0.085, and 0.035 eV for the un doped, 15-p dopant and 50-p dopant samples respectively). The associated non radiative current was then determined at each temperature for this fixed energy.

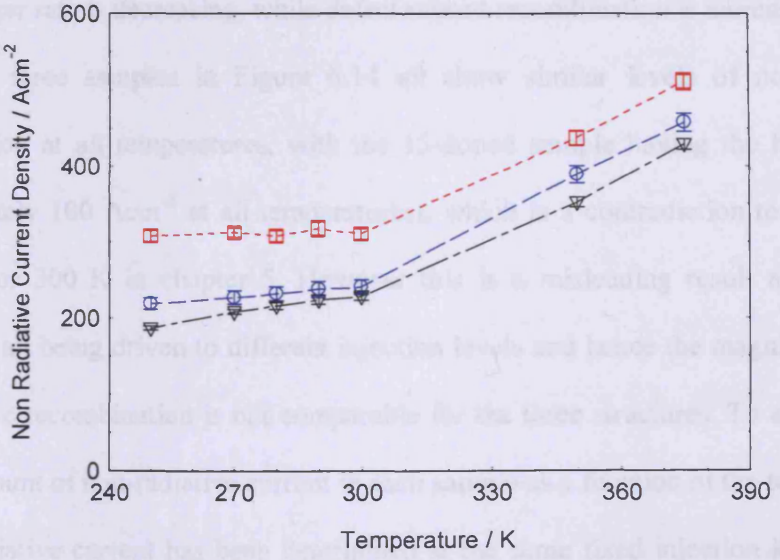

Figure 6.14: - Non-radiative current density as a function of temperature at fixed values of transparency point - transition energy of 0.103 eV for the un doped structure (circles), 0.085 eV for the 15-p dopant sample (squares) and 0.035 eV for the 50-p dopant sample (triangles).

The values of non-radiative current at 300 K in Figure 6.13 and Figure 6.14 are the same as they all correspond to threshold in a 2 mm long laser device. For the 15-p dopant device the non-radiative current is approximately constant up to 300 K after which it begins to increase. The constant region between 250 and 300 K indicates that if the structure was pumped to the same injection level there would be no significant change in the non-radiative current. Therefore the temperature behaviour observed in the threshold current data (Figure 6.1) is caused almost entirely by the changing injection level required to achieve a peak modal gain of 8 cm^{-1}.

The intrinsic and 50-p dopant device both show similar behaviour with a gradual increase (~ 12 % and 20 % respectively) in the non-radiative current between 250 and 290 K and then a sharper increase as the temperature is further increased. It has previously been postulated that the amount of Auger recombination decreases as the temperature is increased[77,110,111], however in these results the non-radiative recombination increases for increasing temperature. However in this work it is the total non-radiative recombination rate which has been determined, and therefore it is possible that the Auger rate is decreasing, while defect related recombination is increasing.

The three samples in Figure 6.14 all show similar levels of non-radiative recombination at all temperatures, with the 15-doped sample having the highest rate (approximately 100 Acm^{-2} at all temperatures), which is a contradiction to the results presented for 300 K in chapter 5. However this is a misleading result as the three devices are all being driven to different injection levels and hence the magnitude of the non-radiative recombination is not comparable for the three structures. To examine the relative amount of non-radiative current in each sample as a function of the temperature, the non-radiative current has been determined at the same fixed injection level (0.103 eV) for all three samples.

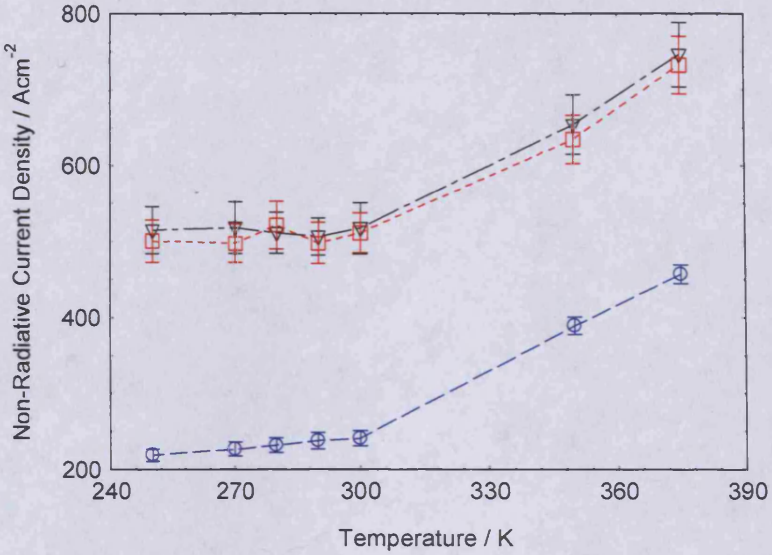

Figure 6.15: - Non-radiative current density as a function of temperature for a fixed transparency point minus transition energy of 0.103 eV for the un doped (circles), 15-p dopant (squares) and 50-p dopant (triangles) samples.

All the structures show similar behaviour to before (Figure 6.14) with both doped samples showing an approximately constant value between 250 and 300 K and then an increasing current at higher temperatures, while the intrinsic device shows a slowly increasing current at all temperatures. However the doped devices now exhibit a higher non-radiative current at all temperatures when compared to the intrinsic sample, with a small further increase for the highest doped structure. This result is consistent with the data presented in chapter 5 regarding the non-radiative current at 300 K

The differing threshold behaviour (Figure 6.1) for the two doped structures is mimicked in the variation of the non-radiative current with temperature for a fixed modal gain of 8 cm^{-1} (Figure 6.13). The non-radiative current at a fixed injection level (Figure 6.14) also shows a differing behaviour, with the lower doped sample showing an approximately constant non-radiative rate up to 300 K and the highest doped structure exhibiting an increasing non-radiative rate over the same temperature range. Whereas the injection level required to maintain a gain of 8 cm^{-1} has been shown to

initially decrease for both the doped structures (Figure 6.8). It is the combination of this decreasing injection level and changing non-radiative current that leads to the differing threshold performance.

For the 15-doped sample the injection level required decreases, while the non-radiative rate at a given injection level remains constant, hence resulting in a lower non-radiative current and therefore a reduced threshold current. For the 50-doped sample although the injection level again decreases, now the non-radiative current at a fixed injection increases. The combination of these two factors leads to an approximately constant threshold up to about 240 K, before a steady increase occurs. The reason for the differing behaviour of the non-radiative rates is unclear, although it seems most likely to be due to the vastly different injection levels required in the two samples.

6.5 Carrier Re-distribution

The reason for the variation in the injection level required to achieve a fixed modal gain (Figure 6.8) is also unclear from the work presented so far and shall now be discussed in some detail.

It has previously been suggested that in p-doped quantum dots the form of the carrier distribution changes as a function of temperature[103,112]. It has been claimed that the carriers initially occupy the dots under random occupation and as the temperature is increased this changes into a thermal distribution of carriers. If the dots were initially filled by random population, all dot states would have an equal probability of being filled by carriers, resulting in relatively wide spectra. As the population begins to become thermal, the lower energy states would be filled preferentially, resulting in narrower spectra. This therefore would lead to a reducing injection level (to maintain a fixed gain) as the temperature is increased, as was observed experimentally (Figure 6.8).

As the temperature is further increased a thermal distribution would involve more high energy states to maintain the same injection, resulting in the spectra broadening again. To see if this is the origin of the changing injection level observed in these samples, the width of the spontaneous emission spectra were measured at fixed values of transparency point minus transition energy at each temperature. To ensure all the spontaneous emission was collected (including that over the wetting layer region) the spontaneous emission was measured from the top of the device (see chapter 4).

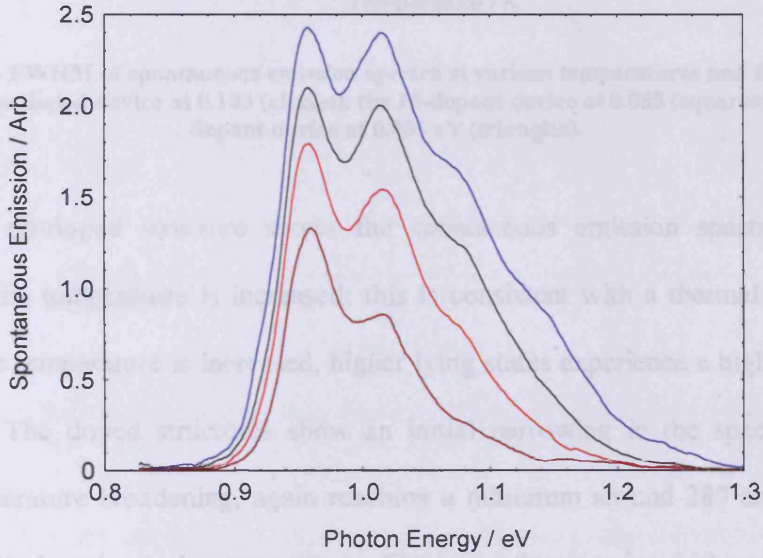

Figure 6.16: - Example spontaneous emission spectra for the 15-dopant sample at 300 K and current densities of 222, 444, 622 and 800 Acm^{-2}.

The widths of the spectra were then determined from the full-width-at-half-maximum (FWHM). Transparency point minus transition energies of 0.103, 0.085 and 0.035 eV were used for the un-doped, 15-dopant and 50-dopant structures respectively, corresponding to the injection required for lasing in a 2 mm long cavity at 300 K.

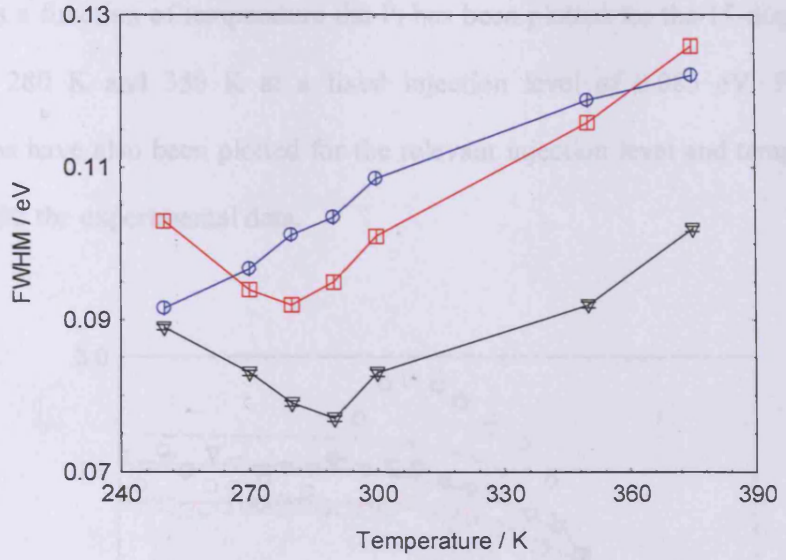

Figure 6.17:- FWHM of spontaneous emission spectra at various temperatures and fixed injection levels; the un doped device at 0.103 (circles), the 15-dopant device at 0.085 (squares) and the 50-dopant device at 0.035 eV (triangles).

The un-doped structure shows the spontaneous emission spectra becoming broader as the temperature is increased; this is consistent with a thermal distribution, where as the temperature is increased, higher lying states experience a higher degree of occupancy. The doped structures show an initial narrowing in the spectra before a higher temperature broadening, again reaching a minimum around 280 and 290 K for the 15 and 50-doped samples respectively. The initial decrease in width suggests that to begin with the dots are randomly populated and as the temperature is increased they become thermally populated, giving a thermal distribution. The subsequent increase is then due to thermal broadening as observed in the un-doped structure.

To further investigate the changing shape of the spontaneous emission spectra and to try and determine if the effects seen in Figure 6.17 are due to a changing carrier distribution the P_f has been studied. As described in chapter 2 if the P_f expression (given by the ratio of the gain to the spontaneous emission) can be fitted with Fermi-Dirac statistics then the carriers are thermally distributed. To see how the carrier population is

changing as a function of temperature the P_f has been plotted for the 15-dopant sample at 250 K, 280 K and 350 K at a fixed injection level of 0.085 eV. Fermi-Dirac relationships have also been plotted for the relevant injection level and temperatures to compare with the experimental data.

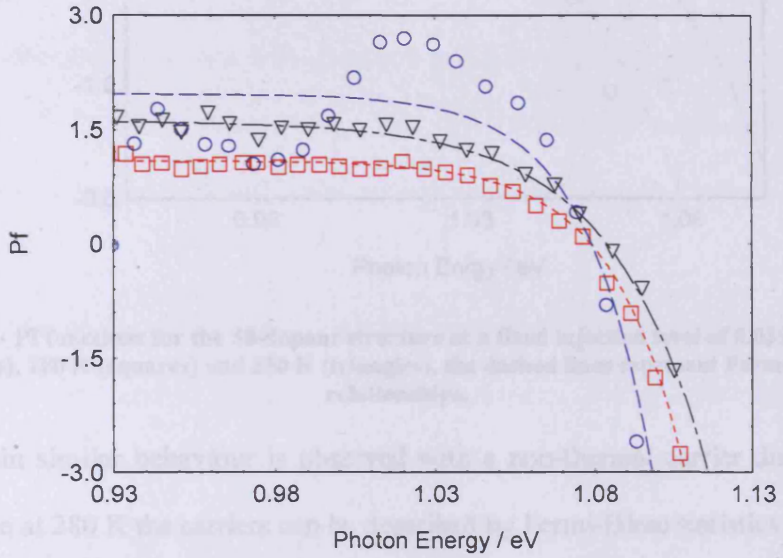

Figure 6.18: - P_f functions for the 15-dopant structure at a fixed injection level of 0.085 eV at 250 K (circles), 280 K (squares) and 350 K (triangles), the dashed lines represent Fermi-Dirac relationships.

At 250 K the measured P_f is drastically different to that expected from Fermi-Dirac statistics (dashed line); this is showing that at this temperature the carriers are not in a thermal distribution. At 280 K the experimental data and the Fermi-Dirac distribution show a good agreement indicating that by this temperature the carriers are distributed thermally in the structure. At 350 K, the carriers still appear to be distributed thermally, although the agreement between the experimental points and the theory does not seem so good here. This poorer agreement is most probably due to the reduced signal (and hence increased signal-to-noise ratio) at higher temperatures. The same analysis has also been performed on the highest doped sample for a fixed injection level of 0.035 eV.

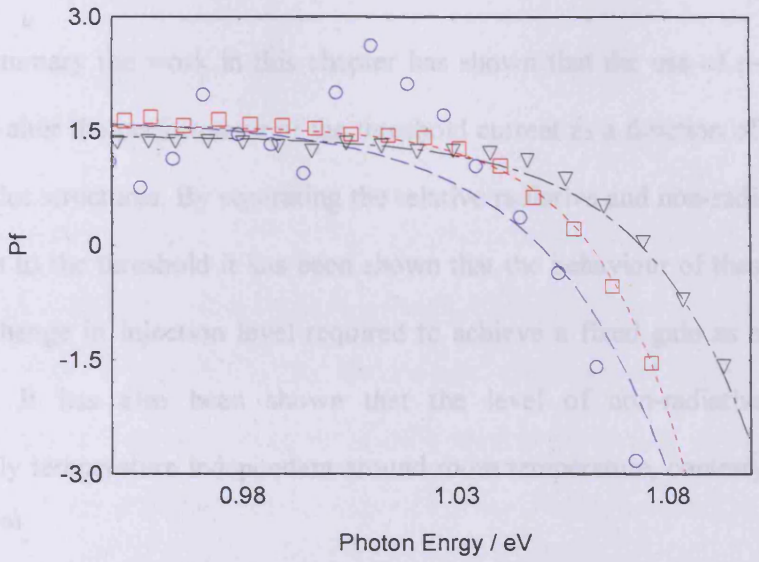

Figure 6.19: - Pf functions for the 50-dopant structure at a fixed injection level of 0.035 eV at 250 K (circles), 280 K (squares) and 350 K (triangles), the dashed lines represent Fermi-Dirac relationships.

Again similar behaviour is observed with a non-thermal carrier distribution at 250 K. Once at 280 K the carriers can be described by Fermi-Dirac statistics and as such are shown to be thermally distributed. These two graphs support the conclusions drawn from Figure 6.17 that as the temperature is increased the carriers go from a random to a thermal population.

The slightly different temperatures at which the two samples begin to be described by a thermal distribution, indicates that as the doping level is increased the temperature to achieve a thermal distribution must also be increased. This seems a reasonable conclusion, because as the doping concentration is increased there are a larger number of carriers that need to be thermally distributed.

6.6 Conclusions

In summary the work in this chapter has shown that the use of p-dopants can significantly alter the performance of the threshold current as a function of temperature in quantum dot structures. By separating the relative radiative and non-radiative current contributions to the threshold it has been shown that the behaviour of these samples is due to the change in injection level required to achieve a fixed gain as a function of temperature. It has also been shown that the level of non-radiative current is approximately temperature independent around room temperature, contrary to previous studies[77,103,104].

The change in injection level required to maintain a fixed gain has been shown to be due to the carriers going from a random to a thermal distribution as the temperature is increased. Differing threshold current performance has been observed in the two doped structures and it seems likely that this is due to a trade off in the redistribution of the carriers and the non-radiative recombination rates.

7. Radiative Lifetimes and the Einstein Relations

7.1 Introduction

The Einstein relations [23,24,113,114] are used to describe the interaction of electrons and photons in a system of discrete energy levels when in thermal equilibrium. As was shown in chapter 1 (equation 1.35) the average spontaneous lifetime of a single quantum dot can be expressed in terms of the optical cross section. In this chapter the optical cross section is determined for each of the samples investigated in the previous chapters. This information is used to determine and compare the radiative lifetime of the dots in each of the samples studied.

7.2 Radiative Lifetime Calculations

The segmented contact method can be used to determine the modal absorption spectra (see chapter 2). If the absorption from each state can be separated, the relative cross section can be determined from equation 18 allowing the radiative lifetime for that state to be calculated. The absorption due to different transitions can be determined by fitting Gaussian functions to the spectra representing the various transitions within the dots (see chapters 4 and 5). Therefore the Gaussian corresponding to the ground state transition can be integrated to give the optical cross section of a single dot and hence allow the radiative lifetime to be determined.

In all of the samples studied in this work there has been strong evidence that the dots form in a bi-modal distribution [59,115] (see chapters 4 and 5). As such the Gaussians from two different dot sizes have been fitted to each of the loss spectra evaluated in this

work. This therefore allows the radiative lifetime of both large and small dots to be calculated, example absorption and Gaussian fits are shown in Figure 7.1 for the HGTSL sample studied in chapter 4.

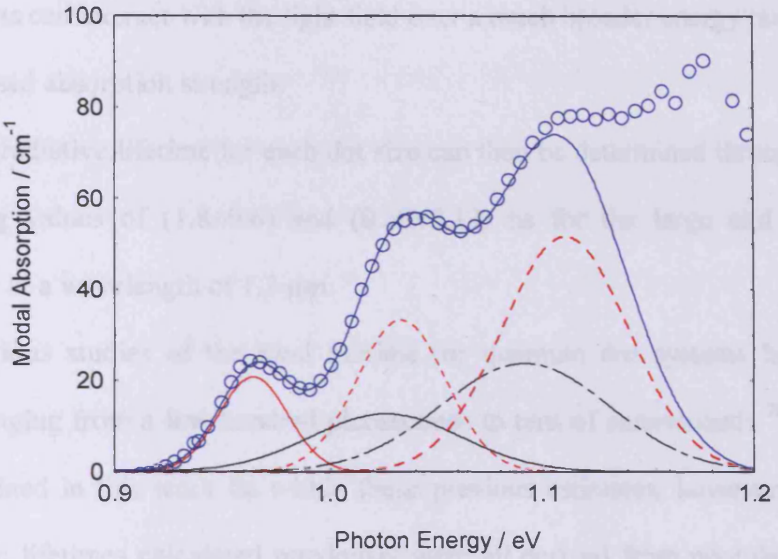

Figure 7.1: - Modal Absorption Spectrum and fitted Gaussians corresponding to a bimodal distribution of dots for the HGTSL sample.

The ground state of the larger dots is described by a Gaussian distribution centred at 0.964 eV, while the smaller dots are characterised by a Gaussian centred at 1.025 eV. Therefore by integrating the area under these Gaussians it is possible to determine the optical cross section of each dot size using equation 1.20. The optical cross section is determined for a single dot and as such the number of dots of each size has to be determined. To achieve this AFM data [59] from similar uncapped samples have been used, these give a dot density of 3.2 X 10^{10} cm^{-2} for the larger dots in each layer and a density of 9 X 10^{9} cm^{-2} for the smaller dots. This gives values for the integrated ground state optical cross section of (2.39±0.75) X 10^{-16} $eVcm^2$ and (1.15±0.31) X 10^{-15} $eVcm^2$ for the large and the small dots respectively. These values are not dissimilar to a

previous measurement of the integrated optical cross section for InAs quantum dots of 4.3 X 10^{-16} $eVcm^{-2}$ determined by Osborne, et al.[35]. The increased cross section for the smaller dots, seems to be most likely due to a broader size distribution (as shown by the AFM data in chapter 3 and the Gaussian fittings in chapters 3 and 4) as such the smaller subset of dots can interact with the light field over a much broader energy range, leading to an increased absorption strength.

The radiative lifetime for each dot size can then be determined through equation 1.35, giving values of (1.8±0.6) and (0.38±0.12) ns for the large and small dots respectively at a wavelength of 1.3 μm.

Previous studies of the total lifetime for quantum dot systems have yielded lifetimes ranging from a few hundred picoseconds to tens of nanoseconds [76,116-120]. The values obtained in this work lie within these previous estimates, however it is worth stressing the lifetimes calculated previously were all derived from photoluminescence experiments. As such these values actually give total lifetimes for the ensemble of dots being studied and will be affected by carrier relaxations and non-radiative processes. However the lifetime obtained in this work is the average spontaneous lifetime per dot and gives the time taken for an exciton to recombine in one dot. As such the two lifetimes are not directly comparable and should not be expected to yield the same answer. Lifetime measurements have also been performed previously on single quantum dots via the use of micro photoluminescence techniques, yielding values to the order of a nanosecond [121], again in reasonable agreement with the values determined here.

The lifetime of an ensemble of dots would generally be considered the more useful lifetime to measure, as it is this lifetime that will influence the performance of a quantum dot laser. However the average lifetime per dot is still a useful parameter to measure as it provides additional information about the system. Knowledge of the

average lifetime can allow it to be seen whether it is this lifetime that limits the lifetime of the ensemble or if non-radiative processes / carrier transport are the limiting factors.

The optical cross section and hence the radiative lifetime can be determined for all the other structures studied in this work to see how they are influenced by different factors. To do this the dot density used is the same as above [59] and it is assumed that the dot density remains constant in each layer, and so it was not possible to determine the radiative lifetime for the other samples studied in chapter 4 as altering the spacer layer growth has been shown to alter the dot density [59]. The values for the optical cross section and the radiative lifetime are given in Table 7.1 for the large subset of dots for various samples studied throughout this thesis.

	Integrated Optical Cross Section / X 10^{-16} eVcm^{-2}	**Radiative Lifetime / ns**
Chapter 4:		
HGTSL	2.39 ± 0.75	1.8 ± 0.6
Repeat HGTSL	2.5 ± 0.81	1.73 ± 0.54
Chapter 5:		
3 Layer	1.29 ± 0.63	3.34 ± 0.97
5 Layer	1.78 ± 0.69	2.42 ± 0.86
7 Layer	1.61 ± 0.63	2.70 ± 0.91
10 Layer	1.89 ± 0.72	2.28 ± 0.81
Chapter 6:		
5 Layer Un-doped	1.78 ± 0.69	2.42 ± 0.86
5 Layer 15-P dopants	1.85 ± 0.76	2.31 ± 0.89
5 Layer 50-P dopants	1.71 ± 0.81	2.55 ± 0.93
7 Layer Undoped	1.85 ± 0.61	2.31 ± 0.76
7 Layer 18-P dopants	1.78 ± 0.65	2.42 ± 0.83

Table 7.1: - Values for the optical cross section and radiative lifetime for the large dots.

The true absorption spectra (i.e. the absorption under a reverse bias) have been used to obtain the lifetimes for the doped structures studied in chapter 6. All the samples have very similar values for the radiative lifetime and are essentially the same within the experimental uncertainties. The errors quoted in Table 7.1 were determined from the uncertainty in fitting the Gaussians to the absorption spectra and do not take account of any changes in the dot density between samples. These results show that the spontaneous lifetime of an exciton in a single In(Ga)As quantum dot is unaffected by

altering the spacer layer growth, stacking the layers or including p-doping. This result initially seems surprising, however it needs to be remembered that lifetime calculated here is for an average lifetime per dot and although the various techniques used in this work may have altered the non-radiative processes and / or the carrier distributions these factors will have no effect on the lifetime determined here. The calculations have also been repeated for the smaller subset of dots with the results shown in Table 7.2.

	Optical Cross Section / X 10^{-15} eVcm^{-2}	**Radiative Lifetime / ns**
Chapter 4:		
HGTSL	1.15 ± 0.31	0.38 ± 0.12
Repeat HGTSL	1.92 ± 0.38	0.23 ± 0.17
Chapter 5:		
3 Layer	1.44 ± 0.24	0.30 ± 0.12
5 Layer	1.18 ± 0.14	0.37 ± 0.10
7 Layer	0.69 ± 0.09	0.63 ± 0.13
10 Layer	0.34 ± 0.11	1.21 ± 0.21
Chapter 6:		
5 Layer Un-doped	1.18 ± 0.14	0.37 ± 0.10
5 Layer 15-P dopants	1.16 ± 0.14	0.38 ± 0.10
5 Layer 50-P dopants	1.21 ± 0.16	0.36 ± 0.11
7 Layer Undoped	1.29 ± 0.19	0.35 ± 0.13
7 Layer 18-P dopants	1.38 ± 0.24	0.33 ± 0.14

Table 7.2: - Values of the optical cross section and radiative lifetime for the small dots.

The multilayered structures studied in chapter 5 show a periodically increasing lifetime with an increase in the number of layers. However this is likely to be a false result caused by the fact that the density of small dots per layer appears to decrease as the number of layers is increased (see chapter 5). As such too large dot densities have been used in the determination of the integrated optical cross section resulting in an overly high radiative lifetime being determined. The rest of the structures studied yield similar values for the radiative lifetime again suggesting that the lifetime of a single dot remains unaffected by any of the techniques studied in this work.

The smaller dots exhibit a shorter lifetime than the larger subset, in contradiction to previously published data [119,122]. However as stated previously past studies have used photoluminescence techniques to determine a lifetime for the ensemble whereas the average lifetime of a dot has been determined here. It is therefore possible that although the lifetime decreases with a decreasing dot size a change in the carrier distribution and / or non-radiative processes associated with this size change lead to an increased lifetime for the ensemble.

7.3 Radiative Lifetime as a function of temperature

The technique can be used to obtain the spontaneous lifetime per dot as a function of temperature. Previous temperature studies of the radiative lifetime have given contrasting results; with an increasing [119] and decreasing lifetime [116] for an increasing temperature both being reported, along with a largely temperature insensitive lifetime [118,120]. The differing behaviours reported are likely to have arisen from the measurements being made on the total lifetime of an ensemble of dots and hence will have been influenced by any changes in the non-radiative rates as a function of temperature as well as temperature effects on the transport of the carriers. The data in chapter 6 showed that the total non-radiative rate is largely constant between 200 and 300 K at a fixed injection level, suggesting that no change would be observed in the non-radiative lifetime over this range.

The spontaneous lifetime measured via this technique will be unaffected by these factors and hence give the true temperature dependence of the radiative lifetime of a single dot. The temperature dependence has been calculated for both the small and large dots for the HGTSL sample, studied in chapter 4 and are presented in Figure 7.2.

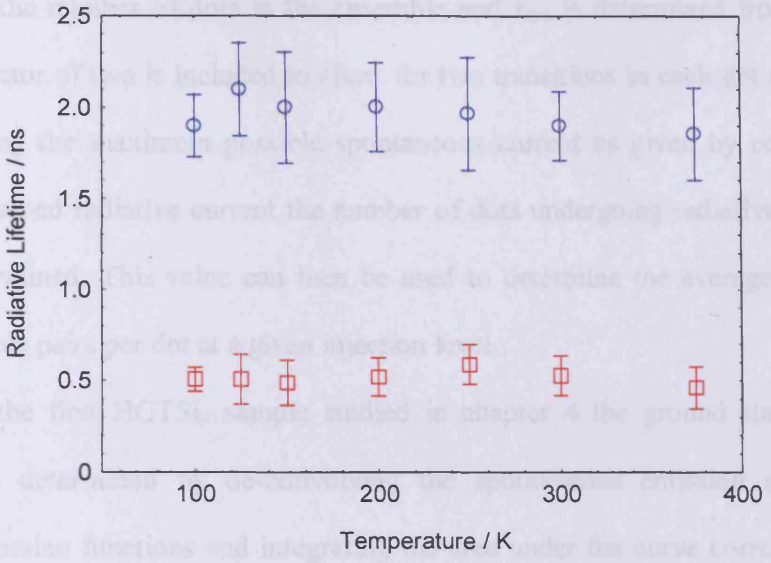

Figure 7.2: - Radiative lifetimes as a function of temperature for the HGTSL sample for the large (circles) and the small (squares) subset of dots.

These results show that for both subsets of dots the spontaneous lifetime is independent of temperature. This result appears physically reasonable as the matrix element is temperature insensitive, and as such it is difficult to see how the lifetime will change with temperature. Although the lifetime of a single dot is unaffected by the temperature the life of the carriers in the ensemble may still change as a function of temperature due to carrier transport or non-radiative effects. Such changes could potentially alter the lifetime of an ensemble, resulting in the varying lifetimes previously measured from photoluminescence techniques [116,118-120].

7.4 Radiative Current and the Radiative lifetime

If all the dots in an ensemble had fully inverted ground states then the corresponding ground state radiative current would be given by,

$$J_{Spon} = \frac{2eN}{\tau_{rad}}$$ **Equation 7.1**

where N is the number of dots in the ensemble and τ_{rad} is determined from equation 1.35. The factor of two is included to allow for two transitions in each dot due to spin. By comparing the maximum possible spontaneous current as given by equation 7.1, with the obtained radiative current the number of dots undergoing radiative transitions can be determined. This value can then be used to determine the average number of electron – hole pairs per dot at a given injection level.

For the first HGTSL sample studied in chapter 4 the ground state radiative current was determined by de-convolving the spontaneous emission spectra into separate Gaussian functions and integrating the area under the curve corresponding to the ground state. The result from this process is shown in Figure 7.3.

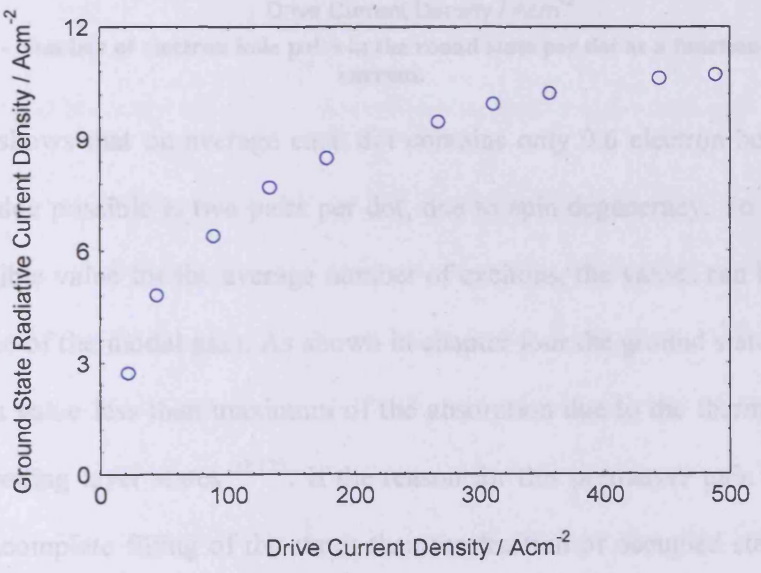

Figure 7.3: - Ground state radiative current as a function of injection current for the first HGTSL sample.

This shows a saturating ground state radiative current, reaching a maximum value of approximately 11 Acm^{-2}. From the radiative lifetime determined previously (Table 7.1) and using equation 7.1 a maximum current of 28.4 Acm^{-2} is predicted from

the ground state. Therefore only approximately 30 % of the maximum possible current is achieved from the ground state. Figure 7.3 has then been re plotted to show the average number of excitons per dot at a given injection level.

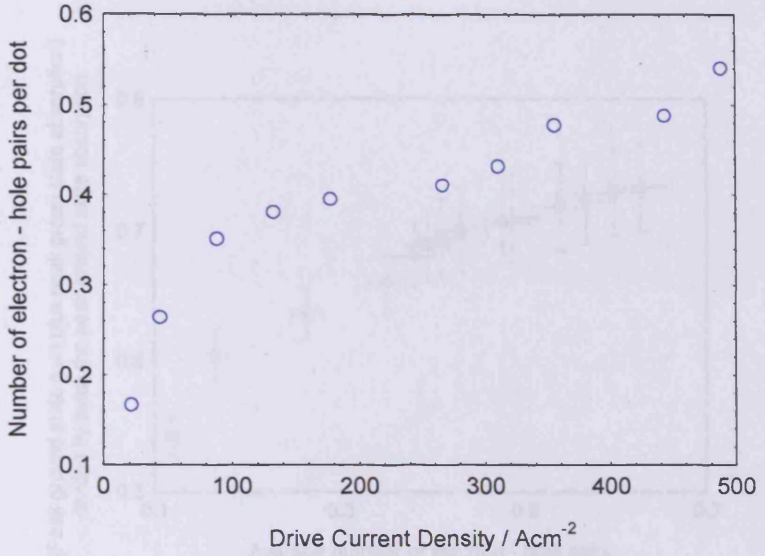

Figure 7.4: - Number of electron hole pairs in the round state per dot as a function of injected current.

This shows that on average each dot contains only 0.6 electron hole pairs; the maximum value possible is two pairs per dot, due to spin degeneracy. To determine if this is a sensible value for the average number of excitons, the values can be compared with the value of the modal gain. As shown in chapter four the ground state modal gain saturates at a value less than maximum of the absorption due to the thermal escape of carriers to wetting layer states [32,123]. If the reason for this premature gain saturation is due to the incomplete filling of the states then the fraction of occupied states (average number of excitons per dot) should correspond to the fraction of the modal gain achieved (i.e. peak modal gain divided by peak absorption). To see if this is the case the peak ground state gain has been scaled by the peak ground state modal absorption and plotted as a function of the average number of excitons per dot. The gain has been scaled by determining the peak ground state gain plus the peak ground state absorption divided by twice the peak absorption. This will give a scale that ranges from 0

(indicating that there is full absorption), which would be expected when there are no carriers in the dots to a value of unity (indicating maximum gain), which would be expected when all the states are occupied.

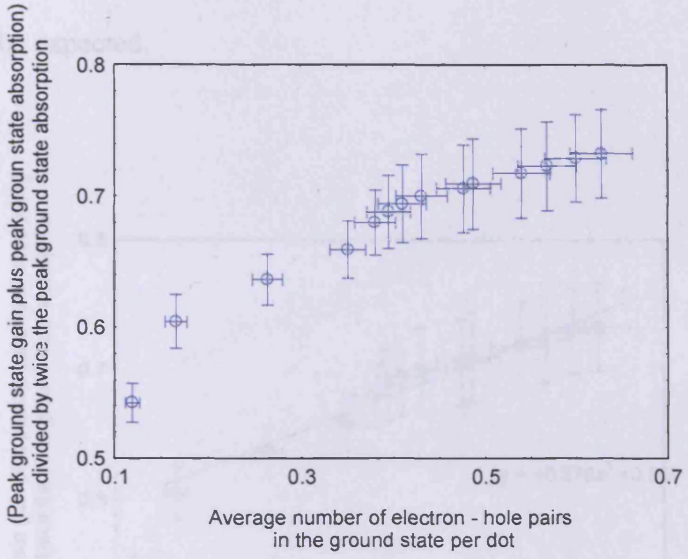

Figure 7.5: - Ratio of ground state gain to absorption as a function of the number of electron hole pairs per dot.

As the average number of carriers in the ground state is increased so the gain also increases. The y-axis reaches a maximum value of 0.74, indicating that the modal gain reaches approximately 37 % of its maximum value; the average number of carriers per dot corresponding to this is 0.67 excitons per dot. As mentioned previously the maximum number of excitons allowed in each dot is two, due to spin degeneracy. This therefore means that approximately 34 % of the ground state dot states are occupied. These two numbers have a reasonable agreement within the experimental uncertainty, indicating that the premature saturation of the gain is caused by the incomplete occupation of the dot states. The agreement is unlikely to be exact as in the determination of the number of excitons the entire inhomogenously broadened distribution is taken into consideration; however the measurement of the peak gain only involves a small percentage of these states. It is also worth noting that from the

derivations is chapter one that the gain is governed by the difference in the occupation probabilities (equation 1.28), whereas the spontaneous emission rate is proportional to a multiplication of these factors (equation 1.41). This means that there is a non-trivial relationship between the quantities plotted in Figure 7.5, so a linear relationship would not necessarily be expected.

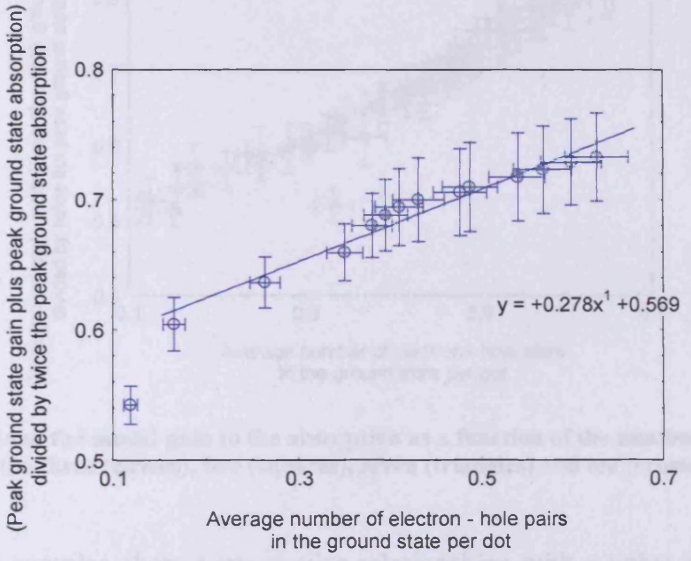

Figure 7.6: - Linear dependence of the average number of excitons per dot and the modal gain.

The first point does not follow this linear dependence; this may be due to the low signal levels for this point, resulting in an inaccurate measurement of the gain and / or the spontaneous emission, or due to the non-trivial behaviour between these quantities discussed above. The gradient of the line predicts when all available ground states are full (x = 2) then a value of 1.12 is obtained, this is slightly higher than theoretical maximum of unity. However it is a reasonable figure given the uncertainties involved in these calculations.

To look at this effect in more detail and further support for the idea of the incomplete inversion of the dot states this analysis has been repeated on the multi layered samples investigated in chapter 5.

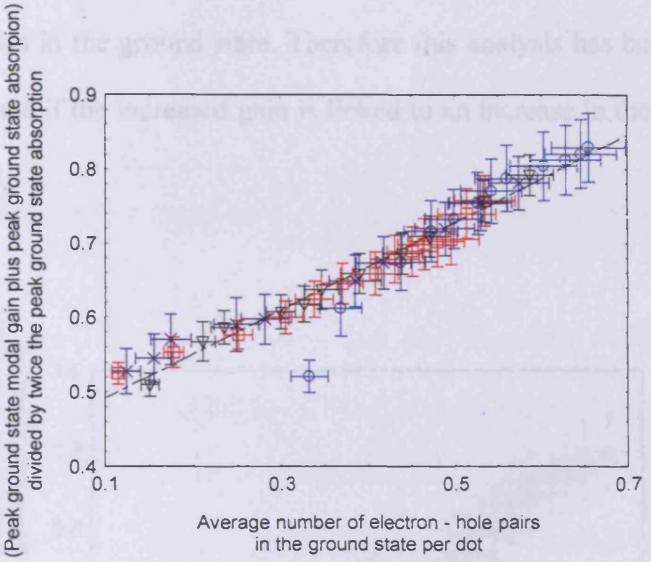

Figure 7.7: - Ratio of the modal gain to the absorption as a function of the number of electron hole pairs per dot for the three (circles), five (squares), seven (triangles) and ten (crosses) layer samples.

All four samples show very similar relationships with a value of around 40 % being obtained for the maximum fraction of the gain in each case. This is obtained with approximately 0.64 excitons in each dot (corresponding to 32 % of the dot states being occupied.) A linear fit through all the data points predicts a value 1.08 for when all the dot states are occupied. These values again show a reasonable agreement within the experimental uncertainties. The similarity between the structures is not surprising due to the values of the gain per layer determined in chapter 5. This therefore shows that stacking the quantum dot layers does not result in an increased average occupancy of the dot states and hence the gain saturates at the same fraction of the maximum. The values obtained for these samples are similar to those determined previously for the HGTSL sample studied in chapter four (Figure 7.5). This again is a reasonable result as

the five layer sample studied here is a repeat of this structure and hence similar behaviour should be observed.

An increased modal gain was observed for the p-type modulation doped structures studied in chapter 5. The explanation given for this was an increased occupation of holes in the ground state. Therefore this analysis has been performed on these samples to see if the increased gain is linked to an increase in the average number of carriers per dot.

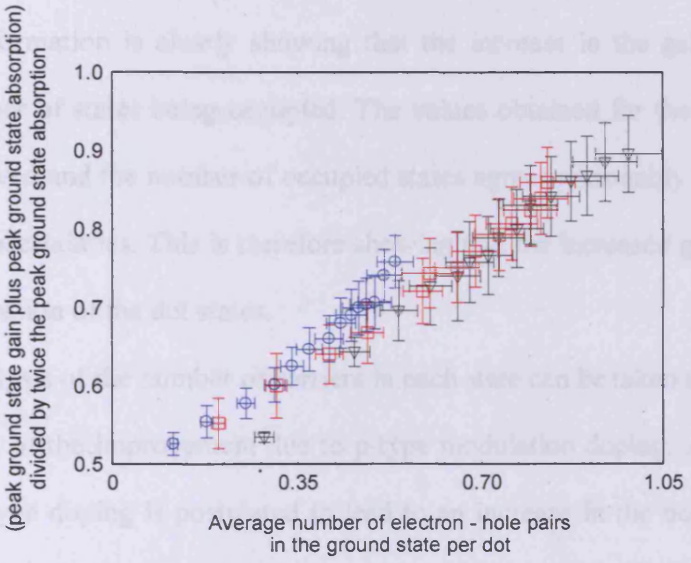

Figure 7.8: - Ratio of the ground state gain to absorption as a function of the average number of electron hole pairs per dot for the un-doped (circles), 15-p doped (squares) and 50-p doped (triangles) samples.

This clearly shows that as the doping is increased a higher fraction of the maximum possible gain can be achieved increasing from a value of approximately 0.8 for the un-doped to 0.87 for the 15-dopant case and further increasing to 0.91 for the 50-doped sample. This is linked with an increase in the average number of excitons per dot from 0.63 (corresponding to 31 % of the states being occupied) for the un-doped sample to values of 0.85 (43 %) and 1.02 (51%) for the 15 and 50-doped samples respectively. This information is summarised in Table 7.3.

	Fraction of maximum gain achieved	Percentage of state occupied
Un – doped	0.45	31
15-p dopants	0.49	43
50-p dopants	0.53	51

Table 7.3: - Comparison of the fraction of the maximum gain achieved and the fraction of states occupied.

This information is clearly showing that the increase in the gain is due to an increased number of states being occupied. The values obtained for the fraction of the total gain achieved and the number of occupied states agrees reasonably well within the experimental uncertainties. This is therefore showing that the increased gain is due to an increased occupation of the dot states.

The analysis of the number of carriers in each state can be taken a step further to show the origin of the improvement due to p-type modulation doping. As described in chapter six, p-type doping is postulated to lead to an increase in the occupation of the states at a fixed injection level (quasi-Fermi level separation)[95,105,124]. Using the information obtained here (Figure 7.9) it is possible to determine the average number of excitons per dot as a function of the transparency point.

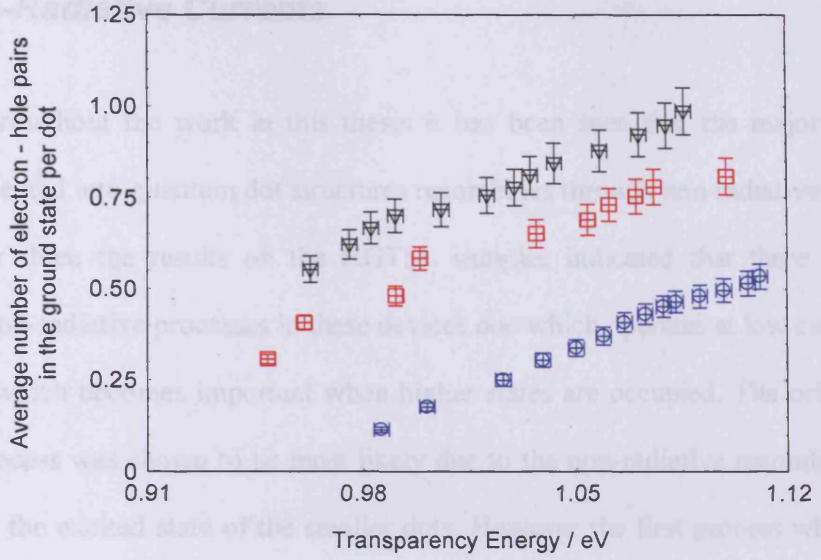

Figure 7.9: - Number of excitons per dot as a function of the transparency energy for the un-doped (circles), 15-p dopants (squares) and 50-p dopants (triangles) samples.

This clearly shows that at a fixed transparency point a higher fraction of the ground state dot states are occupied as the level of doping is increased. As explained in chapter two if the carriers can be described by Fermi-Dirac statistics then the transparency point gives the value of the quasi-Fermi level separation. From studying the temperature performance of these structures (chapter seven) it was shown that by 300 K all three structures could be described by Fermi-Dirac statistics. Therefore Figure 7.10 shows that at a given quasi-Fermi level separation a higher percentage of states are occupied when p-type dopants are present. This is the origin of the subsequent improvement in the gain of p-doped structures as was initially predicted [95,105,124] however this is the first experimental verification of the effect.

7.5 Non-Radiative Currents

Throughout the work in this thesis it has been seen that the majority of the current injected into quantum dot structures recombines through non-radiative channels. In chapter three the results on the HGTSL samples indicated that there were two separate non-radiative processes in these devices one which operates at low currents and a second which becomes important when higher states are occupied. The origin of the second process was shown to be most likely due to the non-radiative recombination of carriers in the excited state of the smaller dots. However the first process which limits the device efficiency to less than 20% (and is over the range where low threshold performance has been achieved [52]) was not fully identified. Although the process seems to be associated with the ground state of the larger dots, it could be due to defect related recombination or Auger recombination.

The radiative lifetime information can be used to try and identify the origin of this non-radiative process by determining the non-radiative current as a function of the number of excitons in each dot. This has been done for the multi layered samples evaluated in chapter 4, at low injection currents (i.e. when the ground state emission is dominant). These samples showed an increasing non-radiative current over this regime as the number of layers was increased.

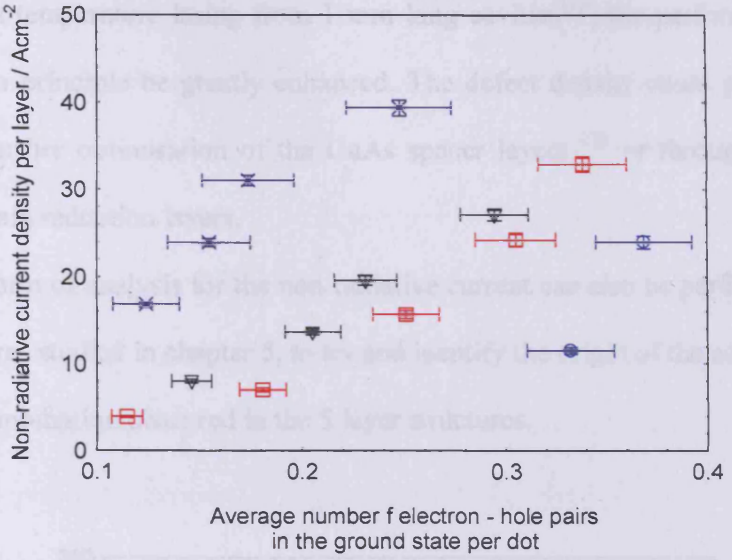

Figure 7.10: - Non radiative current density per layer as a function of the number of excitons per dot for the 3 (circles), 5 (squares), 7 (triangles) and 10 layer samples at 300 K.

This plot clearly shows that for a fixed number of excitons per dot the non-radiative recombination increases as the number of layers is increased. If the non-radiative process were due to an Auger process the same amount of non-radiative recombination per layer should be obtained for the same number of excitons. As fewer carriers are being injected into the dots to achieve the same level of non-radiative recombination as the number of layers is increased, this suggests that the source of the non-radiative channel is a caused by carriers recombining in defects external to the dots. It was shown in chapter four that as the number of layers is increased the defect density also increases (possibly due to the added strain in the structure), it is then these defects that lead to the non-radiative recombination increasing.

This analysis has shown that in the quantum dot samples studied in this work the primary source of non-radiative recombination is due to defect related processes, limiting the efficiency to less than 20% at low injection levels. Therefore despite the excellent performance obtained from these structures (threshold currents of 31 Acm^{-2}

[52,53] and room temperature lasing from 1 mm long cavities[125]) the performance of the devices can in principle be greatly enhanced. The defect density could potentially be reduced by further optimisation of the GaAs spacer layers [126] or through the use of alternative strain reduction layers.

This form of analysis for the non-radiative current can also be performed for the doped structures studied in chapter 5, to try and identify the origin of the additional non-radiative recombination observed in the 5 layer structures.

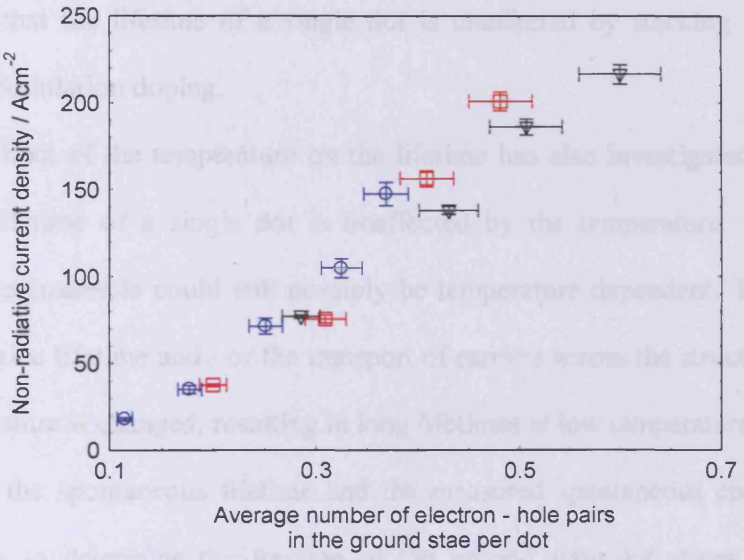

Figure 7.11: - Non-radiative current density as a function of the number of excitons per dot for the un-doped (circles), px15 doped (squares) and px50 doped (triangles) samples at 300 K.

These three samples show a similar dependence for the non-radiative current; this seems to rule out additional defect recombination in the doped samples as this would result in the behaviour observed in Figure 7.11. If the additional non-radiative recombination was due to increased Auger process or leakage of carriers then non-radiative current would be the same for the same number of excitons and the observed effects would be due to the devices being injected to different levels. Therefore either increased Auger or loss of holes seem responsible for the observed increase, however

these are intrinsic processes and would also be expected to lead to an evaluated rise in non-radiative recombination in the seven layer doped samples studied.

7.6 Conclusions

The work described in this chapter has shown that the average spontaneous lifetime per dot can be determined from the optical cross section of the dot. As such lifetimes have been determined for both the large and small dots of all the samples studied in the previous chapters. It has been found that the larger dots have a longer lifetime and that the lifetime of a single dot is unaffected by stacking the layers or introducing modulation doping.

The effect of the temperature on the lifetime has also investigated, it has been shown that lifetime of a single dot is unaffected by the temperature. However the lifetime of the ensemble could still possibly be temperature dependent. This is due to the non-radiative lifetime and / or the transport of carriers across the structure changing as the temperature is changed, resulting in long lifetimes at low temperatures.

From the spontaneous lifetime and the measured spontaneous emission it has been possible to determine the fraction of the ground state dot states occupied by carriers. It has been found that only 30 – 40 % of the states are occupied, resulting in the modal gain only being able to reach approximately 40 % of its maximum value.

The introduction of p-type modulation doping has been shown to result in a higher fraction of dot states being occupied and hence enabling a higher maximum gain to be reached. Furthermore the improvements due to p-type doping have been shown to be due to an increase in the fractional occupation of the states at a fixed quasi-Fermi level separation.

Through determining the spontaneous lifetime it has been possible to evaluate the origin of non-radiative processes in these structures. It has been shown that the major source of non-radiative recombination in these quantum dot structures is from defect related processes; as such it is theoretically possible to greatly improve on the current performance available.

8. Summary and Future Prospects

8.1 Summary:

The work in this thesis has evaluated the performance of self-assembled InAs quantum dot lasers operating at 1.3 μm, by evaluating the modal absorption and gain along with the recombination currents in a variety of structures. Threshold current measurements have also been performed as a function of cavity length.

These structures are important as they offer a potential way to develop semiconductor laser diodes grown on GaAs substrates that operate over the technologically important wavelength range 1.3 – 1.6 μm. This will provide cheaper, more efficient and less temperature sensitive lasers to operate over these wavelengths, when compared to alternative approaches.

To enable these structures to be fully characterised, the modal gain and recombination paths have been analysed. Knowledge of the modal gain spectra allows for accurate design of VCSEL cavities for surface emission at 1.3 μm, while knowledge of the radiative and non-radiative currents allows the efficiency of the structures to be determined and optimised.

In this work a large number of different structures have been studied, with a primary aim of maximising the modal gain and the radiative recombination. It has been shown that the distribution and quality of the dots formed is heavily influenced by the growth conditions (chapters 3 and 4). It has been shown to be likely that the dots form in a bi-modal distribution and that both the number of dot layers stacked and the growth parameters of the GaAs spacer layers can influence this, shifting the dots towards a more mono-modal distribution.

The non-radiative recombination in these structures has also been shown to be comprised of two separate mechanisms (chapters 3 and 4). The first of these was found to be associated with defect and dislocation formation, limiting the overall efficiency to around 20 % at room temperature. The second was shown to be most likely due to non-radiative recombination in the smaller dots, leading to a further reduction in efficiency at high injection currents. However stacking more quantum dot layers appears to reduce the number of smaller dots, and hence limit the second process. The increased number of layers also appears to increase the number of defects increasing the first non-radiative process. It has also been shown that the growth of the GaAs spacer layers can also reduce the number of defects forming leading to improved efficiencies and performance. From all the structures studied in this work it appears that the major non-radiative currents in these samples is due to defect related processes. As such it would appear that Auger related processes are not responsible for the effects observed in this work.

The spontaneous lifetime of the dots in each structure were also evaluated (in chapter 7). This was achieved by determining the optical cross section for the large and small dots from absorption measurements. It was shown that all the structures investigated in this thesis had similar lifetimes of 2.0 ± 0.5 ns and 0.6 ± 0.4 ns for the large and small dots respectively. It was also shown that the lifetime is temperature insensitive. The lifetime measurements were used to convert radiative currents into the number of excitons present at a given injection level. This information was used to show that gain saturation in quantum dot structures is due to the incomplete occupation of dot states, as suggested previously [32], with typically only a third of the quantum dot states being occupied, resulting in a gain per layer of 1.2 ± 0.2 cm^{-1} in most of the samples investigated.

The notion of modulation doping in quantum dot structures has also been investigated (chapters 5 and 6). It was shown that n-type modulation doping alters the growth of the subsequent dots, most probably via diffusion of the donors. However it was shown that p-type dopants could be successfully incorporated into InAs structures without altering the subsequent dot growth or the internal scattering loss, with a value of 2 ± 2 cm^{-1}, being measured in all the samples studied. The p-doped structures exhibited an increased gain at a fixed transparency point. However due to an increased non-radiative contribution in some of the doped structures this improvement was not always seen in the gain current curves. From the lifetime measurements it was shown that this improved gain is due to an increased occupation of states at a given transparency point, as originally predicted [95,105,124], resulting in an increased occupancy of 43% and 51% for the 15 and 50-p doped samples respectively.

The temperature dependence of the threshold current in p-doped and intrinsic quantum dot samples was also investigated (chapter 6). It was shown that the presence of p-dopants can result in temperature insensitive threshold currents or decreasing thresholds with increasing temperature. For a 2 mm long cavity for the 15-p doped sample an initial decrease of $100 Acm^{-2}$ occurs between 180 and 290 K, before the threshold increases at higher temperatures. By separately investigating the behaviour of the modal gain and the non-radiative current at a fixed injection level the lowering threshold current was shown to be due to the temperature dependence of the modal gain. By studying the shape of the spontaneous emission and the carrier distribution as a function of temperature, it was shown that the temperature dependence of the gain originates from the carriers moving from a random population distribution to a thermal distribution at higher temperatures in the doped structures compared to intrinsic devices.

8.2 Comparison to other results and optimisation

The highest reported modal gain to date for an InAs quantum dot system operating at 1.3 μm is 41 cm^{-1} (corresponding to a gain of 6 cm^{-1} per layer)[126], allowing pulsed room temperature lasing from a 360 μm long cavity with a current density of 622 Acm^{-2}. The highest modal gain achieved in this work[125] is 15 cm^{-1} (a gain per layer of 3 cm^{-1}) leading to ground state lasing from a 1 mm long cavity with a threshold current density of 210 Acm^{-2}.

Previous work on p-type modulation doping has indicated that the presence of dopants leads to an increase in the threshold current density of a laser structure[100,103]. The data presented in chapter six, shows that both doped and undoped structures exhibit a very similar threshold current density at room temperature for 2 mm long cavities.

The improved HGTSL structure studied in chapter three results in a T_0 value of 85 K (over the temperature range 20 – 70^{0}C)[125], which is similar to other best reported T_0 values for undoped quantum dot structures.[98] The inclusion of p dopants has been shown to lead to a temperature insensitive (an infinite T_0) or even a decreasing threshold with increasing temperature (negative T_0) over certain temperature regimes [77,97,100,109], this is in agreement with other reports of p-doped laser structures.

This overview shows that both the doped and undoped structures evaluated and developed in this work are comparable to the best reported results in the literature, with the lowest reported room temperature threshold current density for a p-doped laser reported from this work.

Current commercial lasers operating at 1.3 μm are based on InGaAlAs quantum wells grown on InP substrates. The best reported[127] modal gain from such structures is 18 cm^{-1}, allowing room temperature operation from a 250 μm long cavity with high

reflective coatings. These devices give a T_0 of 95 K in the range from 20 – 80 ^{0}C. An alternative system for operation at 1.3 μm is based on so called 'dilute nitrogen' quantum wells, these are GaInAsN quantum wells grown on GaAs substrates, these currently give modal gains of around 20 cm^{-1} with T_0 values of 120 K over the same temperature range[128]. Therefore these results clearly show that quantum dot structures offer a viable alternative to current systems with higher reported modal gains and much improved temperature sensitivity.

The results in this thesis can be used to determine the optimum growth conditions for an InAs quantum dot laser, i.e. what conditions maximise the gain and minimise the non-radiative current. The results in chapter three show that the optimum GaAs matrix growth conditions are a thickness of 35 nm, with the final 20 nm grown at a temperature of 620^{0}C. These conditions minimise the number of smaller dots that form, as well as resulting in a greater uniformity of the larger dots. This has been shown to lead to an enhancement in the modal gain that can be achieved at 1.3 μm, while also improving the radiative efficiency. In chapter seven it was shown that the inclusion of p-type doping increases the modal gain available, however it was also observed that the non-radiative current can also increase in the presence of dopants. It should also be noted that the incorporation of the dopants had to be carefully considered to avoid diffusion into the dots, as such the modified growth conditions of the spacer layer, may not make it feasible to include p-dopants. The data on stacking multiple layers in chapter four revealed that as the number of layers is increased, the density of large dots remains the same in each layer, while the number of the smaller dots decreases leading to an increased density of non-radiative centres. This was explained due to the increase in the overall strain in the structure (generated by the In content of the wells and the dots themselves) increasing as the number of layers increased. This increased strain

results in an increase in the number of large incoherent islands forming, which grow in size from the accumulation of material from the smaller dots. It was shown that up to ten layers could be stacked without adversely affecting the ground state modal gain, however due to the increased number of non-radiative centres the non-radiative current also increased. The improvements observed from modifying the spacer layer, should help to stack quantum dot layers. The improved structure, showed a decrease in both the number of small dots forming and the number of non-radiative centres present in a five layer structure. As such the inclusion of these layers should help to improve the performance of structures with a higher number of stacked layers, this is due to a decreased number of smaller dots, limiting the amount of material that can nucleate to form large non-radiative centres, as well as the improved structure resulting in a reduced strain accumulation, which will reduce the number of defects that form. As such from this work the optimal structure for laser performance at 1.3 μm would involve an undoped ten layer DWELL stack with 35 nm modified HGTSLs, as this should both maximise the gain and minimise the non-radiative currents.

8.3 Future Prospects:

The work in this thesis has helped develop and improve the performance of InAs quantum dot structures. However there still are several areas which can be explored further to enable the optimisation of quantum dot laser structures.

With the incorporation of the modified HGTSLs, it may be possible to stack more DWELL layers, before the amount of strained material leads to considerable defect formation for the reasons discussed above. A further problem with adding additional layers is the reduced interaction with the optical field, for the structures studied in chapter four it was found that the average optical field strength per DWELL

decreased to 83 % for the ten layer sample (compared to a hypothetical 1 layer sample). If the number of DWELLs was increased to 15, this would reduce the average field strength to 54 %, severely reducing the impact of including extra layers. As such with these structures there would seem to be only a minimal improvement possible if the number of layers was increased much beyond 10, while the possibility of defect formation would become more significant as the number of stacks was increased.

As speculated previously the inclusion of p-type dopants into the modified GaAs spacer layers may help to lead to further improvements. However the work in chapter five which showed that p-type dopants can be incorporated into quantum dot structures, without significantly increasing the non-radiative losses, resulting in improved gain current performance used 50 nm GaAs spacer layers and not the improved 35 nm spacers evaluated at the end of chapter three. It would therefore be interesting to investigate doped samples using 35 nm spacer layers to see if the improvements due to doping and smoother GaAs surfaces can be combined or if the reduced thickness results in the dopants diffusing into the dots.

To cover the telecommunications market the emission wavelength needs to be extended further towards 1.55 μm. Longer wavelength emission from InAs quantum dot structures has recently been reported by several groups [129-132]. However the techniques used to grow these structures results in low dot densities, therefore limiting the modal gain available. It would be interesting to characterise samples emitting at longer wavelengths to quantify the effect of the reduced density on the gain as well as evaluating the radiative and non-radiative currents in these structures. The techniques used in this work should also be applicable in longer wavelength dot structures. By using similar HGTSLs and annealing techniques it should be possible to improve the GaAs growth surface. As observed in this work, this should lead to an increased density

of dots and an improved inhomogeneous broadening of them, while reducing the number of defects and non-radiative centres in the structure. Likewise it should be possible to use p-type dopants in these longer wavelengths dots to address the asymmetry in the quasi-Fermi levels and hence increase the occupation of the dots, leading to an enhancement of the available modal gain.

References

[1] P. Blood, G. M. Lewis, P. M. Smowton, H. Summers, J. Thomson, and J. Lutti, IEEE Journal of Selected Topics in Quantum Electronics **9,** 1275-1282 (2003).

[2] Y. Arakawa and H. Sakaki, Applied Physics Letters **40,** 939-941 (1982).

[3] D. Bimberg, M. Grundmann, and N. N. Ledentsov, *Quantum dot heterostructures* (John Wiley, Chichester, 1999).

[4] V. M. Ustinov, *Quantum dot lasers* (Oxford University Press, Oxford, 2003).

[5] J. R. Hook and H. E. Hall, *Solid state physics*, 2nd ed. (Wiley, Chichester, 2000).

[6] C. Kittel, *Introduction to solid state physics*, 7th ed. (Wiley, New York ; Chichester, 1996).

[7] R. N. Hall, G. E. Fenner, J. D. Kingsley, T. J. Soltys, and R. O. Carlson, physical Review Letters **9,** 366-368 (1962).

[8] M. I. Nathan, W. P. Dumke, G. Burns, F. H. J. Dill, and G. Lasher, Applied Physics Letters **1,** 62-63 (1962).

[9] N. J. Holonyak and S. F. Bevacqua, Applied Physics Letters **1,** 82-83 (1962).

[10] T. M. Quist, R. H. Rediker, R. J. Keyes, W. E. Krag, B. Lax, A. L. McWhorter, and H. J. Zeigler, Applied Physics Letters **1,** 91-92 (1962).

[11] Z. I. Alferov, V. M. Andreev, E. l. Portnoi, and M. K. Trukan, Sov. Physics. Semiconductor **3,** 1107 (1970).

[12] I. Hayashi, M. B. Panish, and P. W. Foy, IEEE Journal of Quantum Electronics **5,** 211 (1969).

[13] M. B. Panish, I. Hayashi, and S. Sumski, IEEE Journal of Quantum Electronics **5,** 210 (1969).

[14] I. Hayashi, M. B. Panish, P. W. Foy, and S. Sumski, Applied Physics Letters **17,** 109-111 (1970).

[15] G. H. B. Thompson and P. A. Kirkby, IEEE Journal of Quantum Electronics **9,** 311-318 (1973).

[16] M. B. Panish, IEEE Transactions on Microwave Theory and Techniques **1,** 20-30 (1975).

[17] K. Aiki, M. Nakamura, J. Umeda, A. Yariv, A. Katzir, and H. W. Yen, Applied Physics Letters **27,** 145-146 (1975).

[18] N. Holonyak, R. M. Kolbas, R. D. Dupuis, and P. D. Dapkus, IEEE Journal of Quantum Electronics **16,** 170-186 (1980).

[19] R. D. Burnham, W. Streifer, D. R. Scifres, C. Lindstrom, and T. L. Paoli, Electronics Letters- IEE **18,** 1095-1097 (1982).

[20] N. Kirstaedter, N. N. Ledentsov, M. Grundmann, D. Bimberg, V. M. Ustinov, S. S. Ruvimov, M. V. Maximov, P. S. Kopev, Z. I. Alferov, U. Richter, P. Werner, U. Gosele, and J. Heydenreich, Electronics Letters **30,** 1416-1417 (1994).

[21] R. Mirin, A. Gossard, and J. Bowers, Electronics Letters **32,** 1732-1734 (1996).

[22] H. Shoji, Y. Nakata, K. Mukai, Y. Sugiyama, M. Sugawara, N. Yokoyama, and H. Ishikawa, Electronics Letters **32,** 2023-2024 (1996).

[23] A. Einstein, Phys Z, Translated in "The Old Quantum Theory" D. ter Harr, Oxford, 1967 **18,** 121 (1917).

[24] L. A. Coldren and S. W. Corzine, *Diode Lasers and Photonic Integrated Circuits* (Wiley, 1995).

[25] R. N. Hall, Physical Review **87,** 387 (1952).

[26] W. Shockley and W. T. J. Read, Physical Review **87,** 835-841 (1952).

[27] I. P. Marko, A. D. Andreev, A. R. Adams, R. Krebs, J. P. Reithmaier, and A. Forchel, IEEE Journal of Selected Topics in Quantum Electronics **9,** 1300-1307 (2003).

[28] M. K. Zundel, N. Y. Jin-Phillipp, F. Phillipp, K. Eberl, T. Riedl, E. Fehrenbacher, and A. Hangleiter, Applied Physics Letters **73,** 1784-1786 (1998).

[29] K. Eberl, A. Kurtenbach, M. Zundel, J. Y. JinPhillipp, F. Phillipp, A. Moritz, R. Wirth, and A. Hangleiter, Journal of Crystal Growth **175,** 702-706 (1997).

[30] B. Damilano, N. Grandjean, S. Dalmasso, and J. Massies, Applied Physics Letters **75,** 3751-3753 (1999).

[31] A. Morel, M. Gallart, T. Taliercio, P. Lefebvre, B. Gil, J. Allegre, H. Mathieu, B. Damilano, N. Grandjean, and J. Massies, Physica Status Solidi a-Applications and Materials Science **180,** 375-380 (2000).

[32] D. R. Matthews, H. D. Summers, P. M. Smowton, and M. Hopkinson, Applied Physics Letters **81,** 4904-4906 (2002).

[33] P. Borri, W. Langbein, S. Schneider, U. Woggon, R. L. Sellin, D. Ouyang, and D. Bimberg, Physical Review Letters **87,** 157401 (2001).

[34] W. Ouerghui, A. Melliti, M. A. Maaref, and J. Bloch, Physica E **28,** 519-524 (2005).

[35] S. W. Osborne, P. Blood, P. M. Smowton, Y. C. Xin, A. Stintz, D. Huffaker, and L. F. Lester, Journal of Physics Condensed Matter **16,** S3749-S3756 (2004).

[36] P. Blood, IEEE Journal of Quantum Electronics **36,** 354-362 (2000).

[37] N. Kirstaedter, O. G. Schmidt, N. N. Ledentsov, D. Bimberg, V. M. Ustinov, A. Y. Egorov, A. E. Zhukov, M. V. Maximov, P. S. Kopev, and Z. I. Alferov, Applied Physics Letters **69,** 1226-1228 (1996).

[38] L. V. Asryan and R. A. Suris, Semiconductor Science and Technology **11,** 554-567 (1996).

[39] D. Bimberg, N. Kirstaedter, N. N. Ledentsov, Z. I. Alferov, P. S. Kopev, and V. M. Ustinov, IEEE Journal of Selected Topics in Quantum Electronics **3,** 196-205 (1997).

[40] P. Blood, (2006), p. Postgraduate Lecture Notes.

[41] D. L. Huffaker, G. Park, Z. Zou, O. B. Shchekin, and D. G. Deppe, IEEE Journal of Selected Topics in Quantum Electronics **6,** 452-461 (2000).

[42] G. Park, O. B. Shchekin, D. L. Huffaker, and D. G. Deppe, IEEE Photonics Technology Letters **12,** 230-232 (2000).

[43] D. L. Huffaker, G. Park, Z. Zhou, O. B. Shchekin, and D. G. Deppe, Applied Physics Letters **73,** 2564-2566 (1998).

[44] P. G. Eliseev, H. Li, A. Stintz, G. T. Liu, T. C. Newell, K. J. Malloy, and L. F. Lester, Applied Physics Letters **77,** 262-264 (2000).

[45] N. Chand, E. E. Becker, J. P. Van der Ziel, S. N. G. Chu, and N. K. Dutta, Applied Physics Letters **58,** 1704-1706 (1991).

[46] G. W. Turner, H. K. Choi, and M. J. Manfra, Applied Physics Letters **72,** 876-878 (1998).

[47] P. Bhattacharya, S. Ghosh, S. Pradhan, J. Singh, Z. K. Wu, J. Urayama, K. Kim, and T. B. Norris, IEEE Journal of Quantum Electronics **39,** 952-962 (2003).

[48] V. M. Ustinov, A. Y. Egorov, A. R. Kovsh, A. E. Zhukov, M. V. Maximov, A. F. Tsatsulnikov, N. Y. Gordeev, S. V. Zaitsev, Y. M. Shernyakov, N. A. Bert, P. S. Kopev, Z. I. Alferov, N. N. Ledentsov, J. Bohrer, D. Bimberg, A. O. Kosogov, P. Werner, and U. Gosele, Journal of Crystal Growth **175,** 689-695 (1997).

[49] A. E. Zhukov, A. R. Kovsh, N. A. Maleev, S. S. Mikhrin, V. M. Ustinov, A. F. Tsatsul'nikov, M. V. Maximov, B. V. Volovik, D. A. Bedarev, Y. M. Shernyakov, P. S. Kop'ev, Z. I. Alferov, N. N. Ledentsov, and D. Bimberg, Applied Physics Letters **75,** 1926-1928 (1999).

[50] L. F. Lester, A. Stintz, H. Li, T. C. Newell, E. A. Pease, B. A. Fuchs, and K. J. Malloy, IEEE Photonics Technology Letters **11,** 931-933 (1999).

[51] N. Ledentsov; *Vol. 6653166* (U.S, 2003).

[52] H. Y. Liu, I. R. Sellers, T. J. Badcock, D. J. Mowbray, M. S. Skolnick, K. M. Groom, M. Gutierrez, M. Hopkinson, J. S. Ng, and J. P. R. David, Applied Physics Letters **85,** 704-706 (2004).

[53] H. Y. Liu, I. R. Sellers, M. Gutierrez, K. M. Groom, W. M. Soong, M. Hopkinson, J. P. R. David, R. Beanland, T. J. Badcock, and D. J. Mowbray, Journal of Applied Physics **96,** 1988-1992 (2004).

[54] J. D. Thomson, H. D. Summers, P. J. Hulyer, P. M. Smowton, and P. Blood, Applied Physics Letters **75,** 2527-2529 (1999).

[55] G. M. Lewis, P. M. Smowton, J. D. Thomson, H. D. Summers, and P. Blood, Applied Physics Letters **80,** 1-3 (2002).

[56] Y. C. Xin, H. Su, L. F. Lester, L. Zhang, A. L. Gray, S. Luong, K. Sun, Z. Zou, T. Whittington, and J. Zilko, in *Determination of optical gain and absorption of quantum dots with an improved segmented contact method [5722-09]*, San Jose, CA, 2005 (SPIE), p. 49-59.

[57] Y. C. Xin, Y. Li, A. Martinez, T. J. Rotter, H. Su, L. Zhang, A. L. Gray, S. Luong, K. Sun, Z. Zou, J. Zilko, P. M. Varangis, and L. F. Lester, IEEE Journal of Quantum Electronics **42,** 725-732 (2006).

[58] J. Lutti, Thesis, Cardiff, 2005.

[59] H. Y. Liu, M. Hopkinson, C. N. Harrison, M. J. Steer, R. Frith, I. R. Sellers, D. J. Mowbray, and M. S. Skolnick, Journal of Applied Physics **93,** 2931-2936 (2003).

[60] H. Drexler, D. Leonard, W. Hansen, and J. P. Kotthaus, Physical Review Letters **73,** 2252 (1994).

[61] H. Jiang and J. Singh, Physical Review **56,** 4696-4701 (1997).

[62] H. Pettersson, R. J. Warburton, J. P. Kotthaus, N. Carlsson, W. Seifert, M. E. Pistol, and L. Samuelson, Physical Review **60,** R11289-R11292 (1999).

[63] W. Zhou, O. Qasaimeh, J. Phillips, S. Krishna, and P. Bhattacharya, Applied Physics Letters **74,** 783-785 (1999).

[64] H. Kissel, U. Muller, C. Walther, W. T. Masselink, Y. I. Mazur, G. G. Tarasov, and M. P. Lisitsa, Physical Review **62,** 7213-7218 (2000).

[65] O. Suekane, S. Hasegawa, M. Takata, T. Okui, and H. Nakashima, Materials Science and Engineering B **88,** 158 - 163 (2002).

[66] S. J. Lee, S. K. Noh, J. W. Choe, and E. K. Kim, Journal of Crystal Growth **267,** 405-411 (2004).

[67] M. V. Maximov, A. F. Tsatsul`nikov, B. V. Volovik, D. A. Bedarev, Y. M. Shernyakov, I. N. Kaiander, E. Y. Kondrat`eva, A. E. Zhukov, A. R. Kovsh, and N. A. Maleev, Microelectronic Engineering **51-52,** 61-72 (2000).

[68] G. Park, O. B. Shchekin, D. L. Huffaker, and D. G. Deppe, Applied Physics Letters **73,** 3351-3353 (1998).

[69] D. G. Deppe, D. L. Huffaker, S. Csutak, Z. Zou, G. Park, and O. B. Shchekin, Ieee Journal of Quantum Electronics **35,** 1238-1246 (1999).

[70] I. P. Marko, A. R. Adams, S. J. Sweeney, D. J. Mowbray, M. S. Skolnick, H. Y. Liu, and K. M. Groom, IEEE Journal of Selected Topics in Quantum Electronics **11,** 1041-1047 (2005).

[71] A. J. Bennett, P. N. Stavrinou, C. Roberts, R. Murray, G. Parry, and J. S. Roberts, Journal of Applied Physics **92,** 6215-6218 (2002).

[72] R. Fehse, S. Jin, S. J. Sweeney, A. R. Adams, E. P. O Reilly, H. Riechert, S. Illek, and A. Y. Egorov, Electronics Letters- IEE **37,** 1518-1519 (2001).

[73] T. Higashi, S. J. Sweeney, A. F. Phillips, A. R. Adams, E. P. O'Reilly, T. Uchida, and T. Fujii, IEEE Photonics Technology Letters **11,** 409-411 (1999).

[74] H. J. Pask, H. D. Summers, and P. Blood, Applied Physics Letters **87,** 083109 (2005).

[75] S. V. Zaitsev, N. Y. Gordeev, V. I. Kopchatov, V. M. Ustinov, A. E. Zhukov, A. Y. Egorov, N. N. Ledentsov, M. V. Maximov, P. S. Kop'ev, and A. O. Kosogov, Japanese Journal of Applied Physics Part 1 Regular Papers Short Notes and Review Papers **36,** 4219-4220 (1997).

[76] L. Y. Karachinsky, S. Pellegrini, G. S. Buller, A. S. Shkolnik, N. Y. Gordeev, V. P. Evtikhiev, and V. B. Novikov, Applied Physics Letters **84,** 7-9 (2004).

[77] S. Fathpour, Z. Mi, P. Bhattacharya, A. R. Kovsh, S. S. Mikhrin, I. L. Krestnikov, A. V. Kozhukhov, and N. N. Ledentsov, Applied Physics Letters **85,** 5164-5166 (2004).

[78] O. G. Schmidt, N. Kirstaedter, N. N. Ledentsov, M. H. Mao, D. Bimberg, V. M. Ustinov, A. Y. Egorov, A. E. Zhukov, M. V. Maximov, and P. S. Kop'ev, Electronics Letters- IEE **32,** 1302-1303 (1996).

[79] D. Bimberg, N. N. Ledentsov, M. Grundmann, N. Kirstaedter, O. G. Schmidt, M. H. Mao, V. M. Ustinov, A. Y. Egorov, A. E. Zhukov, and P. S. Kopev, Physica Status Solidi B Basic Research **194,** 159-174 (1996).

[80] C. H. Roh, Y. J. Park, K. M. Kim, Y. M. Park, E. K. Kim, and K. B. Shim, Journal of Crystal Growth **226,** 1-7 (2001).

[81] L. Hwack Joo, H. Ryu, and S. Nahm, Journal of Crystal Growth **182,** 292-298 (1997).

[82] H. J. Lee, H. Ryu, J. Y. Leam, S. K. Noh, H. G. Lee, and S. Nahm, Journal of Crystal Growth **172,** 18-24 (1997).

[83] X. Q. Meng, B. Xu, P. Jin, X. L. Ye, Z. Y. Zhang, C. M. Li, and Z. G. Wang, Journal of Crystal Growth **243,** 432-438 (2002).

[84] P. M. Smowton, G. M. Lewis, A. Sobiesierski, P. Blood, J. Lutti, and S. Osbourne, Applied Physics Letters **83,** 419-421 (2003).

[85] N. Tessler and G. Eisenstein, IEEE Journal of Quantum Electronics **29,** 1586 (1993).

[86] A. Hangleiter, A. Grabmaier, and G. Fuchs, Applied Physics Letters **62,** 2316 (1993).

[87] X. Q. Li and Y. Arakawa, Physical Review **56,** 10 423-10 427 (1997).

[88] R. Heitz, M. Veit, A. Kalburge, Q. Xie, M. Grundmann, P. Chen, N. N. Ledentsov, A. Hoffmann, A. Madhukar, D. Bimberg, V. M. Ustinov, P. S. Kop'ev, and Z. I. Alferov, Physica E **2,** 578 (1998).

[89] Y. Arakawa and H. Sakaki, Applied Physics Letters **40,** 939-941 (1982).

[90] M. Asada, Y. Miyamoto, and Y. Suematsu, IEEE Journal of Quantum Electronics **QE-22,** 1915-1921 (1986).

[91] K. J. Vahala, IEEE Journal of Quantum Electronics **24,** 523-530 (1988).

[92] http://ece-www.colorado.edu/~bart/ecen5355/f05/simwindows.htm, (1994).

[93] http://ece-www.colorado.edu/~bart/ecen6355/simwindows/, (1999).

[94] E. Yablonovitch and K. O. Kane, Journal of Lightwave Technology **4,** 504 (1986).

[95] K. J. Vahala and C. E. Zah, Applied Physics Letters **52,** 1942 (1988).

[96] D. G. Deppe, H. Huang, and O. B. Shchekin, IEEE Journal of Quantum Electronics **38,** 1587-1593 (2002).

[97] K. Otsubo, N. Hatori, M. Ishida, S. Okumura, T. Akiyama, Y. Nakata, H. Ebe, M. Sugawara, and Y. Arakawa, Japanese Journal of Applied Physics Part 2 Letters **43,** L1124-L1126 (2004).

[98] S. S. Mikhrin, A. R. Kovsh, I. L. Krestnikov, A. V. Kozhukhov, D. A. Livshits, N. N. Ledentsov, Y. M. Shernyakov, I. I. Novikov, M. V. Maximov, and V. M. Ustinov, Semiconductor Science and Technology **20,** 340-342 (2005).

[99] J. Kim and S. L. Chuang, IEEE Journal of Quantum Electronics **42,** 942-952 (2006).

[100] O. B. Shchekin and D. G. Deppe, Applied Physics Letters **80,** 3277-3279 (2002).

[101] Z. Mi, S. Fathpour, and P. Bhattacharya, Electronics Letters- IEE **41,** 1282-1283 (2005).

[102] J. Siegert, S. Marcinkevicius, and Q. X. Zhao, Physical Review **72,** 085316 (2005).

[103] I. P. Marko, N. F. Masse, S. J. Sweeney, A. D. Andreev, A. R. Adams, N. Hatori, and M. Sugawara, Applied Physics Letters **87,** 211114 (2005).

[104] S. Mokkapati, M. Buda, H. H. Tan, and C. Jagadish, Applied Physics Letters **88,** 161121 (2006).

[105] O. B. Shchekin and D. G. Deppe, Applied Physics Letters **80,** 2758-2760 (2002).

[106] X. Huang, A. Stintz, H. Li, A. Rice, G. T. Liu, L. F. Lester, J. Cheng, and K. J. Malloy, IEEE Journal of Quantum Electronics **37,** 414-417 (2001).

[107] P. W. Fry, I. E. Itskevich, D. J. Mowbray, M. S. Skolnick, J. J. Finley, J. A. Barker, E. P. O'Reilly, L. R. Wilson, I. A. Larkin, and P. A. Maksym, Physical Review Letters **84,** 733-736 (2000).

[108] H. Shimizu, S. Saravanan, J. Yoshida, S. Ibe, and N. Yokouchi, Applied Physics Letters **88,** 241117 (2006).

[109] O. B. Shchekin and D. G. Deppe, IEEE Photonics Technology Letters **14,** 1231-1233 (2002).

[110] S. Ghosh, P. Bhattacharya, E. Stoner, J. Singh, H. Jiang, S. Nuttinck, and J. Laskar, Applied Physics Letters **79,** 722-724 (2001).

[111] S. Krishna, P. Bhattacharya, J. Singh, T. Norris, J. Urayama, P. J. McCann, and K. Namjou, IEEE Journal of Quantum Electronics **37,** 1066-1074 (2001).

[112] D. G. Deppe, S. Freisem, H. Huang, and S. Lipson, Journal of Physics **38,** 2119-2125 (2005).

[113] D. McCumber, Phys Rev, 136 (1964).

[114] H. J. Pask, Thesis, Cardiff University, 2006.

[115] H. Y. Liu, I. R. Sellers, M. Hopkinson, C. N. Harrison, D. J. Mowbray, and M. S. Skolnick, Applied Physics Letters **83,** 3716-3718 (2003).

[116] M. Colocci, A. Vinattieri, L. Lippi, F. Bogani, M. Rosa-Clot, S. Taddei, A. Bosacchi, S. Franchi, and P. Frigeri, Applied Physics Letters **74,** 564-566 (1999).

[117] K. Kamath, N. Chervela, K. K. Linder, T. Sosnowski, H. T. Jiang, T. Norris, J. Singh, and P. Bhattacharya, Applied Physics Letters **71,** 927-929 (1997).

[118] T. Kono, Y. Nagamune, M. Nishioka, and Y. Arakawa, Superlattices and Microstructures **17,** 77 (1995).

[119] L. Zhang, T. F. Boggess, D. G. Deppe, D. L. Huffaker, O. B. Shchekin, and C. Cao, Applied Physics Letters **76,** 1222-1224 (2000).

[120] A. Melliti, M. A. Maaref, F. Hassen, M. Hjiri, H. Maaref, J. Tignon, and B. Sermage, Solid State Communications **128,** 213-217 (2003).

[121] C. Unitt, A. J. Bennett, P. Atkinson, K. Cooper, P. See, D. Gevaux, M. B. Ward, R. M. Stevenson, D. A. Ritchie, and A. J. Shields, Journal of Optics B-Quantum and Semiclassical Optics **7,** S129-S134 (2005).

[122] S. Raymond, S. Fafard, P. J. Poole, A. Wojs, P. Hawrylak, S. Charbonneau, D. Leonard, R. Leon, P. M. Petroff, and J. L. Merz, Physical Review B **54,** 11548-11554 (1996).

[123] C. L. Walker, I. C. Sandall, P. M. Smowton, I. R. Sellers, D. J. Mowbray, H. Y. Liu, and M. Hopkinson, IEEE Photonics Technology Letters **17,** 2011-2013 (2005).

[124] O. B. Shchekin, D. G. Deppe, and D. Lu, Applied Physics Letters **78,** 3115-3117 (2001).

[125] C. L. Walker, I. C. Sandall, P. Smowton, D. J. Mowbray, H. Y. Liu, S. l. Liew, and M. Hopkinson, IEEE Photonics Technology Letters **18,** 1557-1559 (2006).

[126] A. Salhi, L. Martiradonna, G. Visimberga, V. Tasco, L. Fortunato, M. T. Todaro, R. Cingolani, A. Passaseo, and M. De Vittorio, IEEE Photonics Technology Letters **18,** 1735-1737 (2006).

[127] R. Paoletti, M. Agresti, D. Bertone, L. Bianco, C. Bruschi, A. Buccieri, R. Campi, C. Dorigoni, P. Gotta, M. Liotti, G. Magnetti, P. Montangero, G.

Morello, C. Rigo, E. Riva, G. Rossi, D. Soderstrom, A. Stano, P. Valenti, M. Vallone, and M. Meliga, Journal of Lightwave Technology **24,** 143-149 (2006).

[128] Y. Wei, J. S. Gustavsson, M. Sadeghi, S. Wang, and A. Larsson, Ieee Journal of Quantum Electronics **42,** 1274-1280 (2006).

[129] I. I. Novikov, N. Y. Gordeev, M. V. Maximov, Y. M. Shernyakov, A. E. Zhukov, A. P. Vasil'ev, E. S. Semenova, V. M. Ustinov, N. N. Ledentsov, D. Bimberg, N. D. Zakharov, and P. Werner, Semiconductor Science and Technology **20,** 33-37 (2005).

[130] A. G. Gladyshev, N. V. Kryzhanovskaya, A. M. Nadtochy, E. S. Semenova, A. E. Zhukov, A. P. Vasil'ev, V. S. Mikhrin, Y. G. Musikhin, M. V. Maximov, N. N. Ledentsov, and V. M. Ustinov, Physica Status Solidi a-Applications and Materials Science **203,** 1359-1364 (2006).

[131] K. Akahane, N. Yamamoto, S. Gozu, A. Ueta, and N. Ohtani, Physica E-Low-Dimensional Systems & Nanostructures **32,** 81-84 (2006).

[132] H. Y. Liu, M. J. Steer, T. J. Badcock, D. J. Mowbray, M. S. Skolnick, F. Suarez, J. S. Ng, M. Hopkinson, and J. P. R. David, Journal of Applied Physics **99,** - (2006).